Studies of High Transverse Momentum Phenomena in Heavy Ion Collisions Using the PHOBOS Detector

by

Edward Wenger

B.A., Dartmouth College (2002)

Submitted to the Department of Physics
in partial fulfillment of the requirements for the degree of

Doctor of Philosophy

at the

MASSACHUSETTS INSTITUTE OF TECHNOLOGY

September 2008

Author . . . .
Department of Physics
August 19th, 2008

Certified by . . . .
Gunther Roland
Associate Professor of Physics
Thesis Supervisor

Accepted by . . . .
Thomas J. Greytak
Associate Department Head for Education

Studies of High Transverse Momentum Phenomena in Heavy Ion Collisions Using the PHOBOS Detector

by

Edward Wenger

Submitted to the Department of Physics
on August 19th, 2008, in partial fulfillment of the
requirements for the degree of
Doctor of Philosophy

Abstract

The use of high-p_T particles as calibrated probes has proven to be an effective tool for understanding the properties of the system produced in relativistic heavy ion collisions. In this thesis, two such measurements are presented using the PHOBOS detector at the Relativistic Heavy Ion Collider (RHIC):

1. The transverse momentum spectra of charged particles produced near mid-rapidity in Cu+Cu collisions with center-of-mass energies of 62.4 and 200 GeV per nucleon pair

2. Two-particle correlations with a high transverse momentum trigger particle ($p_T > 2.5$ GeV/c) in Au+Au collisions at $\sqrt{s_{NN}} = 200$ GeV over the broad longitudinal acceptance of the PHOBOS detector ($-4 < \Delta\eta < 2$)

In central Au+Au collisions at 200 GeV, the single-particle yields are suppressed at high-p_T by a factor of about five compared to p+p collisions scaled by the number of binary collisions. This is typically understood to be a consequence of energy loss by high-p_T partons in the dense QCD medium, as such a suppression is absent in d+Au collisions.

In Cu+Cu collisions, the nuclear modification factor, R_{AA}, has been measured relative to p+p data as a function of collision centrality. For the same number of participating nucleons (N_{part}), R_{AA} is essentially the same for the Cu+Cu and Au+Au systems over the measured range of p_T, in spite of the significantly different geometries. At high-p_T, the similarity between the two systems can be described by simple, geometric models of parton energy loss.

Two-particle angular correlations are a more powerful tool for examining how high-p_T jets lose energy and how the medium is modified by the deposited energy. In central Au+Au collisions, particle production correlated with a high-p_T trigger is strongly modified compared to p+p. Not only is the away-side yield much broader in $\Delta\phi$, the near-side peak of jet fragments now sits atop an unmistakable 'ridge' of correlated partners extending continuously and undiminished all the way to $\Delta\eta = 4$.

Thesis Supervisor: Gunther Roland
Title: Associate Professor of Physics

This work is dedicated to the memory of my grandfathers, Dennis and Donald.

Contents

1 Introduction

Quantum Chromodynamics (QCD) is a theory that describes the interaction of quarks, the fundamental building blocks of hadronic matter (e.g. protons and neutrons), with gluons, the mediators of the strong force [1]. An expected property of strongly interacting matter is that at sufficiently high temperatures, there exists a phase known as the Quark Gluon Plasma (QGP), in which quarks and gluons are no longer confined within hadrons, but rather are free to move over larger distances. Such extreme conditions may be accessed experimentally by relativistic collisions of heavy ions. By measuring the momentum spectra and the correlations between particles in heavy ion collisions, we hope to better understand the properties of the short-lived 'fireball' that is created.

1.1 Quarks

With the advent of high-energy particle accelerators and new detector technologies in the 1950's [3], many new resonances were discovered (e.g. Δ, Λ, Σ, K^0). The realization that these could not all be elementary particles motivated various classification schemes. Murray Gell-Mann [4] and Yuval Ne'eman [5] independently suggested that the various hadrons could be grouped according to the 'Eightfold Way', a name Gell-Mann borrowed from Buddhism, to describe the arrangement of mesons and baryons into octets with similar properties (see Fig. 1.1).

It was proposed that the symmetries manifested in these arrangements of hadrons could be understood by the introduction of three 'flavors' – up, down, and strange – of fractionally-charged, spin-1/2 particles named 'quarks' by Gell-Mann [6]. (Zweig originally referred to them as 'aces' [7].) In the quark model, mesons are bound states of a quark with an anti-quark (e.g. $\pi^+ = u\bar{d}$), while baryons are bound states of three quarks (e.g. $\Lambda^0 = uds$). The prediction of a baryon with spin=3/2 and strangeness=-3, the Ω^- in Fig. 1.1(c), and its subsequent discovery [8] at Brookhaven's Alternating Gradient Synchrotron (AGS) earned the quark model widespread acceptance.

By the late 1960's, experiments using the Deep-Inelastic Scattering (DIS) of electrons off of protons began to probe the inner structure of the nucleon [12], much as Rutherford had used the scattering of α-particles from gold foil to discover the atomic nucleus. At large momentum transfers, the DIS results exhibited a feature known as 'Bjorken scal-

[1] At typical energy scales, the strong force is the most powerful of the four fundamental forces, the others in order of diminishing strength being the electromagnetic, weak and gravitational forces (see Appendix A). The strong force is powerful enough to bind protons together in the nucleus, overcoming their intense electromagnetic repulsion, via residual effects of pion exchange [1] that are analogous to the induced-dipole Van der Waals' forces that attract electrically neutral molecules [2].

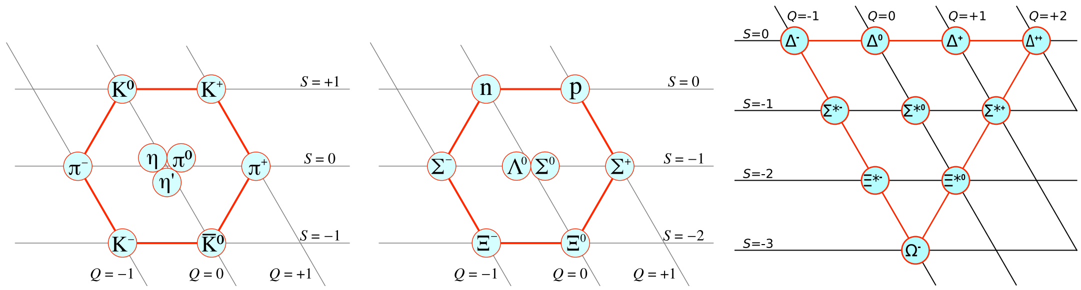

(a) Meson Nonet (b) Baryon Octet (c) Baryon Decuplet

Figure 1.1: The arrangement of hadrons by strangeness (S) and charge (Q) according to the Eightfold Way for (a) the spin-0 mesons [9] (b) the spin-1/2 baryons [10] and (c) the spin-3/2 baryons [11].

ing' [13], which implied that the electrons were scattering from point-like, spin-1/2 fermions. Later experiments confirmed that these 'partons' (as they were generically named) carried the fractional charges of the quarks (i.e. +2/3, -1/3). Tables of fundamental particle properties can be found in Appendix A.

1.2 Color

Quarks must satisfy the Pauli Exclusion principle, which forbids identical fermions (particles with half-integer spin) from occupying the same quantum state. An apparent problem in the quark model appears for the Δ^{++}. First, the three valence quarks all have the same flavor (uuu). Next, the experimentally measured spin of 3/2 requires that each spin-1/2 quark be in the same spin state $(\uparrow\uparrow\uparrow)$. Finally, the positive parity of the Δ^{++} means that the spatial wavefunction is also symmetric.

A hidden, three-valued property of quarks is required [14] for three otherwise identical quarks to coëxist within a baryon. This property is named color by analogy to white light, whereby red, green, and blue quarks combine to form a 'colorless' baryon. Each color has a corresponding anti-color, so a meson might consist of a $r\bar{r}$ pair.

The convenient introduction of color is supported experimentally by the measurement of cross-sections in high-energy e^+e^- collisions. For energies much larger than the $q\bar{q}$ mass threshold and away from resonances, the cross-section for $e^+e^- \to q\bar{q}$ is proportional to that for $e^+e^- \to \mu^+\mu^-$. Accounting for the number of different quark flavors and the electric charge on each, there is still a factor of three between the predicted and measured values of the ratio

$$\frac{\sigma(e^+e^- \to q\bar{q} \to hadrons)}{\sigma(e^+e^- \to \mu^+\mu^-)} \tag{1.1}$$

until the introduction of color [15]. This demonstrates that color is an intrinsic property of quarks, namely the production of an $r\bar{r}$ pair is distinct from a $g\bar{g}$ pair.

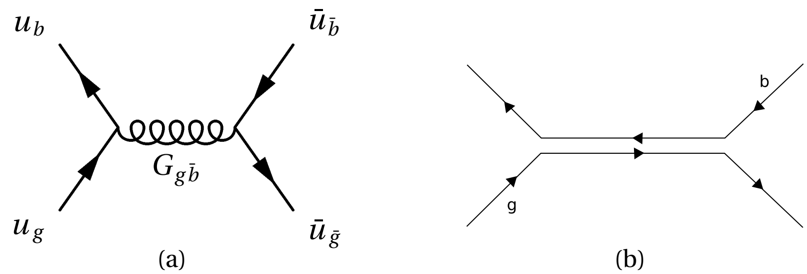

Figure 1.2: (a) The interaction of two quarks via the exchange of a gluon. Time flows upwards in the diagram. Note the exchange of color [16]. (b) Lines of color traced through the same interaction.

1.3 Gluons

Quantum Chromodynamics (QCD) is a relativistic field theory that describes the strong interactions of quarks and gluons. Field theories in particle physics are based on fundamental symmetries of nature. For QCD, this symmetry is in color. An arbitrary rotation of the three colors, for example swapping red and green, does not affect any observable physical quantity. The requirement of local gauge invariance, that is allowing the global symmetry to act independently at all points in space, was used first in Quantum Electrodynamics (QED), where it introduced into the theory a massless vector field that was identified as the photon. The fact that QCD has three colors rather than just a single charge introduces more complexity into the theory. When color charge is required to be locally invariant under gauge transformations, eight massless vector bosons called 'gluons' appear. Unlike the neutral photon, the gluons themselves carry color, the 'charge' of QCD. Each of the eight gluons carries both a color charge and an anticolor charge [2], which can be represented as

$$r\bar{b}, r\bar{g}, b\bar{g}, b\bar{r}, g\bar{b}, g\bar{r}, \frac{r\bar{r}-b\bar{b}}{\sqrt{2}}, \frac{r\bar{r}+b\bar{b}-2g\bar{g}}{\sqrt{6}}. \tag{1.2}$$

As an example, the exchange of a $g\bar{b}$ gluon between a quark and antiquark is shown in Fig. 1.2.

The best evidence for the existence of gluons comes from the study of three-jet events, first seen in e^+e^- collisions at PETRA in 1979, where one particle from the produced $q\bar{q}$ pair radiates a high-energy gluon [17]. Quantitative studies of DIS results, which only probe the charged constituents of the proton, had previously inferred the existence of gluons indirectly, since the total fraction of the proton momentum carried by the quarks is only about 50%.

[2] The eight gluon states arise from the three colors in exactly the same fashion as the meson octet arises from approximate SU(3) flavor symmetry. However, the colorless singlet gluon state, $\left(r\bar{r}+b\bar{b}+g\bar{g}\right)/\sqrt{3}$, does not exist. With no net color, this gluon would be able to mediate the strong force over macroscopic distances between other colorless objects (e.g. electrons, protons), which clearly does not happen.

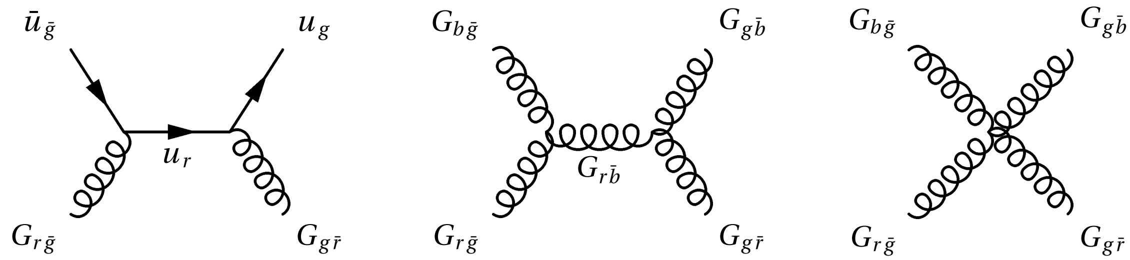

(a) Quark Exchange (b) Gluon Exchange (c) Direct Interaction

Figure 1.3: Examples of the different classes of gluon-gluon interaction [16]. (a) Interaction via quark exchange. (b) Interaction via gluon exchange. (c) Direct interaction.

1.4 Asymptotic Freedom and Quark Confinement

The modification of the effective electromagnetic coupling strength as a function of distance (or equivalently momentum transfer Q) is a well-known property of QED that can be understood by the effect of screening from pairs of virtual electrons and positrons. Consider the vacuum surrounding an electron where short-lived e^+e^- pairs are constantly being created and annihilated. The presence of the electron polarizes this cloud of virtual particles, so that the charge felt by a distant test particle is decreased. As the test particle is brought closer to the electron, it feels less of the polarized vacuum; thus the effective charge increases.

A similar effect is seen in QCD where virtual $q\bar{q}$ pairs tend to screen the color charge in much the same way. However, there is one very important difference in QCD: the gluons themselves carry color charge. Unlike the photon, which can only interact with charged particles and not other neutral photons, gluons are able to interact directly with each other as shown in Fig. 1.3(b) and 1.3(c).

The polarization of virtual gluons in the vacuum actually has the opposite effect of polarized $q\bar{q}$ pairs. It enhances the color field, a phenomenon known as 'antiscreening'[3]. The effective coupling strength in the 'one-loop' approximation – valid for small α_s or alternatively large Q – is as follows [19–21]:

$$\alpha_s^{\text{eff}}\left(Q^2\right) \approx \frac{4\pi}{\left(11 - \frac{2}{3}n_f\right)\ln\left(Q^2/\Lambda^2\right)}, \tag{1.3}$$

where Q is the momentum transfer, n_f is the number of quark flavors, and $\Lambda \approx 200$ MeV is a dimensional parameter that defines the QCD scale.

The number of quark flavors is sufficiently few ($n_f = 6$) that the antiscreening behavior of the gluons wins out over the screening of the quarks[4]. For larger momentum

[3] An intuitive way to qualitatively understand antiscreening is to consider the color magnetic properties of the gluon. As spin-1 particles, colored gluons act as permanent magnetic dipoles that align themselves to an applied field. Because of the relation $\epsilon\mu = 1$ (in units where c=1) between the dielectric constant, ϵ, and the magnetic permeability, μ, paramagnetism ($\mu > 1$) implies antiscreening ($\epsilon < 1$) [18].

[4] At RHIC energies, only up, down, and strange quarks contribute significantly in thermal equilibrium.

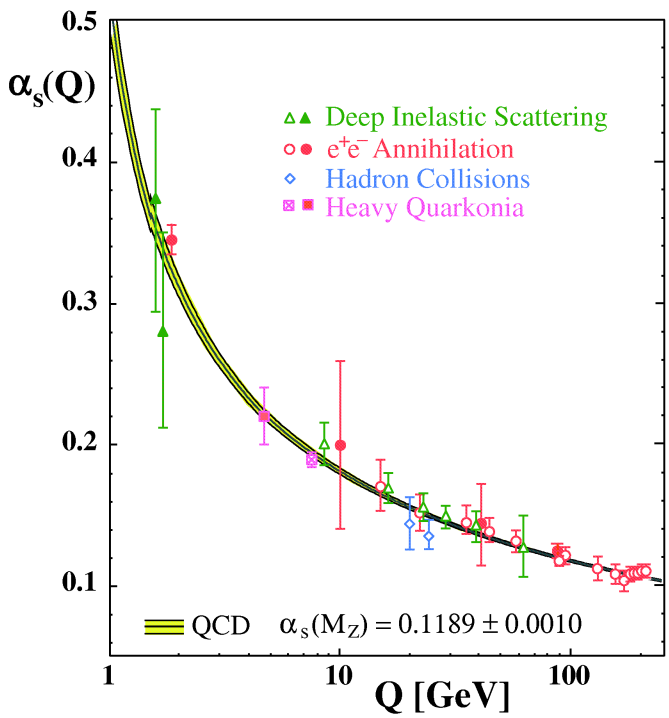

Figure 1.4: A summary of existing measurements of the strong coupling constant as a function of energy scale, taken from [22]. Open and closed symbols use NLO and NNLO calculations, respectively, to extract α_s from their analysis.

transfers, which correspond to shorter distances probed, the effective coupling strength approaches zero, see Fig. 1.4. This essential property of the strong force, referred to as 'asymptotic freedom' [20, 21], implies that for extremely high-energy collisions, the scattered quarks within the nucleon may be treated as free, non-interacting particles.

The flip-side of asymptotic freedom is confinement, meaning that for increasingly large separations between quarks, the force between them never goes to zero. Confinement is believed to be responsible for the continued failure of searches for individual, free quarks, as the energy required to separate them would be infinite. While the non-perturbative ($\alpha_s > 1$) nature of this regime makes analytical proof of confinement untenable, it is possible to formulate QCD on a discrete set of space-time points (known as the lattice [23]) to calculate the force in the strong-coupling limit [24].

When a quark and antiquark are pulled apart, for example in an accelerator environment by their own kinetic energy, the gluon fields between them stretch into narrow tubes (known as strings) until eventually the potential energy in the field is greater than the mass of a $q\bar{q}$ pair. When it is energetically favorable, new $q\bar{q}$ pairs are produced and all particles remain confined to colorless mesons and baryons. This hadronization

Charm is suppressed by a factor of $e^{-m_c/T}$, where m_c is the mass of the charm quark (see Appendix A) and T is the temperature.

process, referred to alternatively as fragmentation or string breaking, is responsible for the 'jets' of hadrons that show up in particle detectors instead of the originally scattered quarks.

1.5 The QCD Phase Diagram

The properties of the strong force give rise to a rich structure with distinct phases of QCD matter, shown in Fig. 1.5 as a function of temperature (T) and baryon chemical potential (μ_B)[5]. At low temperatures, partons (quarks and gluons) are confined within composite structures (protons and neutrons), which are collectively bound into nuclei. Under normal conditions, strongly interacting matter is in a mixed phase, with droplets of nuclear matter surrounded by regions of vacuum. At temperatures above the nuclear binding energy ($\approx 1-10$ MeV), or at values of μ_B below the phase transition, the nuclear matter evaporates into a hadron gas. Because of the similarity between the (residual) strong force between nucleons and the Van der Waals' attraction between molecules in a liquid, the transition is expected to be first-order at low temperatures[6] [25].

Starting in the lower left corner of Fig. 1.5 and increasing μ_B at low temperature, one first crosses the liquid-gas transition into nuclear matter. Increasing μ_B further corresponds to more and more compressed nuclear matter, until at some point, one crosses over to quark matter. This quark matter is superconducting due to the formation of diquark 'Cooper pairs', analogous to the pairing of electrons into 'quasi-bosons' that is responsible for superconductivity in solid-state physics. The fact that diquarks are necessarily colored objects means that the resulting condensate gives mass to the gluons via the Anderson-Higgs mechanism [26, 27]. Thus, the system is referred to as a 'color superconductor'.

In fact, Fig. 1.5 is really a simplification of the rich phase structure at high density. Because quarks come in three colors and three light flavors (up, down and strange), the different possible pairings of quarks into Cooper pairs can lead to quite different behaviors. At very high densities ($\mu_B >> m_s$) where SU(3) flavor symmetry is restored and the interaction strength is weak due to asymptotic freedom, reliable calculations show that the favored pairings are invariant under the simultaneous transformation of color and flavor. This phase is referred to as Color-Flavor Locked (CFL) [28]. At lower densities where the strange quark mass must be taken into account ($m_s > m_{u,d} \neq 0$), the phase structure is less certain and a number of different phases may exist. See [29] for a review of the phase structure of quark matter.

The most promising chance for observing quark matter at such high densities is in

[5] Increasing baryon chemical potential (μ_B) increases the net baryon density. μ_B corresponds to the amount of energy that would be added with the addition of one baryon to a system held at constant volume and entropy. In nuclear matter, where the density is empirically shown to be nearly constant, the energy of adding one nucleon is just the nucleon mass minus the binding energy ($\approx 930-940$ MeV).

[6] First-order phase transitions are characterized by 'latent heat', an amount of energy absorbed or released in crossing the transition.

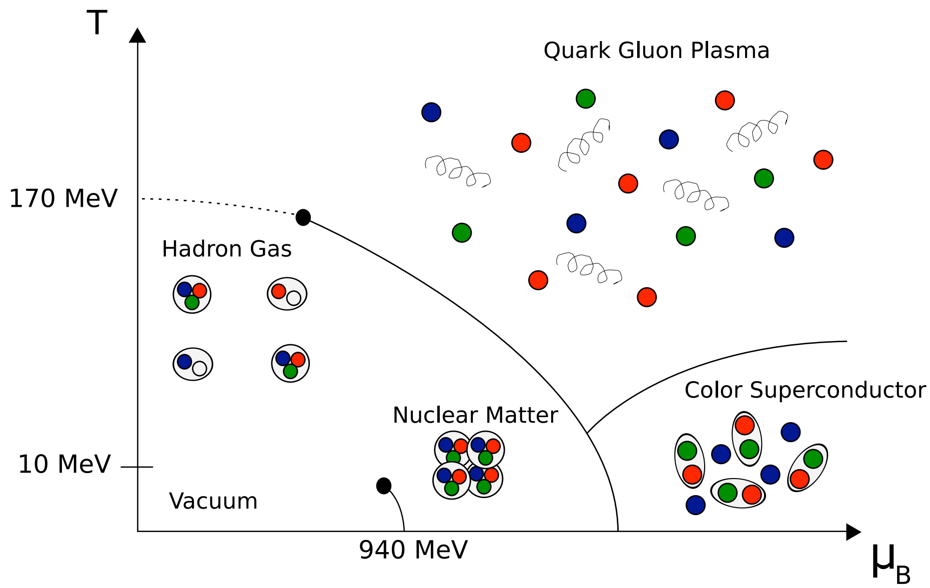

Figure 1.5: A simplified representation of the QCD phase diagram. The vertical axis is temperature (T) and the horizontal axis is baryon chemical potential (μ_B).

the cores of neutron stars that have collapsed under their own gravity. A review of theoretical developments and observational data related to compact stars can be found in [30].

Returning to the origin at $\mu = T = 0$ in Fig. 1.5 and heating the vacuum without preference for quarks over antiquarks (i.e. moving vertically along the temperature axis), a gas of mostly pions is first formed. The low temperature system is characterized by a number of order parameters (e.g. chiral symmetry breaking, confinement). With rising temperature, entropy eventually wins out, and one crosses into a state, known as the Quark Gluon Plasma (QGP) [31, 32], where this ordering melts away. The existence of a transition from a hadronic to a partonic phase is supported by lattice calculations performed at finite temperature and $\mu_B = 0$. The results point to a rapid cross-over, at a critical temperature of $T_c \approx 170$ MeV, for thermodynamic variables related to the degrees of freedom of the system [33, 34]. Heating the vacuum to sufficiently high temperatures should result in a relativistic gas of weakly interacting quarks and gluons, as a consequence of asymptotic freedom. It is believed that the entire universe existed in a weakly interacting QGP state around the first few microseconds after the Big Bang. While the QGP at very high temperatures is weakly interacting, this is not the case near the cross-over, where results from heavy ion collisions suggest the interactions are quite strong [35–38].

At non-zero μ_B, the current consensus is that the phase boundary changes from a cross-over to a first-order transition at a critical end-point, in the vicinity of which large fluctuations in thermodynamic variables should be observable. Lattice calculations at finite densities are complicated by the 'fermion sign problem' [39], and the precise location of the critical point is very dependent on the value of the quark mass [40]. There is hope from initial studies of Pb+Pb collisions [41] in the range $\sqrt{s_{\mathrm{NN}}} = 5 - 15$ GeV that the location of the critical point can be discovered experimentally. At present, a low-energy scan in 2010 is planned at RHIC to further investigate this topic. Future critical end-point searches are also planned for the CBM experiment at FAIR and the NA49 experiment at SPS.

1.6 Heavy Ion Collisions

The only known technique for exploring the properties of QCD matter at high temperatures in the laboratory is the collision of heavy nuclei. A sizeable fraction of the kinetic energy of the two relativistic ($E \gg m_0$) nuclei is released into a small region from the near simultaneous collisions of many nucleons.

Fixed target experiments at Brookhaven's AGS and CERN's Super Proton Synchrotron (SPS) have recorded collisions of light ions up to Au+Au and Pb+Pb at center-of-mass energies per nucleon ($\sqrt{s_{\mathrm{NN}}}$) from 2 to 17 GeV. The highest energies achieved to date have been at RHIC, where billions of d+Au, Cu+Cu, and Au+Au collisions have been recorded at energies up to $\sqrt{s_{\mathrm{NN}}} = 200$ GeV. Pb+Pb collisions at CERN's Large Hadron Collider (LHC) are expected to begin in 2009 at energies up to $\sqrt{s_{\mathrm{NN}}} = 5.5$ TeV.

A vast collection of experimental observables has been measured, relating detectable signals to the properties of the matter produced in heavy ion collisions. While no unambiguous signal of color deconfinement has been seen, the preponderance of evidence suggests the system produced in RHIC collisions has an extremely high energy density that is inappropriate to describe in terms of hadronic degrees of freedom. Additionally, the constituents of this system appear to interact very strongly within the produced medium.

For a thorough overview of recent experimental and theoretical developments in heavy ion collisions, see the proceedings of the 'Quark Matter' conference series [42–44] and the 'White Papers' from the four RHIC experiments [35–38].

1.6.1 Energy Density

The energy density of the system produced in Au+Au collisions can be estimated using the approach pioneered by Bjorken [45] and previously formulated in [16]. Energy density is just the amount of energy contained in some volume. That volume for a head-on collision can be taken as a cylinder with transverse area equal to that of the gold nucleus, $\mathscr{A}$. The length of the cylinder will grow with time as the system expands longitudinally due to the large initial momenta of the nuclei. As such, the choice of length is actually a choice of the time at which the system can be considered to reach local thermodynamic equilibrium. At one extreme, one could choose the longitudinal extent immediately after the two Lorentz-contracted nuclei collide (of order 0.1 fm). However, there is no reason to think that the system has approached any sort of equilibrium at that instant [35]. Instead, the measured magnitude of elliptic flow (see Sect. 1.6.2) can place an upper limit on the equilibration time of $\tau_0 \lesssim 1 \to 2$ fm/c [46].

Now that the volume of the initial system is known, it is necessary to estimate the energy contained within it. The relevant energy is not that carried initially by the colliding nuclei, but rather the energy of the produced particles. It is natural, therefore, to choose the hadrons produced roughly transverse to the collision for the estimate. The energy density can be estimated as

$$\epsilon_0 \approx \frac{\langle E_T \rangle \, dN/dy \, \Delta y}{2\tau_0 \mathscr{A}} \approx \frac{\sqrt{(0.500 \text{ GeV})^2 + m_\pi^2}\,(700)\,(3/2)}{(1 \to 2 \text{ fm})\, \pi\, (6.5 \text{ fm})^2} \approx 4 \to 2 \text{ GeV/fm}^3 \tag{1.4}$$

where $\langle E_T \rangle$ is the average transverse energy of hadrons and $dN/dy \, \Delta y$ is the number of hadrons produced in the mid-rapidity[7] interval $-1 < \eta < 1$. It is assumed that the majority of hadrons are pions [47] with an average transverse momentum $\langle p_T \rangle = 500$ MeV/c [35], and with positive, negative, and neutral pions equally represented. To estimate the *total* number of mid-rapidity particles using the measured *charged* hadron multiplicity [48], one must account for the undetected *neutral* pions, hence (700)(3/2). The radius of the gold nucleus is taken to be 6.5 fm.

Even this conservative[8] lower-bound on the initial energy density exceeds the value predicted by lattice calculations at the cross-over ($\sim$ 1 GeV/fm^3) [34]. Furthermore, it is an order of magnitude greater than the energy density of the gold nucleus ($\sim$ 160 MeV/fm^3) and at least five times greater than that of the proton ($\sim$ 450 MeV/fm^3, using $r_p = 0.8$ fm). Therefore, this system is likely better described in terms of quark, antiquark and gluon degrees of freedom, as opposed to hadronic degrees of freedom. After all, how is one to understand five protons occupying the same space?

1.6.2 Azimuthal Anisotropy

For off-center collisions of gold nuclei, the overlapping region that is the source of particle production has a pronounced initial state anisotropy, see Fig. 1.6(a). If the particles did not interact after their initial production, the azimuthal distribution of outgoing particles would leave no trace of this asymmetrical source. The magnitude of the final state azimuthal anisotropy ($v_2 = \langle \cos 2\phi \rangle$) or ‘elliptic flow’ is shown in Fig. 1.6(b) as a function of collision centrality. The presence of flow is evidence that the constituents of the system are interacting in the earliest moments after the collision, since any isotropic expansion of the source acts to diminish the spatial asymmetry. Based on this reasoning, an upper-limit for the equilibration time was derived, which was used in the previous section to estimate the initial energy density of the system.

The unexpectedly large elliptic flow implies that the produced system is interacting at early times in a manner more closely resembling the conditions of a liquid than a gas.

[7] Rapidity is a measure of longitudinal velocity. Particles at mid-rapidity are produced roughly transverse to the collision axis. See Appendix B for a detailed discussion of kinematic variables.

[8] Any work done by the expanding system is neglected in the summation over final-state hadrons.

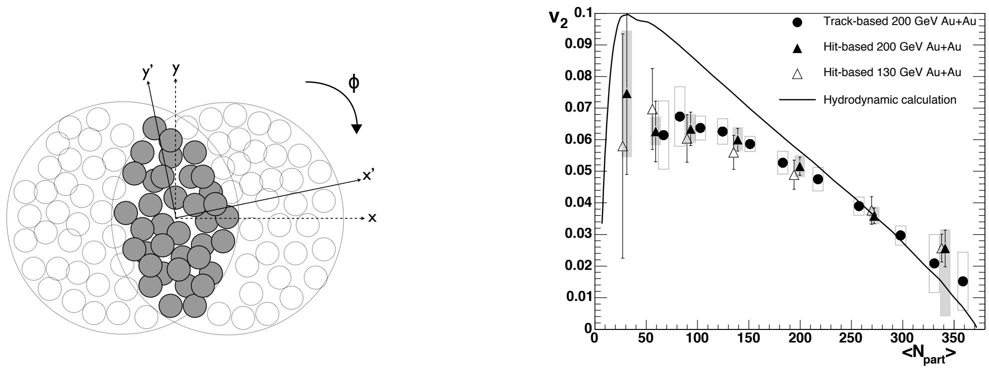

Figure 1.6: (a) Transverse view of an off-center collision [49]. The beam direction is into the page. (b) The magnitude of elliptic flow (v_2) measured by two techniques at $\sqrt{s_{\rm NN}} = 130$ and 200 GeV as a function of the number of nucleons participating in the collision ($N_{\rm part}$) [50]. Prediction of relativistic hydrodynamic model from [51].

The ordering of v_2 according to the mass of particle species (i.e. π, K, p, Λ) is compelling evidence that the early system undergoes a collective, pressure-driven expansion [52]. The agreement between ideal hydrodynamic models and measured flow results appears to be optimized for very early thermalization and an expansion characterized by a partonic equation of state [46]. The early equilibration time and the large initial energy density estimated in the previous section are suggestive of collective motion prior to hadronization. This interpretation is further supported by the intriguing observation that $v_2(p_T)$ appears to scale with constituent quark number ($n_q = 2$ for mesons and 3 for baryons) over the $p_{\rm T}$ region where hydrodynamics is applicable [53].

1.6.3 Transverse Momentum Distributions

Further evidence that the system in Au+Au collisions at RHIC energies is extremely dense and strongly interacting, comes from the study of the transverse momentum ($p_{\rm T}$) distributions of charged hadrons. In the collision of heavy ions, hard scattering events (i.e. large momentum transfers between partons) take place just as in p+p collisions, but the number of such scatterings scales with the number of binary nucleon-nucleon collisions ($N_{\rm coll}$). This assertion is supported by the fact that the direct production of photons, which do not interact via the strong force, scales with $N_{\rm coll}$ in Au+Au compared to p+p [56], as seen in Fig. 1.7(a).

The ratio of the charged hadron yield in Au+Au compared to the expectation of binary scaling – the nuclear modification factor $R_{\rm AA}$ – is found to be suppressed by a factor of about 5 at high-$p_{\rm T}$ [57–59]. This suppression is understood to be a consequence of final-state energy loss – 'jet quenching' – given the absence of the effect from d+Au collisions, where no hot, dense medium is created [55, 60, 61] (see Fig. 1.7(b)). In heavy ion collisions, a dense partonic medium is produced, causing high-$p_{\rm T}$ partons to lose

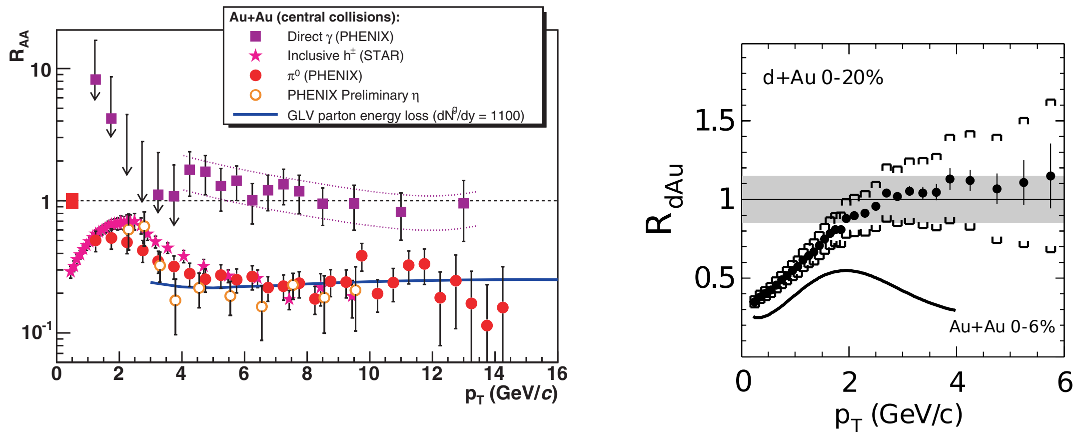

Figure 1.7: (a) PHENIX measurements of the nuclear modification factor R_{AA} for η and π^0 compared to direct photons, taken from [54]. (b) PHOBOS measurements of the nuclear modification in 0-20% central d+Au and 0-6% central Au+Au collisions [55].

energy in the form of induced gluon radiation, which eventually fragments into hadrons with much lower transverse momentum.

To better understand the energy loss mechanism and to constrain the properties of the medium, it is desirable to vary the path length traversed by produced jets. This can be achieved by studying the dependence of R_{AA} on collision centrality, on the angle relative to the reaction plane [62], and on the size of the colliding nuclei [63]. Various models have attempted to describe the centrality dependence of R_{AA} in Au+Au collisions, taking into account the initial geometry of the system. Because the geometry differs between Au+Au and the smaller Cu+Cu system, the centrality dependence of the Cu+Cu spectra presented in Ch. 7 provide an important test of our understanding of medium-induced energy loss.

1.6.4 Two-Particle Correlations

Dihadron correlations are a powerful tool for probing the properties of the medium produced in heavy ion collisions, particularly how it modifies the signature of back-to-back jets. Figure 1.8(a) [36] shows the azimuthal distribution of hadrons with $p_{\mathrm{T}} > 2$ GeV correlated to a trigger particle with $p_{\mathrm{T}} > 4$ GeV. Pairs taken from the same jet show up as a correlation at $\Delta\phi \approx 0$, while pairs taken from back-to-back jets result in a correlation at $\Delta\phi \approx \pi$. While the near-side correlation structure is similar for the p+p, d+Au, and Au+Au systems, the away-side correlation is strikingly absent in central Au+Au events [65]. The survival of the near-side correlation is a consequence of the requirement of a high-p_{T} trigger particle, which introduces a bias towards detecting those scatterings that occur near the surface. The disappearance of the away-side is likely due to the interaction of hard-scattered partons traversing a nearly opaque medium.

The energy and momentum of the away-side jet, however, must be present in the fi-

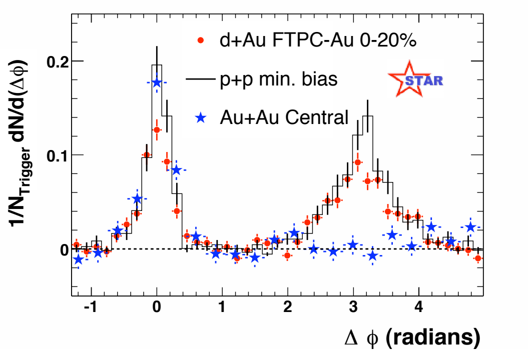

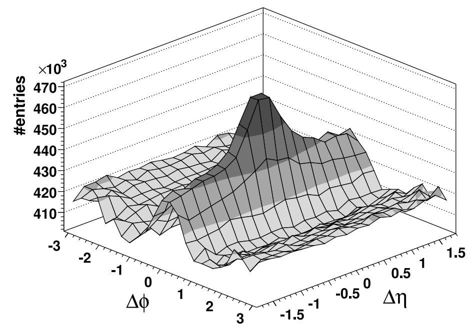

Figure 1.8: (a) Azimuthal correlations between pairs of high-p_T hadrons in p+p, d+Au, and Au+Au collisions [36]. (b) Raw correlation function in $\Delta\eta$ and $\Delta\phi$ for $3 < p_T^{trig} < 4$ GeV/c and $p_T^{assoc} > 2$ GeV/c [64]. Notice the extended ridge structure on the near side ($\Delta\phi \sim 0$).

nal state, motivating the measurement of correlations between high-p_T triggers and the excess of lower-p_T associated particles [66, 67]. Such measurements should be particularly sensitive to the precise nature of the jet-medium interaction. Figure 1.8(b) [64] shows a novel feature unique to Au+Au collisions: correlated particle production at small $\Delta\phi$ and extended in $\Delta\eta$ known as the 'ridge'. This phenomenon is the subject of active theoretical research, and while many proposed mechanisms can qualitatively describe the 'ridge', the origin of the structure is still not well understood.

Detailed measurements of correlations can elucidate the underlying mechanisms responsible for particle production. While many experimental properties of the ridge have already been measured, the PHOBOS triggered correlations analysis outlined in Ch. 8 adds an important piece to the puzzle. By extending the measurement to include correlated particles separated longitudinally by up to four units of pseudorapidity ($\Delta\eta = 4$), the results presented in Ch. 9 can be used to discriminate between the various proposed mechanisms for the ridge.

1.7 Goal of this Thesis

This thesis presents results on charged hadron transverse momentum distributions in Cu+Cu and Au+Au collisions, as well as long-range, p_T-triggered, two-particle correlations in Au+Au collisions. The measurement of high-p_T yields in the new Cu+Cu collision system will be used to clarify the jet quenching mechanism, in particular the dependence on the size and shape of the produced medium. The measurement of triggered correlations provides important data to constrain possible mechanisms for the distribution of jet energy deposited in the medium. In particular, the much broader pseudorapidity acceptance of the new PHOBOS measurement will be used to test proposed theoretical explanations of the ridge correlation.

The analyses presented herein primarily used the multiplicity array, which recorded the angular positions of particles over a broad acceptance in a single layer of silicon, and the multi-layer Spectrometer arms, which measured the momentum of a small fraction of produced particles by tracking their trajectories through a magnetic field. The layout of the PHOBOS detector apparatus is described in Ch. 2; the procedures for processing the raw silicon signals are detailed in Ch. 3.

One of the main challenges in the smaller Cu+Cu system was the low multiplicity of produced particles. Special care was required to estimate the efficiency of the collision trigger for the accurate determination of event centrality. The procedures used to characterize collision events are described in Ch. 4. This includes the essential introduction of a new vertexing algorithm that was both efficient at low multiplicities and accurate enough for track finding.

Using a single layer of silicon to measure associated particles in the correlations analysis presented another challenge. While secondary tracks in the multi-layer Spectrometer could be rejected based on their deviation from the primary event vertex, secondary hits in the single-layer Octagon were only partially rejected using cuts on deposited energy. The remaining contribution suppressed the observed correlation, requiring a correction. Additionally, in central Au+Au events, the high hit density in the mid-rapidity Octagon necessitated a procedure to weight hits by the local occupancy. The techniques for dealing with secondaries and occupancy are detailed in Ch. 5, along with the reconstruction algorithms for hits and tracks from the energy deposited in detector pads.

2 The PHOBOS Experiment

The data presented in this thesis were collected by PHOBOS, one of four experiments at the Relativistic Heavy Ion Collider (RHIC). First collisions were provided by RHIC on June 12th, 2000; a few weeks later, PHOBOS submitted the first results on charged particle multiplicities at RHIC energies [68]. In the following years, collisions of p+p, d+Au, Cu+Cu, and Au+Au were recorded over a broad range of center-of-mass energies. As from 2006, the experiment stopped taking new data. The collaboration is now focusing its efforts entirely on data analysis.

2.1 Relativistic Heavy Ion Collider

The Relativistic Heavy Ion Collider (RHIC) [69, 70] at Brookhaven National Lab (BNL) was designed to collide heavy ions at center-of-mass energies up to 200 GeV per nucleon. Four experiments (STAR , PHENIX, PHOBOS, and BRAHMS) were built to study these collisions. The production and acceleration of beams of gold ions involves much of the existing infrastructure at BNL, as shown in Fig. 2.1 [71].

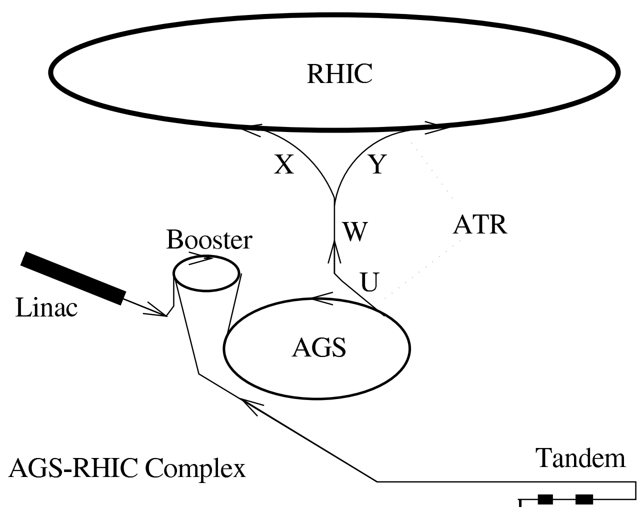

Figure 2.1: A diagram of the AGS-RHIC complex taken from [71]. Au^{+77} ions exit the AGS ring at U. Stripped of their final two electrons at W, Au^{+79} ions are injected into the two RHIC rings at X and Y respectively. See text for a description of the Tandem Van de Graaff. Energetic protons for the study of p+p or p+A collisions are supplied by the Linear Accelerator (Linac).

The process begins with the production of negatively charged Au^- ions from a pulsed sputter source at the Tandem Van de Graaff accelerator, which consists of two static potentials arranged in sequence. The negative ions are accelerated by the first potential (+15 MV) through a thin foil which strips them of some of their electrons. The now-positively charged ions then enter the second potential (-15 MV) where they are accelerated up to 1 MeV per nucleon. Stripped again upon exiting the Tandem Van de Graaff, ions with charge +32 are magnetically selected and transferred to the Booster synchrotron, where they are accelerated up to 95 MeV per nucleon. Another electron stripping is performed after exiting the Booster. The Au^{+77} ions are then injected into the Alternating Gradient Synchrotron (AGS) and accelerated to the RHIC injection energy of 10.8 GeV per nucleon. Leaving the AGS, ions are stripped of their final two electrons and transferred to RHIC for a final acceleration.

To carry the counter-rotating beams of heavy ions, RHIC consists of two quasi-circular rings, 3.8 km in circumference. Each ring is made up of six arc sections and six straight sections. Liquid helium-cooled, superconducting dipole magnets with a strength of 3.458 T bend the beam around the arc sections, while quadrupole magnets keep the beam tightly focused. In the middle of the straight sections lie the six interaction points. On either side of each interaction point, the two beams are brought together into a single beam-pipe by a pair of D0 magnets. Two DX magnets then steer the beams such that they cross at the interaction point.

Particles travel around the beam in bunches of $\sim 10^9$ ions. Two RF systems are used at RHIC: one at 28 MHz to accelerate the bunches captured from AGS, and another at 197 MHz to 'rebucket'[1] the ions into a tighter longitudinal profile ($\sigma_L \approx 25$ cm). As the bucket size is much smaller than the distance between bunches, many buckets are empty. For this reason, a 'crossing clock' is used to let experiments know when two filled buckets should be colliding.

2.2 PHOBOS Detector

The PHOBOS detector consisted of two main components: an array of multiplicity detectors covering almost the entire solid angle of produced particles, and a two-arm magnetic Spectrometer to study the detailed properties of a small fraction of these particles ($\sim$ 2%). Both components utilized silicon pad technology to detect charged particles. By minimizing the amount of material between the beam and the first silicon layer, PHOBOS was able to detect particles with very low momentum [72]. Although the design was optimized to search for signals of new physics at very low-p_T [73], the PHOBOS detector has proven quite capable of studying high-p_{T} phenomena as well. Additional subdetectors were added to aid in particle identification, event triggering and centrality determination. A diagram of the complete detector setup is shown in Fig. 2.2.

[1]Buckets refer to the positions along the beam at which particles can 'ride' the Radio Frequency (RF) wave.

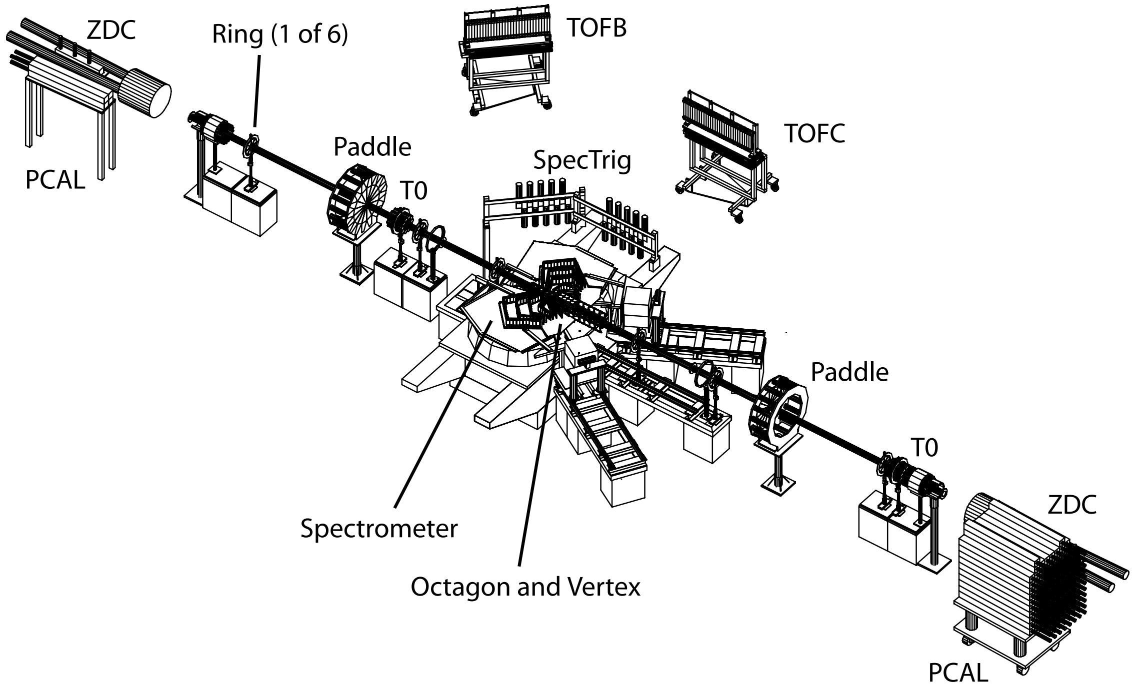

Figure 2.2: The complete PHOBOS detector setup in 2003. The calorimeters (see Sect. 2.2.3) were roughly three times further from the interaction point than shown.

2.2.1 Multiplicity and Vertex Detectors

The PHOBOS multiplicity array used single layers of silicon to measure the number and angular distribution of charged particles. Those particles produced at $\left|\eta\right| < 3.2$ were detected in the Octagon, a single-layer of silicon pad sensors that surrounded the beam-pipe in an octagonal barrel. Particles emitted at more forward angles were detected by six Ring counters, mounted perpendicular to the beam-pipe, extending the pseudorapidity coverage to $\left|\eta\right| < 5.4$. Above and below the interaction region, two layers of finely segmented silicon provided precision vertex resolution.

To maximize the precision of the very forward measurements, where particles traverse more beam-pipe material due to their small angle, the three sections of steel beam-pipe nearest the interaction region were replaced with lighter beryllium. The only noticeable gaps in the multiplicity array were from an attempt to reduce the material off of which low-momentum particles might scatter before detection in the Spectrometer.

Octagon Detector

The Octagon detector, shown in Fig. 2.3 [72], was 1.1 m long with a face-to-face diameter of 90 mm. Eight rows of thirteen silicon pad sensors were supported on a lightweight aluminum frame, through which cold water was run to cool the readout electronics. Sensors were removed from four faces in the regions immediately between the nominal

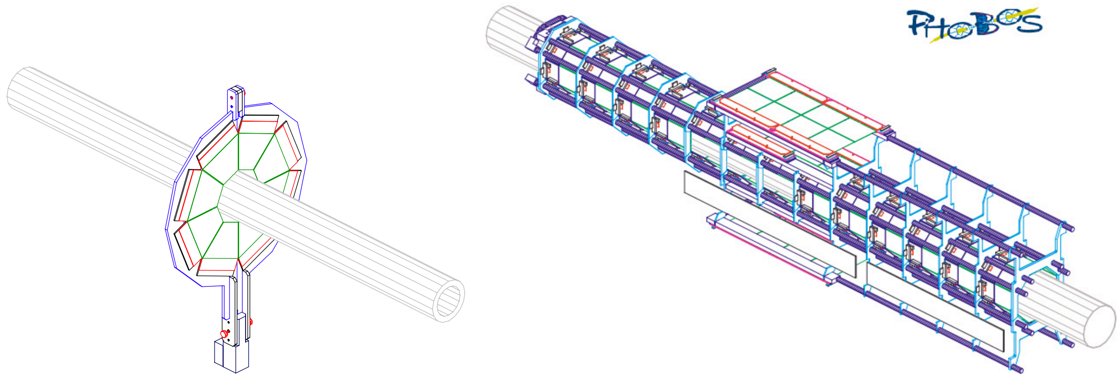

(a) Ring Detector (b) Octagon and Vertex Detectors

Figure 2.3: The PHOBOS multiplicity detectors [72].

vertex position and the Vertex and Spectrometer detectors. The thickness of the Octagon sensors, like all the silicon in PHOBOS, was specified to within 300 and 340 μm. Each 84 mm x 36 mm sensor was divided into four rows of 30 pads each. Despite the relatively large size of the pads (2.708 mm x 8.710 mm), the Octagon sensors achieved a signal-to-noise ratio comfortably above the design goal of 12-to-1.

Ring Detectors

The Ring detectors were used to detect charged particles at very forward angles (large pseudorapidity). The six Ring detectors were supported by carbon fiber mounts along with their readout electronics at distances of $\pm$1.13 m, $\pm$2.35 m, and $\pm$5.05 m from the nominal interaction point. Each detector consisted of eight trapezoidal sensors arranged in a ring extending 12 cm radially outward from an inner diameter of 10 cm (see Fig. 2.3 [72]). Each trapezoidal sensor had 64 pads arranged in eight rows of eight radial columns. Unlike the rectangular Octagon pads, those in the Rings were designed such that each would have approximately the same pseudorapidity coverage ($\Delta\eta \approx 0.1$). As such, the pad sizes ranged from 3.8 mm x 5.1 mm at small radii to 10.2 mm x 10.2 mm at the largest radii. The average signal-to-noise for Ring sensors was comparable to the Octagon.

Vertex Detector

The Vertex detector was designed to measure the location of the primary collision vertex within the range $|v_z| < 10$ cm to an accuracy of 0.2 mm in high multiplicity Au+Au events. The accuracy of the vertex position is important to parts of many PHOBOS analyses, for instance as a seed for the tracking algorithm in the Spectrometer. The detector consisted of two layers of finely segmented silicon pad sensors mounted on the Octagon frame, both above and below the interaction point. The collision position could then be reconstructed from two-point tracks that pointed back to a common vertex. While this was the preferred method in Au+Au events, different vertexing algorithms were used in lower multiplicity environments such as Cu+Cu and d+Au collisions (see Sect. 4.4).

The layers closer to the collision ($y = \pm 5.6$ cm), known as the 'Inner Vertex', had four sensors laid out in a line along the beam direction. The pads on each Inner Vertex sensor were arranged in four columns of 128 pads. In the azimuthal direction, the 12 mm long pads were similar in dimension to the Octagon. However, much greater precision was required along the beam direction, so the pads were only 0.473 mm wide.

The Outer Vertex layers ($y = \pm 11.8$ cm) each had two adjacent sets of four sensors aligned as before. On each sensor, the pads (24 mm x 0.473 mm) were laid out in two columns of 128 pads. Because of their smaller pad size, the Vertex sensors achieved a higher signal-to-noise than the Octagon sensors.

In addition to providing vertex information, these detectors were used to determine the charged particle multiplicities within a solid angle corresponding approximately to the removed Octagon sensors. For collisions at the nominal vertex position, the Inner Vertex covered $\left|\eta\right| < 1.54$ and the Outer Vertex covered $\left|\eta\right| < 0.92$. Both layers had an azimuthal extent of $\Delta\phi = 42.7°$. The upper 4 x 2 array of Outer Vertex sensors can be seen in Fig. 2.3 [72].

2.2.2 Spectrometer Detectors

For a small fraction of the particles produced in a collision, the momentum could be reconstructed using the PHOBOS two-arm Spectrometer. The multi-layered silicon pad detector tracked particles bending through a 2 T magnetic field. At lower momentum, the velocity-dependent energy loss of tracks was used to determine particle species (e.g. π, K, p). The Time-of-Flight (TOF) walls, together with the Time-Zero Counter (T0) detectors, extended this capability to higher momenta.

PHOBOS Magnet

The PHOBOS magnet was a conventional, room-temperature dipole magnet with vertical fields of opposite polarity on either side of the beam-pipe. The roughly 2 T magnetic field was generated by a 3600 amp current in four sets of copper coils, two above the Spectrometer and two below. The gap between the poles measured 158 mm, and the total bending power was ≈ 1.5 Tm. A photograph of the PHOBOS magnet before installation is shown in Fig. 2.4(a). Including the steel flux return yokes, the massive structure weighed about 45 tons[2].

The pole tips were shaped such that the first few layers of the Spectrometer resided in a region of very low magnetic field, see Fig. 2.4(b) [35]. Straight tracks from this region were used as seeds for the more complicated task of reconstructing the curved paths through the high-field region. The field was approximately constant and vertical in the high-field region, with a maximum value $B_y = 2.18$ T and B_x and B_z components of less than 0.05 T.

[2]This is approximately 3/4 the weight of an Abrams tank without the depleted Uranium armor upgrade.

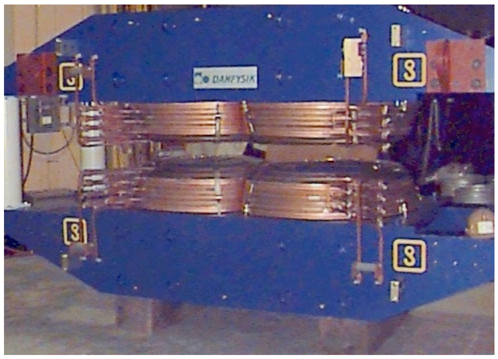

(a) PHOBOS Magnet

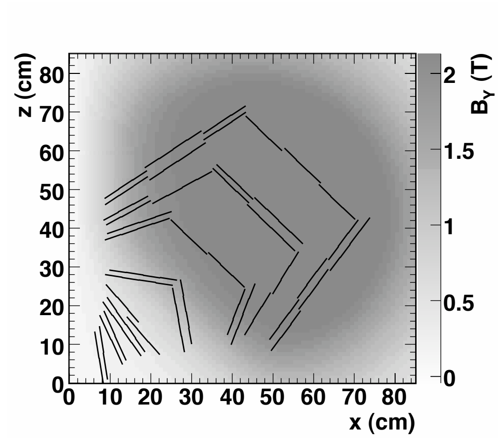

(b) Magnetic Field Map

Figure 2.4: (a) A picture of the PHOBOS magnet from late-1998 prior to installation. (b) The vertical magnetic field strength in the vicinity of one of the Spectrometer arms [35].

It was possible to switch the polarity of the magnetic field by reversing the direction of the current through the coils. The magnet polarity was typically reversed after each beam dump, to ensure similar statistics in both polarities. This symmetry of the detector was used to minimize certain systematic uncertainties, particularly in the analysis of particle ratios [74, 75].

Spectrometer Detector

The PHOBOS Spectrometer consisted of two arms on either side of the beam-pipe. Each arm consisted of 137 sensors arranged into sixteen layers and mounted on either side of eight water-cooled aluminum frames. As shown in Fig. 2.5(a) [35], the frames were attached to a carrying plate made of carbon-epoxy. This material was chosen because its non-conducting nature minimized vibrations from magnetic eddy currents. The carrying plate was mounted on rails so that the frames could be assembled outside the magnet and slid into place. The entire region between the magnetic poles was occupied by a light- and air-tight enclosure, which used circulating dry nitrogen to maintain a relative humidity $< 10\%$.

The Spectrometer contained five different sensor types, the details of which are listed in Table 2.1. The spatial positioning of the Spectrometer layers and their respective sensor types are shown in Fig. 2.5(b) [16]. The horizontal width of the silicon pads was kept small in all layers to maintain good resolution in the bending direction of tracks. The increased vertical dimension of the pads at large distances from the interaction point minimized the cost of the sensors at the expense of some decreased azimuthal resolution.

In total, the Spectrometer consisted of 135,168 separate channels. The algorithms that were used to process this volume of information into the trajectories of charged

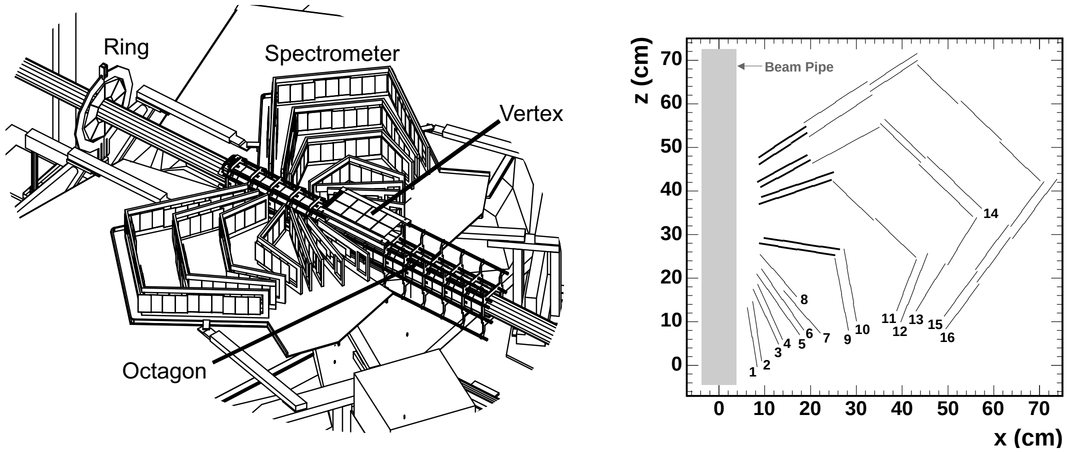

Figure 2.5: (a) The PHOBOS silicon detectors in the proximity of the interaction point. The top yoke of the PHOBOS magnet has been removed [35]. (b) Sensor layout in one arm of the PHOBOS Spectrometer. Layers are numbered and the Type 3 sensors indicated with thick lines [16].

Sensor Type	Number of Pads (horiz. x vert.)	Pad Size (mm x mm)	Sensor Placement (layer numbers)
1	70 x 22	1.000 x 1.0	1-4
2	100 x 5	0.427 x 6.0	5-8
3	64 x 8	0.667 x 7.5	9-16 (inner)
4	64 x 4	0.667 x 15.0	9-12
5	64 x 4	0.667 x 19.0	13-16

Table 2.1: Properties of the various Spectrometer sensor types. Type 3 sensors were only used in the region nearest the beam, see Fig. 2.5(b).

particles are discussed in Sect. 5.2.

Time-of-Flight Wall

The Time-of-Flight (TOF) wall was installed to extend the PHOBOS Particle Identification (PID) capabilities to high transverse momentum. The wall consisted of two sections of 120 scintillators – wall ‘B’, aligned 45° to the beam at a distance of 5.4 m, and wall ‘C’, aligned parallel to the beam at a distance of 3.9 m [76]. Together the two sections covered a pseudorapidity range of $0 < \eta < 1.24$.

The Bicron BC404 plastic scintillators were chosen for their good timing resolution (1.8 ns), moderate attenuation (1.6 m), and maximum emission wavelength (408 nm), which is close to the typical peak response wavelength (420 nm) of a fast Photomultiplier Tube (PMT). The scintillators were 20 cm in length with an 8 mm x 8 mm cross-sectional area.

Hamamatsu R5900 PMTs were connected to groupings of four scintillators at each end

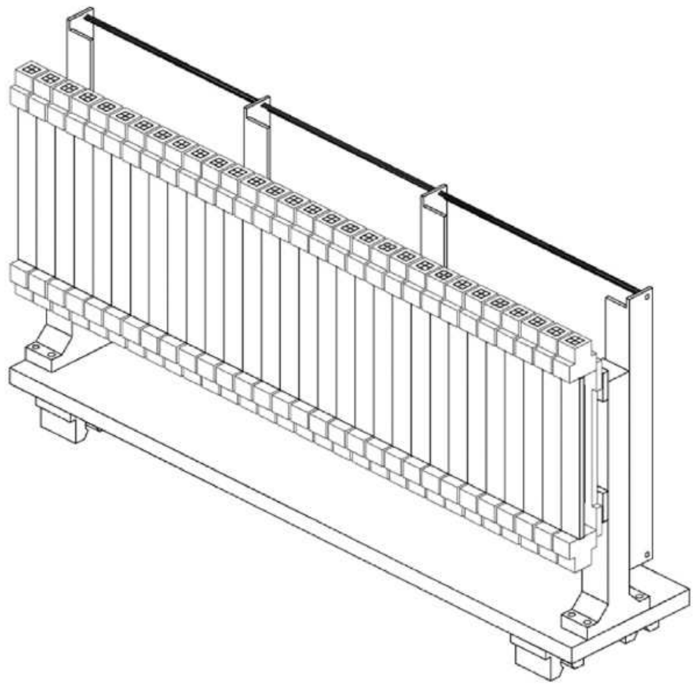

Figure 2.6: Schematic drawing of one TOF wall [35].

(see Fig. 2.6). The PMTs had a segmented 2 x 2 anode, but the four channels shared the same photocathode leading to some cross-talk between adjacent channels (< 10%). The anode signal from each PMT was split in two: one part was sent to an Analog-to-Digital Converter (ADC) after a 400 ns cable delay for a pulse-height reading, while the other part was sent to a leading-edge discriminator near the PMT. The discriminator signal was then sent to a Time-to-Digital Converter (TDC) for timing information with 25 ps/channel sensitivity. The simultaneous measurement of pulse height and timing allowed for slewing corrections, which improved the overall timing resolution of the TOF to better than 100 ps.

Since each scintillator was read out at both the top and bottom, vertical position information was available from the difference in timing signals and pulse heights. This information aided in the extrapolation of Spectrometer tracks to the TOF wall. The position resolution achieved in studies of cosmic rays and radioactive sources was 10 mm based on timing and 37 mm based on the ratio of pulse heights.

2.2.3 Calorimeters

In order to classify events based on the impact parameter of the colliding nuclei, detectors were designed to detect ‘spectators’, i.e. particles that did not directly participate in the collision. The energy of *neutron spectators* was measured with the Zero-Degree Calorimeter (ZDC) detectors placed directly downstream of the collisions. Adjacent to the ZDCs, in the region where protons were swept out of the beam-pipe, forward Proton Calorimeter (PCAL) detectors were installed to tag collisions with *proton spectators* [16].

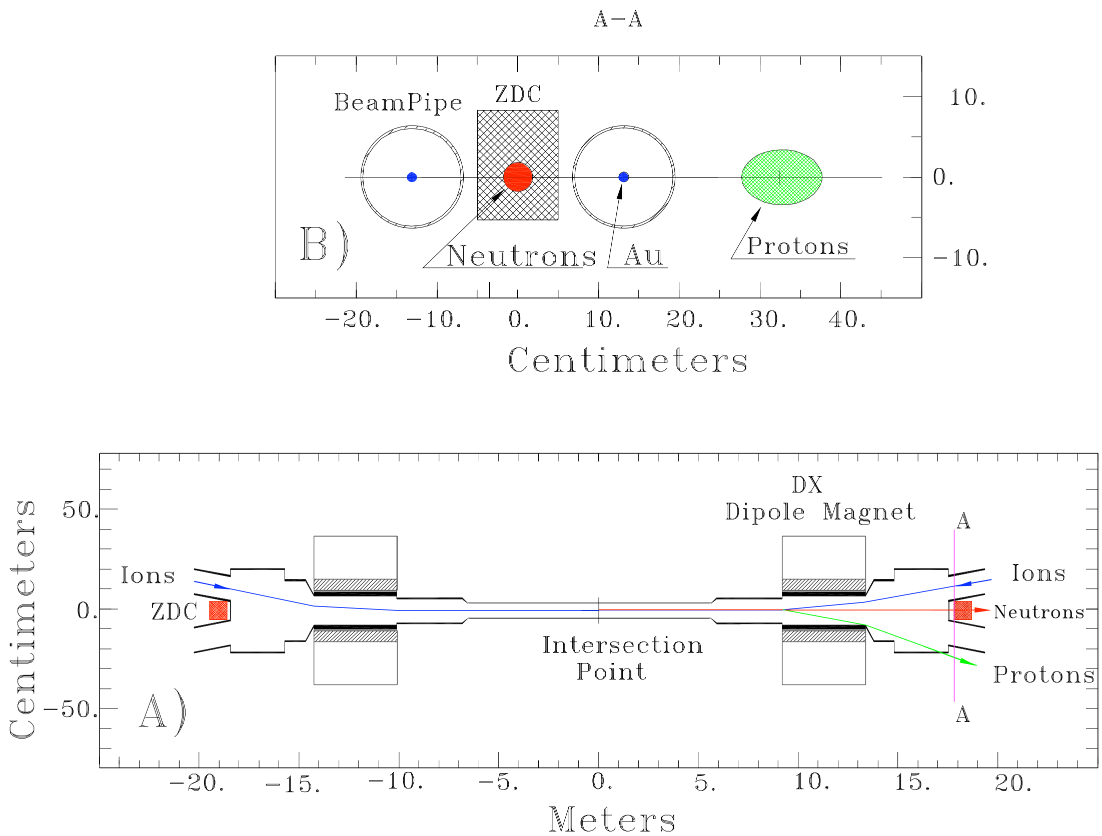

Figure 2.7: Plan view (bottom) and “beam’s eye" view (top) of the ZDC location and the paths taken by gold ions, protons, and neutrons [77].

Not shown in Fig. 2.2, the Spectrometer Calorimeter (SpecCAL) was installed in 2004 using a similar design as the PCALs. Because its goal was to provide calorimetric information for reconstructed high-p_T tracks, the SpecCAL was located beyond the positive Spectrometer arm.

Zero-Degree Calorimeters

High-energy collisions of nuclei are known to cause neutron emission by ‘evaporation’ [77]. At the RHIC beam energy of 100 GeV per nucleon, these fragments diverge no more than 2 mrad from the beam direction. The region immediately behind the DX magnet is especially well-suited for the measurement of free neutrons, since all charged particles are swept away by the magnet. The design of the ZDC modules was restricted mostly by the limited space in the "zero-degree" region. As shown in the lower panel of Fig. 2.7 [77], the width of the calorimeter could not exceed 10 cm ($\sim$ 1 interaction length (Λ_I) in tungsten). The calorimeters were designed to minimize energy loss from the transverse leakage of the shower. They were not segmented in the transverse direction, so no information on the transverse position of neutrons was available.

The ZDCs were hadron shower, sampling calorimeters that consisted of three identi-

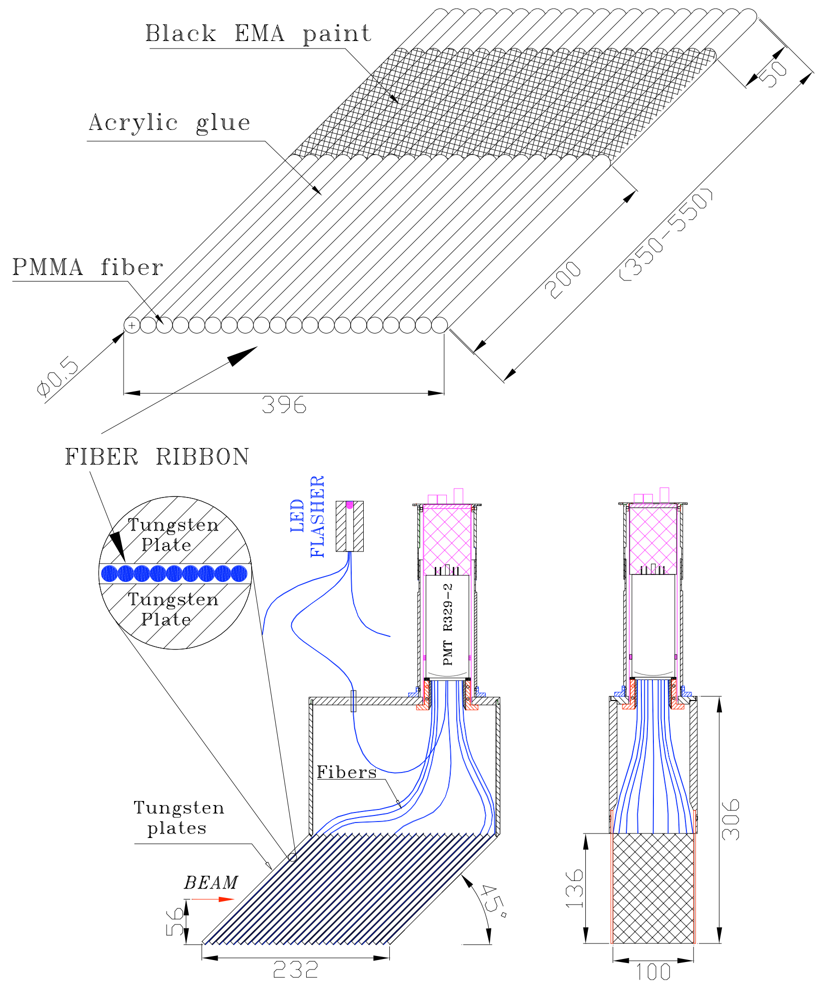

Figure 2.8: Design of a tungsten ZDC module. Dimensions shown are in millimeters [77].

cal modules. Each module was constructed from single-layer ribbons of Poly-methyl-methacrylate (PMMA) optical fibers (0.5 mm wide) sandwiched between 27 tungsten alloy plates (5 mm wide). The length of one module corresponded to two nuclear absorption lengths. The PMMA fibers sampled the Čerenkov radiation emitted by shower secondaries. The optical fibers were placed at a 45° inclination to coincide with the approximate Čerenkov angle for near-luminous particles in PMMA. The fibers from one module were collected and attached to a single PMT. The detailed design is illustrated in Fig. 2.8 [77].

Pairs of identical ZDC detectors were positioned roughly at ±18 m at each of the four RHIC experiments for use in triggering, event characterization, and luminosity monitoring for RHIC beam operators.

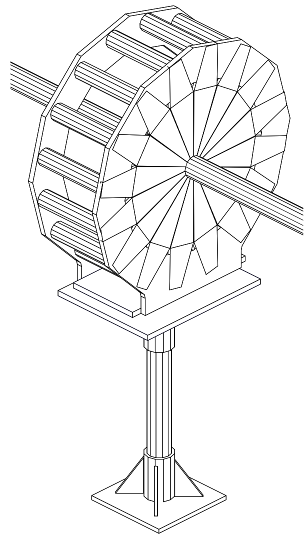

(a) Paddle Counter

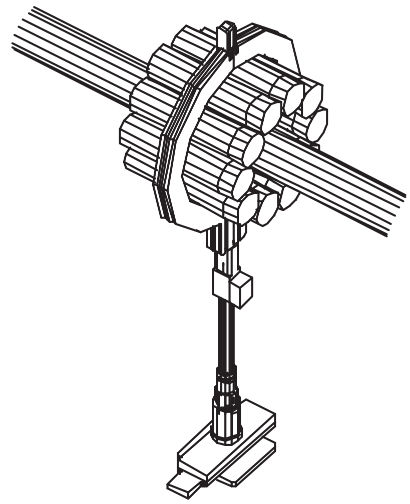

(b) Time-Zero Counter (T0)

Figure 2.9: Schematic diagrams of trigger counters: (a) Paddle counter [79] (b) Time-Zero Counter (T0).

2.2.4 Trigger Detectors

A number of different detectors were used by PHOBOS to trigger on collision events with desirable properties. The primary trigger detectors used in nucleus-nucleus collisions were the two Paddle counters and the ZDCs. The T0s were used to trigger on collision vertex in addition to providing a start-time for the TOF walls. Before the d+Au run, the Spectrometer Trigger (SpecTrig) was commissioned to increase the rate of events with a high-p_T track by selecting co-linear combinations of SpecTrig hits, TOF hits, and the real-time T0 vertex position [76]. There were also Čerenkov detectors [78], two sets of 16 Lucite radiators arranged around the beam-pipe at ±5.5 m. However, they were no longer used after the installation of the superior T0s.

Paddle Counters

The Paddle counters [79] were used as the primary event trigger in the Au+Au and Cu+Cu physics runs. The total energy deposited in the Paddles was also used to determine event centrality during these runs. The Paddle counters were two arrays of 16 wedge-shaped scintillators located at ±3.21 m from the nominal interaction point. They covered the pseudorapidity region $3 < |\eta| < 4.5$, with an active area of 99%. As a minimum bias trigger, plastic scintillators have a number of natural advantages. Their large dynamic range (from one Minimum Ionizing Particle (MIP) up to 50 per collision) allowed good energy resolution from the most peripheral to the most central collisions; good timing resolution meant they could be used to quickly select collisions from a desired vertex range; and high tolerance for radiation was essential given their proximity to the beam. A diagram of a Paddle counter is shown in Fig. 2.9(a) [79].

Each scintillator was 18.6 cm long and 0.95 cm thick, growing in width from 1.9 cm to 9.5 cm from the inner to outer edge. While the scintillators sat perpendicular to the beam, the PMTs were aligned parallel. This necessitated a two-component light-guide, joined by an aluminized 45° mirror.

The full Paddle counters achieved a time resolution of about 1 ns, sufficient to distinguish between collision and background events (see Sect. 4.1). The Paddles had an efficiency of 100% in central and semi-peripheral Au+Au events, which made them effective in triggering without bias.

Time-Zero Counters

There were two Time-Zero Counters (T0s) positioned at $z = \pm 5.3$ m, each consisting of ten Bicron BC800 Čerenkov radiators arranged in a ring with diameter 151 mm. However, the positions of the T0s were not fixed. During the d+Au run, for example, the T0 on the lower multiplicity deuteron side was moved to 2.6 m from the interaction point. The Čerenkov radiators were 25 mm thick and 50 mm in diameter. They were coupled to fast Hamamatsu R2083 PMTs of the same diameter.

Because of their fast response time, the T0s provided a precise start-time measurement for the TOF, as well as real-time vertex information for use in triggering. The T0s had an intrinsic time resolution of 110 ps, allowing a much more precise determination of the event vertex than the Paddles. However, their smaller geometrical acceptance resulted in some loss in efficiency for very low multiplicity events. A diagram of one of the T0s is shown in Fig. 2.9(b).

2.2.5 Data Acquisition

The digitized signals from the trigger detectors were used to quickly decide whether to accept an event. A description of trigger algorithms can be found in Sect. 4.1. For events that passed the trigger, the full state of the PHOBOS detector was read-out and sent to the DAQ for processing. The various parts of the PHOBOS DAQ system are shown in Fig. 2.10 [80].

The DAQ received data from over 135,000 silicon channels and 2,000 scintillator channels. The digitized silicon signals from the Front-End Controllers (FECs) (see Sect. 3.1) were transmitted via optical fibers to a 24-node processing farm, connected to a RACEway switching network and residing in a single VME crate [81]. The main purpose of the farm was to check for consistency and compress the silicon data. Because corrections for Common-Mode Noise (CMN) and cross-talk between silicon channels were done offline after processing, the compression used a lossless Huffman algorithm [82]. Leveraging the fact that most channels in the low-occupancy Spectrometer and Vertex detectors were empty in any given event, the algorithm achieved a compression factor of four-to-one [80].

The signals from the scintillators were digitized in one FASTBUS crate (Paddles, TOF, T0s, ZDCs) and one VME crate (PCAL, SpecCAL, SpecTrig). These signals were combined with

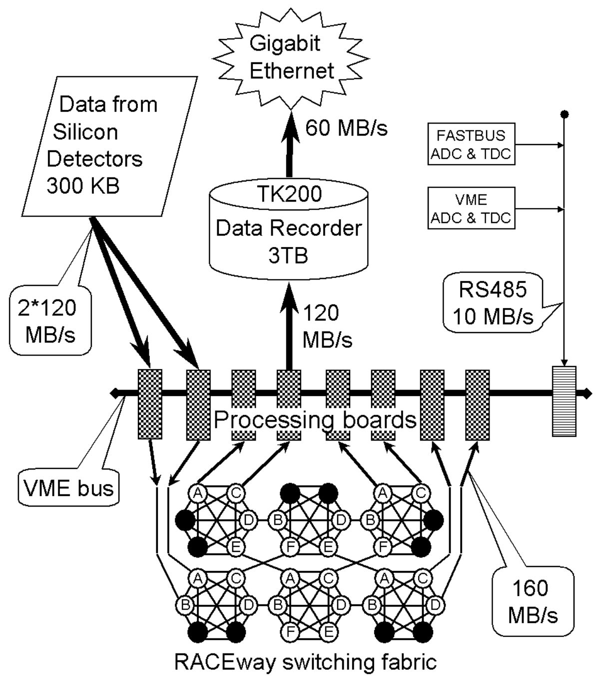

Figure 2.10: Diagram of the PHOBOS Data Acquisition (DAQ) system from [80].

the processed silicon data by the Event Builder into 1 GB files referred to as ‘sequences’ (roughly 10,000 events). The Event Builder periodically distributed recent events to online monitoring computers for on-the-spot reconstruction.

A TK200 data recorder from the Conduant Corporation acted as a buffer between the output of the processor farm and a Gigabit ethernet transfer to High Performance Storage System (HPSS) tape. The TK200 had a 3.2 TB capacity corresponding to 22 hours of storage at maximum input. After the most recent upgrade in 2004, the DAQ system reached a trigger rate of 575 Hz, a processing speed of 200 MB/s, and a data-sinking rate to HPSS of 50 MB/s [80].

3 Silicon Signal Processing

After the electronic signals had been read-out from the PHOBOS silicon detectors, they still needed to be processed before they could be used to determine the positions and deposited energies of detected particles. This processing included the subtraction of pedestals and Common-Mode Noise (CMN), the calibration of gains, and the determination of dead channels.

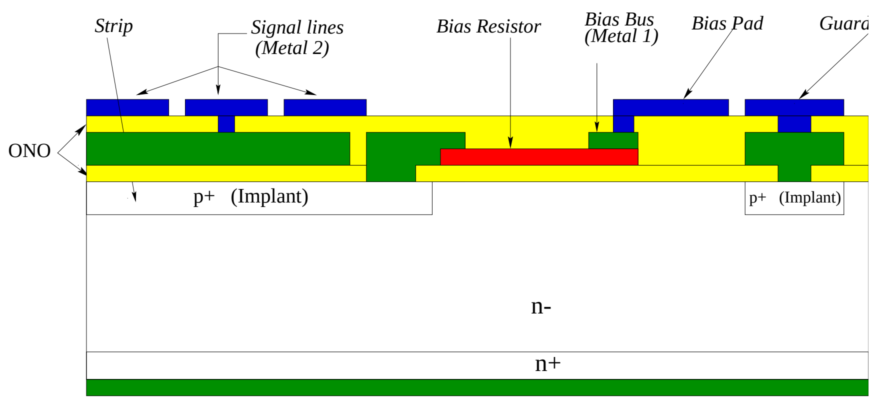

Figure 3.1: Cross-section of a silicon sensor used in PHOBOS [83].

3.1 Silicon Sensor Design and Readout

Semiconducting materials, such as silicon, are characterized by a narrow energy gap between the valence electron band and the conduction band (of order 1 eV). Silicon can be 'doped' by the addition of impurities with different numbers of valence electrons. If the impurity has more valence electrons than silicon (e.g. arsenic), the resulting semiconductor is called *n-type*, due to the excess of negative charge carriers. If the impurity instead has fewer valence electrons (e.g. boron), it is a donor of 'holes', vacancies in the valence band that can move through the semiconductor under the influence of an external field. Due to the excess of positively charged holes, this is called a *p-type* semiconductor.

At the interface between two such types of semiconductor (known as a *p-n junction*), excess electrons drift across the boundary and recombine with holes[1], leading to a re-

[1]Similarly holes drift into the n-type region to recombine with electrons, albeit with lower mobility.

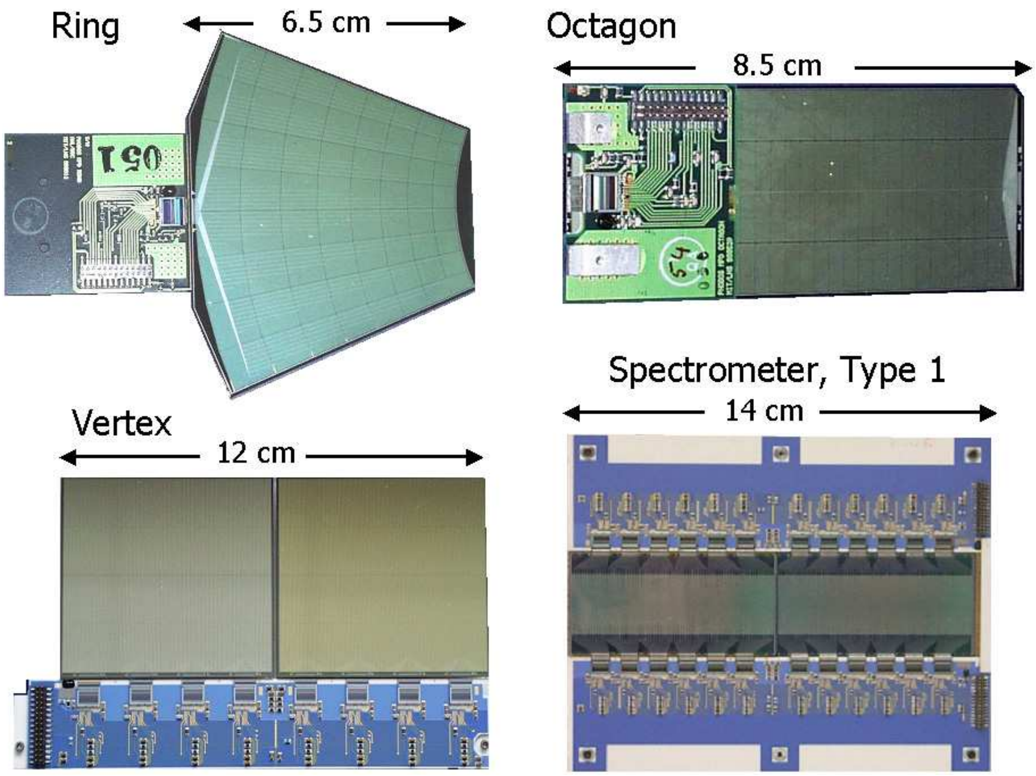

Figure 3.2: Photographs of four types of silicon sensor module.

gion that is free of charge carriers – the 'depletion zone'. Applying a reverse bias voltage to the silicon allows the charge carriers to drift further across the interface, which increases the size of the depletion zone. For the 300 μm thick silicon sensors used in PHOBOS, the whole volume was depleted with an applied voltage of approximately 70 V.

The passage of a charged particle through the silicon excites electrons into the conduction band, leaving behind a hole in the valence band. Because the energy gap is small compared to the typical energy deposited by an incident particle, many electron-hole pairs are created, resulting in a very good energy resolution. Under the influence of the applied voltage, and because the region is free of other charge carriers with which to recombine, the produced electrons and holes drift to opposite ends of the sensor.

Figure 3.1 shows a cross-section of the sensor design used in PHOBOS. The silicon sensors [83] were biased via polysilicon resistors (red), required to have at least 1 MΩ resistance. The p^+ implants were capacitively coupled to the aluminum pickup pads (green) via an 0.2 μm thick layer of silicon Oxide-Nitrous-Oxide (ONO) dielectric material (yellow). The induced current from each pad was read-out by its own metal line (blue) that led to the front-end electronics at the edge of the sensor. An advantage of the double metal-layer design was that the full surface of the detector could also be used for the routing of signals. The network of signal lines was separated from the aluminum pickups by a 1.2 μm thick ONO layer.

The read-out of the silicon channels was handled by commercially available chips

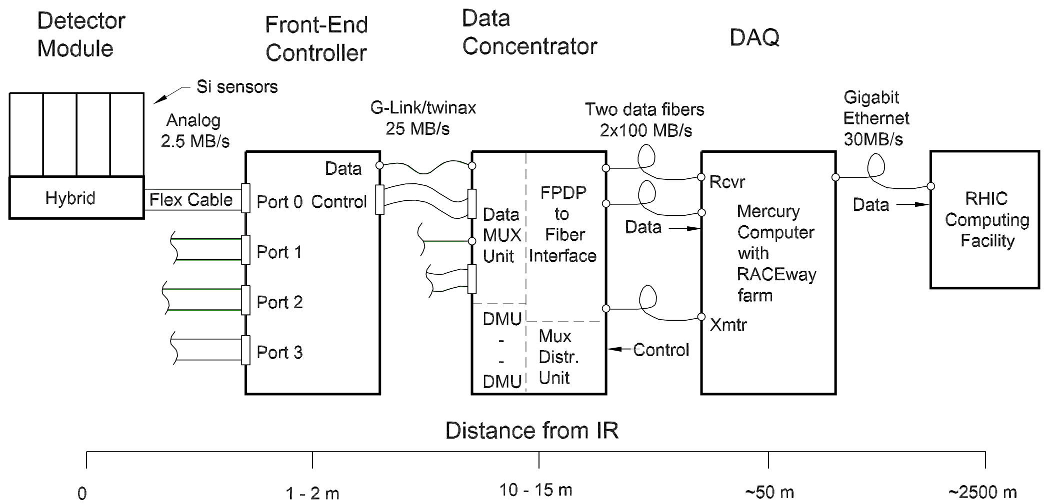

Figure 3.3: Diagram of the readout chain [85].

from the IDEAS company (http://www.ideas.no/), which integrated the collected signals from the silicon pads. Depending on the sensor pixelization, as many as sixteen, 64- or 128- channel VA-HDR-1 chips served a single module [84]. The detector modules consisted of one to four silicon sensors, and their associated read-out chips, mounted onto hybrids. Photographs of silicon sensor modules from four different PHOBOS subdetectors are shown in Fig. 3.2.

Front-End Controllers (FECs) resided in crates a few meters from the detector modules, which they controlled, powered, and read-out via flex cable. The pre-amplified signals from the read-out chips were digitized by 12-bit ADCs in the FECs. The digitized signals were sent via a G-link interface to the Data Multiplexing Unit (DMU) in the Data Concentrator, where they were collated and transmitted over two optical fibers to the DAQ (see Sect. 2.2.5). A summary of the read-out chain can be seen in Fig. 3.3 [85]. For further details of the PHOBOS detector read-out, see [84, 85].

3.2 Pedestal, Noise and Gain Calibrations

Besides the real signal of a particle hitting a pad, the digitized value in each detector channel, called the ADC signal, had three additional contributions that needed to be corrected for:

1. The constant offset in the ADC signal, called the ‘pedestal’, caused by a non-zero ‘leakage current’.

2. Electronic and thermal noise, which caused the offset ADC value to fluctuate randomly about its average.

3. Random event-by-event shifts in the offset for all channels on a single chip, called Common-Mode Noise (CMN).

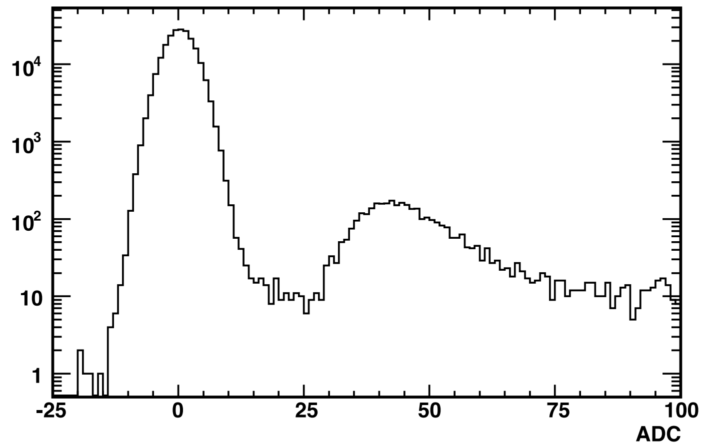

Figure 3.4: Pedestal-subtracted ADC signal distribution from a typical Ring sensor over many events. The width of the pedestal peak at zero corresponds to the noise. The peak at 40 ADC units corresponds to the 80 keV deposited by Minimum Ionizing Particles (MIPs).

For any given low-multiplicity event, most individual pads were not hit, due to low occupancy. Inspecting the signal in a given channel over many such events, the most common ADC value would indicate the location of the 'pedestal'. While the locations of the pedestals did change over time, they were relatively stable over an individual running of the detector. For this reason, at the beginning of each running, the algorithm described below was performed in each channel to find the pedestals.

First, the average signal from the first 200 events was calculated and called the 'pre-pedestal'. Then, in a window around the pre-pedestal location, the signals from the next 300 events were plotted and the peak location determined. If the peak-finding failed, more events were used until it was found. To determine the noise, the signals from the next 600 events were fitted with a Gaussian around the most probable value determined in the previous step. The extracted noise value corresponds to the width of the Gaussian at zero in Fig. 3.4[2].

In addition to the pedestal and noise contributions, all the channels on a given chip could experience random shifts in voltage. A CMN shift could be caused by a dip in the supplied voltage to a whole chip, in response to large current consumption in pads with large signals [84]. To correct for CMN, the pedestal-subtracted signals were collected for groups of channels event-by-event. Any non-zero offset in the single-event pedestal-subtracted signal distribution was attributed to CMN. By subtracting this component off of the raw ADC signal event-by-event, an improvement of about 20% was achieved in the noise level (see Fig. 3.5 [16]).

Finally, it was necessary to relate the ADC value in a channel to the actual deposited energy (e.g. in keV). To this end, the silicon sensors were equipped with a gain calibration system that was used in dedicated calibration runs. A sequence of known Digital-

[2]Note that the statistics that went into this plot are much greater than were used in the pedestal and noise determinations.

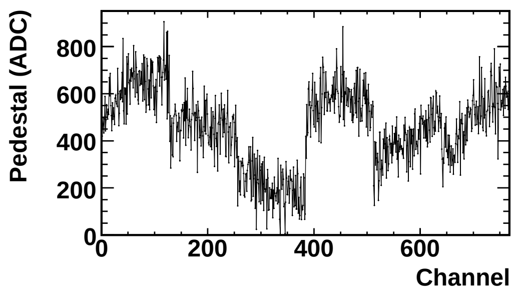

(a) Pedestal Values

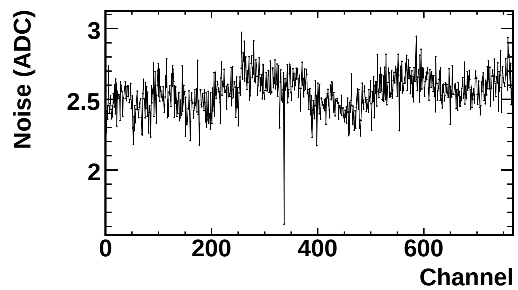

(b) Noise Values

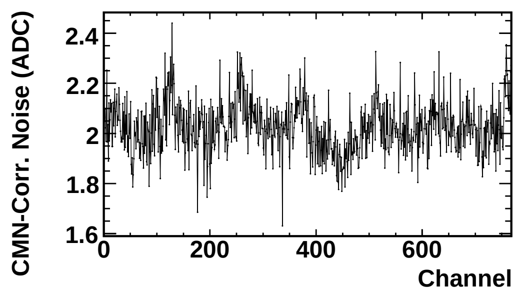

(c) Noise Values Corrected for CMN

Figure 3.5: The distribution of (a) pedestal values (b) noise values and (c) CMN-corrected noise values in ADC units for different channels. Notice the 128-channel structure of the individual chips [16].

to-Analog Converter (DAC) signals was inputted to the front-end pre-amplifiers. The signals were then digitized and the output ADC signals compared to the input. The gains (i.e. the slopes of the output-to-input ratios) were essentially constant over the dynamic range of the read-out chips. The deposited energy associated with one ADC unit was determined to be ~ 2.1 keV, corresponding to a most probable hit value of ~ 80 keV.

3.3 Dead and Hot Channels

Improperly functioning silicon channels needed to be identified and excluded from any physics analysis. The decision to declare a channel 'dead'[3] was based on three numbers: the noise, the number of hits, and the average energy per hit.

Noisy channels were excluded by imposing a cut at 10 keV on the maximum allowed noise. In the Rings, this value was later increased to 15 keV for the 2005 physics run.

For this study, a hit was counted when the energy exceeded four times the pedestal width (i.e. the noise). The number of hits above this threshold, and their associated analog energy, were summed over many events until each channel had been hit many times. Channels that had many fewer hits than the average were considered dead. Also,

[3]For these purposes, the term 'dead' encompasses actually dead channels as well as hot, noisy, and otherwise fishy channels.

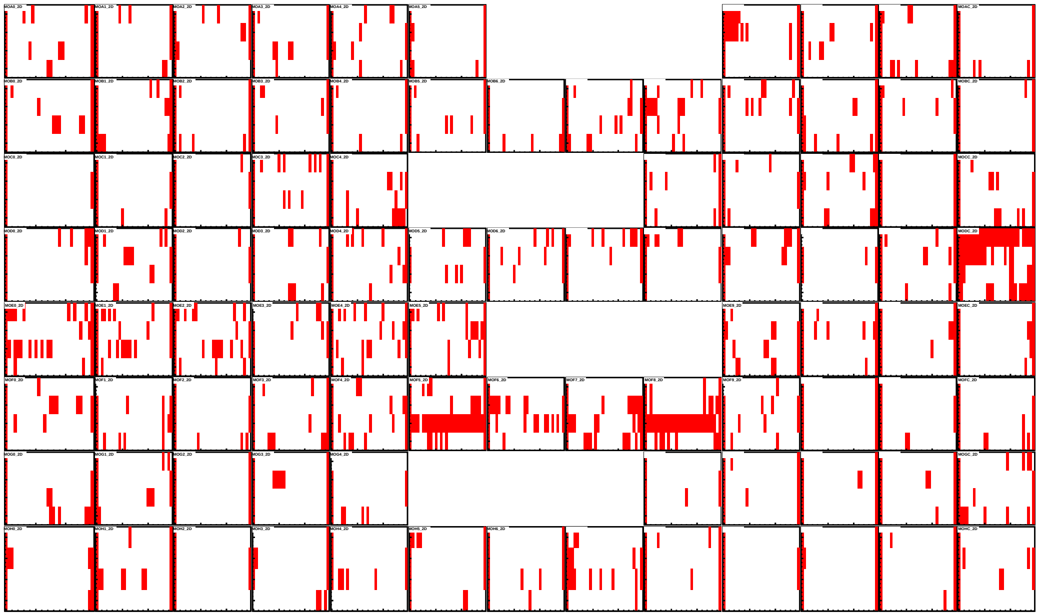

Figure 3.6: The distribution of dead channels in the Octagon detector for the 2004 PHOBOS physics run.

those with many more hits were rejected, since such channels might have large non-Gaussian tails in the noise. For channels with much more energy per hit or much less than average, something was wrong with the gains, so the channel was considered dead.

In the multiplicity detectors, the positions of the cuts on these two variables were determined for each sub-detector (e.g. second positive Ring). In the Spectrometer, however, the hit densities varied too much among the different layers to use the same cuts for the whole detector. Instead, the cuts were determined separately for each module. The percentage of dead channels in the multiplicity detectors and in each layer of the Spectrometer can be found in Table 3.1. For illustration, a map of the dead channels in the Octagon can be seen in Fig. 3.6. Whole rows of dead channels are likely a consequence of noisy readout chips.

Subdetector	Percent Dead
Octagon	8.43
Top Vertex	5.08
Bottom Vertex	6.05
Negative Rings	4.49
Positive Rings	6.70

Spectrometer	Percent Dead	
Layer	Negative Arm	Positive Arm
1	2.53	2.63
2	1.27	1.79
3	1.23	1.79
4	1.53	2.08
5	2.00	2.10
6	0.65	1.15
7	0.20	2.07
8	0.33	1.87
9	0.33	0.94
10	3.94	2.12
11	1.49	1.54
12	3.39	2.05
13	5.11	2.80
14	2.31	2.67
15	2.08	1.69
16	4.38	2.04

Table 3.1: Percentage of dead channels in (a) the multiplicity detectors and (b) each layer of the PHOBOS Spectrometer for both the positive and negative arms.

4 Event Characterization

Collision triggers used the time and energy information in the fast detectors to determine if a particular event was useful and should be recorded. Further selection on the utility of recorded events was performed offline. Once the signals in the various detectors had been read out and processed, the properties of collision events could be determined, in particular the collision geometry and vertex position.

4.1 Collision Trigger

Triggering, the determination of whether a collision has occurred and whether its signal should be recorded, was one of the most important aspects of running the PHOBOS experiment. In principle, one could have just used the crossing-clock provided by RHIC to alert when the bunches in the beam should be colliding. However, this would have resulted in most of the data coming from undesirable beam-gas events, collisions between ions in the beam and gas in the beam-pipe. To determine when real nucleus-nucleus collisions had occurred, several types of triggers were employed, including Minimum Bias (MinBias) triggers and Vertex triggers. Additionally, during the d+Au run, triggering with the SpecTrig was employed to enhance high-p_T tracks. A detailed discussion of this trigger configuration can be found in [76].

MinBias triggers were designed to capture a large fraction of the total cross-section with minimal losses in efficiency in peripheral events. In lower multiplicity collision systems (e.g. p+p), the trigger condition was at least one hit slat in each of the positive and negative Paddles. For higher multiplicity systems (e.g. Au+Au), more than two hit slats were required in each Paddle.

Vertex triggers were employed to confine the recorded events to those lying within the useable region of detector. The time signals from the two T0s were sent to a Time-to-Analog Converter (TAC), which calculated their time difference. An adjustable window was used to select only events with a T0 time difference corresponding to the desired vertex range[1].

During the Au+Au and Cu+Cu runs in 2004 and 2005, a combination of high luminosity and lost beam particles grazing the beam pipe resulted in a cloud of desorbed electrons forming in the beam [86]. The prevalence of double $Au^+ + e^-$ events that appeared to come from the desired vertex range swamped the existing trigger. This phenomenon

[1] For the 2004 run, the vertex window was extended somewhat beyond the usual analysis range to $-40 < v_z < 20$ cm. It was thought that the very negative vertex positions might be useful to certain analyses (e.g. reconstruction of the ϕ meson via the two kaon decay channel).

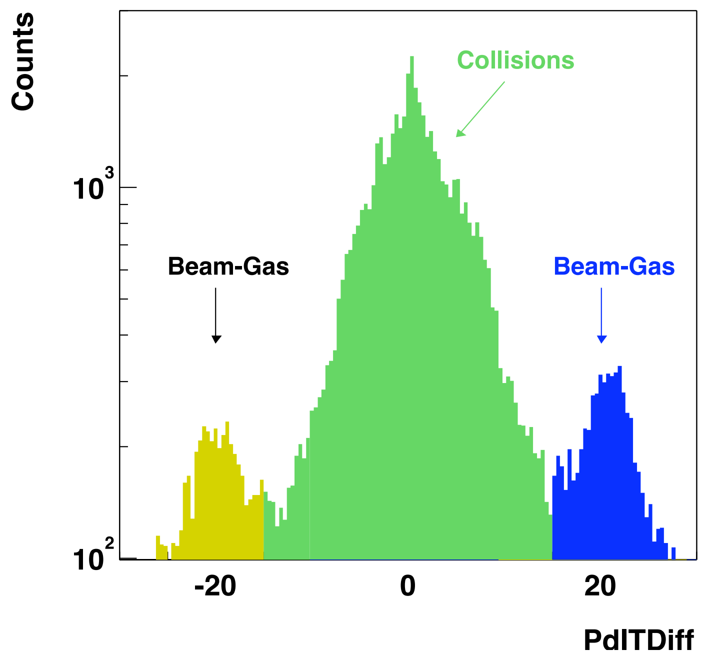

Figure 4.1: The distribution of Paddle Time Difference (PdlTDiff) shows a peak near zero, corresponding to collisions, as well as two peaks from beam-gas events at ±21 ns [87].

varied in magnitude from run to run, so the decision was made to use a trigger that incorporated the ZDC information when there were high backgrounds. Requiring energy deposited in both ZDCs ensured that a heavy ion from each beam had participated in the collision. Nonetheless, the high backgrounds meant that a larger fraction of events had to be discarded later in event selection due to pile-up (more than one collision in the detector at the same time).

4.2 Event Selection

The offline selection of collision events for analysis relied largely on rejecting beam-gas events with cuts on the PdlTDiff and the ZDC timing. As seen in Fig. 4.1 [87], beam-gas events from the region outside the two Paddles left a characteristic time difference of ±21 ns, corresponding to the time it took a relativistic particle to travel the 6.4 m between the two Paddles. A hard cut on PdlTDiff was placed at ±4 ns to select collision events. Because the signals in the ZDCs came from spectator neutrons liberated in the collision of a nucleus, the energy and timing signals looked quite different for beam-gas and collision events. Requiring a valid ZDC time excluded beam-gas events from between the Paddles that were not rejected by the PdlTDiff cuts. Finally, recognizing that very central collisions, with few spectators, left little signal in the ZDCs, events were allowed to fail the ZDC timing cut if there were large signals in both Paddles. The offline event selection criteria were contained in a single flag, called Is Collision (IsCol), for use in physics analysis. Further details and the specifics of event selection in the Cu+Cu spectra analysis are in Sect. 6.1.

4.3 Centrality Determination

Heavy-ion collision events come in all varieties; sometimes the nuclei collide head-on, while other times the collisions are more glancing. To study the underlying physics behind any measurement, it is essential that one can classify events based on the initial impact parameter of the two nuclei.

For all the different collision systems and energies measured by PHOBOS, the centrality classification procedure followed the same three basic steps. First, the 'trigger efficiency' (the fraction of the total cross-section to which the trigger is sensitive) was estimated by comparing measured distributions in data and Monte Carlo (MC). Next, using the known efficiency and a multiplicity variable with a monotonic dependence on centrality, the data were divided into bins of fractional cross-section. Finally, using MC simulations, the bins in fractional cross-section were related to the relevant variables of the collision geometry (e.g. impact parameter, average numbers of participants and collisions). These procedures and the various cross-checks on their validity are discussed in [87].

4.3.1 Calculating the Efficiency

To estimate the missing cross-section, the number of hit Paddle slats (between 0 and 32) was compared between data and HIJING as seen in Fig. 4.2. There is a relatively flat region between 15 and 22 hit Paddles, over which the different distributions were normalized. The final efficiency was then calculated as the ratio of events seen in data by the sum of data events with sixteen or more hit Paddles and MC events with fifteen or fewer hit Paddles.

$$\frac{\text{Data}(0,32)}{\text{MC}(0,15)+\text{Data}(16,32)} \tag{4.1}$$

The data were only corrected in the inefficient region. This ensured that any discrepancy in the most central collisions, that might be sensitive to the particular parameters of the HIJING MC, would not be included. The final efficiencies for the 200 GeV Au+Au data were 97% (n>0) and 88% (n>2). At 62.4 GeV, the same quantities were 91% and 81%.

The situation was slightly less certain for Cu+Cu collisions where the flat region in the hit Paddle distribution was neither as broad nor as flat. A 'shape matching' method was also tried in which the distributions in a given centrality variable were normalized such that the shapes matched between data and MC at high multiplicity. The efficiency was then just the ratio of the two integrals. This technique had previously been used in the low energy Au+Au run as well as the d+Au run. In the end, the Cu+Cu efficiencies

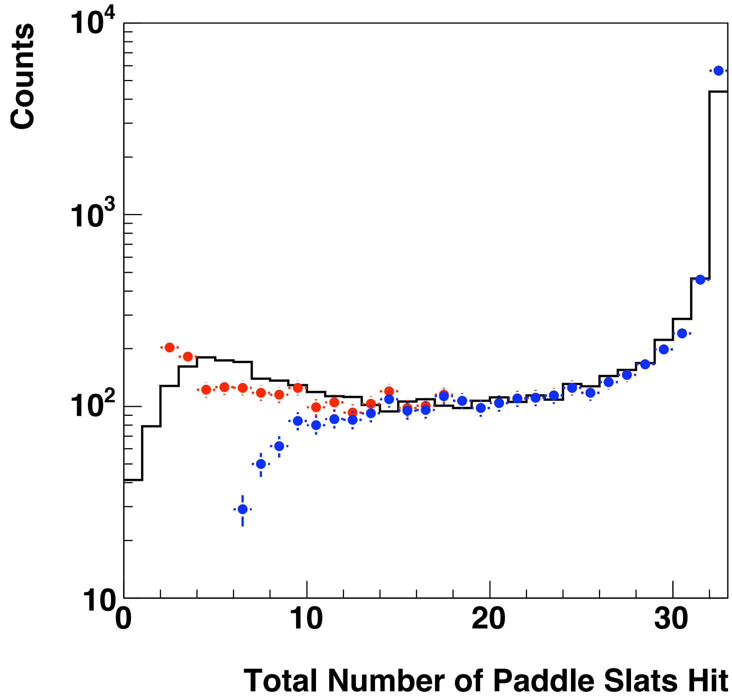

Figure 4.2: The distribution of the number of hit Paddles for HIJING (black line) and Au+Au data for the n>0 (red points) and n>2 (blue points) MinBias trigger requirements.

were taken as the average of many different measurements. The final values for the n>2 sample were 84 ± 5 and 75 ± 5 for 200 and 62.4 GeV, respectively.

4.3.2 Making Cuts on Fractional Cross-section

Once the efficiencies had been determined, it was possible to define cuts that divided data events into bins of fractional cross-section. The multiplicity variable on which the cuts were made was only required to have a monotonic dependence on centrality. As such, many different variables were used over the PHOBOS lifetime depending on the collision system. These included the truncated mean of the energy in the Paddles (Paddle Mean (PdlMean)), the sum of the energy in the ZDCs (ZDCSum), the total energy in the symmetric regions of the Octagon (EOct), and the energy in all six Rings (ERing).

Figure 4.3(a) shows the clear monotonic relationship between PdlMean from a MC simulation and the number of participating nucleons (N_{part}) from a Glauber model. Using the previously calculated efficiency, cuts were made on the PdlMean distribution corresponding to bins of cross-section. For example, the most central bin shown in Fig. 4.3(b) corresponds to the 3% most central collisions.

For the analysis of the Cu+Cu spectra in Ch. 6, cuts made on the EOct variable were used to determine centrality. It was considered that a bias might be introduced by measuring the event centrality and the spectra in the same region of pseudorapidity. How-

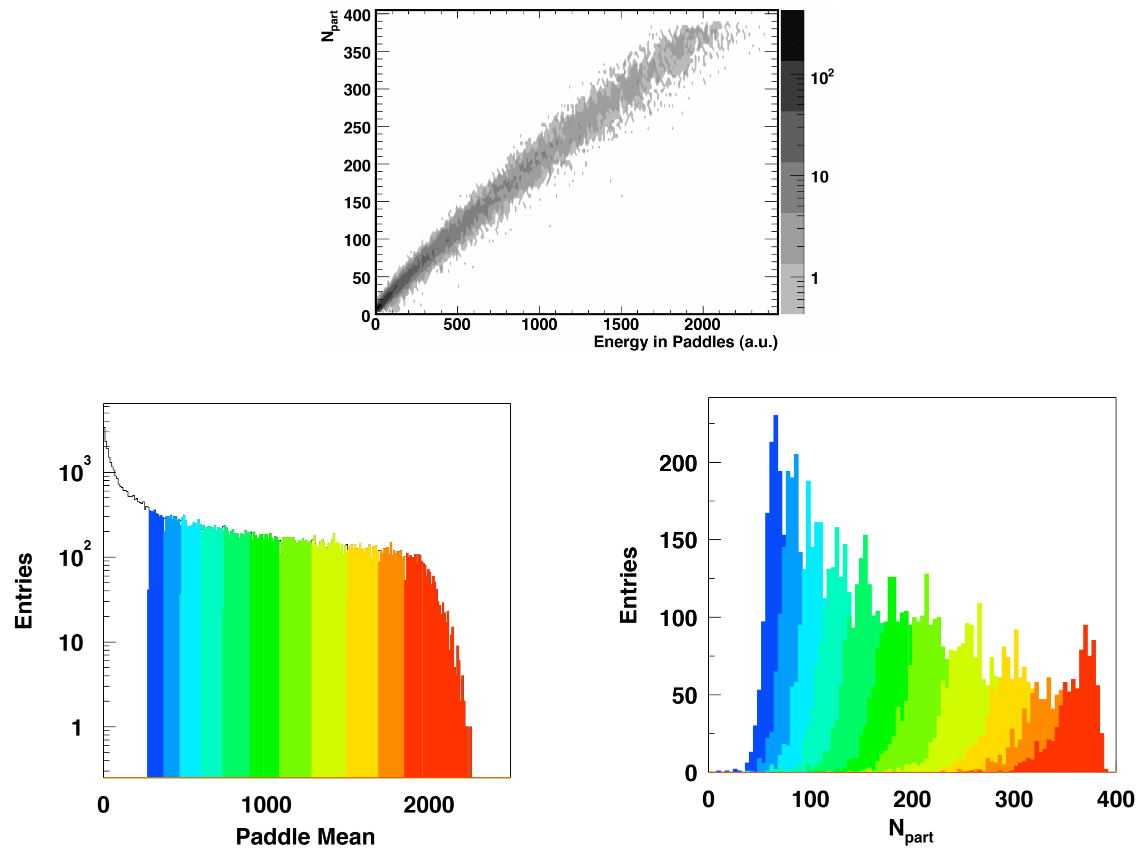

Figure 4.3: (a) The relationship from a MC simulation between truncated mean signal in the Paddles and number of participating nucleons. (b) The positions of the fractional cross-section cuts on the PdlMean distribution. (c) Distribution of N_{part} in MC for the same bins shown in (b).

ever, it was found that this only affected the very most central bin, and even there only slightly.

4.3.3 Estimating Centrality Variables

The final step in the centrality procedure was to relate the multiplicity signal in the data to the number of participating nucleons in the collision. As was already seen in Fig. 4.2, the shapes of the Paddle signal distributions were well-matched between data and HIJING. Because the full cross-section was present in the MC, it could simply be divided into bins; the data were first scaled by the efficiency before binning. The centrality information was accessible for every MC event, so the N_{part} distributions could be calculated for each cross-section bin (see Fig. 4.3(c)).

The average value of N_{coll} in a given cross-section bin was not directly taken from the HIJING. Rather, the relationship between N_{part} and N_{coll} was estimated using a Glauber model of nucleus-nucleus collisions (see Fig. 4.4(c)). In this model, each nucleus con-

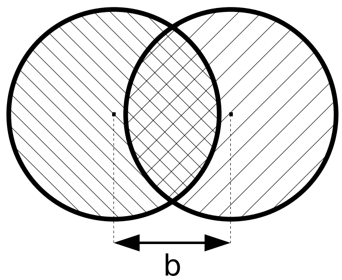

(a) View down the beam

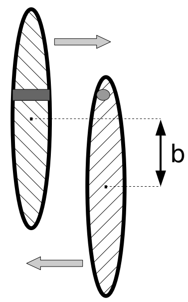

(b) Side view

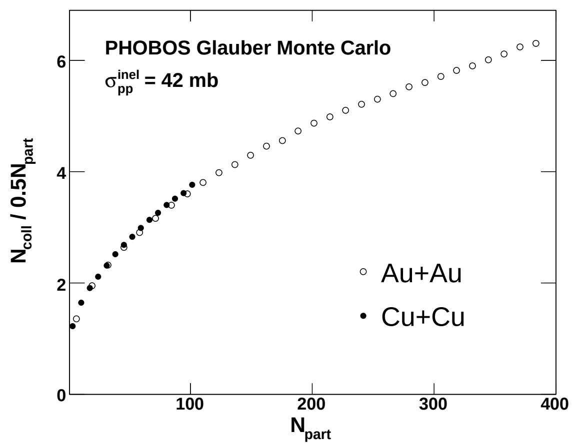

(c) N_{coll} and N_{part} from Glauber Model

Figure 4.4: Illustration of collision event geometry. (a) The view along the beam of two nuclei collide with impact parameter b. The shaded region represents the participating nucleons N_{part}. (b) The same colliding nuclei seen from the side. A single nucleon (small circle) undergoes multiple collisions, determined by the thickness of the other nucleus (gray box). (c) The total number of binary collisions N_{coll} per participating nucleon pair.

sisted of nucleons randomly arranged according to a 'Woods-Saxon' probability distribution

$$\rho(r) = \frac{\rho_0}{1 + exp\left(\frac{r-R}{d}\right)} \tag{4.2}$$

where $\rho(r)$ is the normalized nuclear density, R = 6.38 fm is the nuclear radius, and $d =$ 0.535 fm is the surface thickness. The nucleons were assumed to travel in straight lines, with a chance of interaction given by the total inelastic p+p cross-section (42 ± 1 mb at 200 GeV and 36 ± 1 mb at 62.4 GeV). As shown in Fig. 4.4(b), each nucleon was allowed to undergo any number of collisions without deflection.

For Cu+Cu and Au+Au collisions at $\sqrt{s_{\mathrm{NN}}} = 62.4$ and 200 GeV, tables containing the estimated N_{part} and N_{coll} values for each centrality bin, and the respective PdlMean or

EOct cuts, can be found in Appendix C.

4.4 Vertex Reconstruction

Determination of the collision vertex was a critical first step for the interpretation of the signals in the detector. For instance, it was used as a starting point for the reconstruction of track candidates (see Sect. 5.2). Numerous different algorithms were used to find the event vertex, utilizing the various sub-detectors. Different sub-detectors had their own advantages when it came to vertex reconstruction. Using the time difference between the two Paddles, for example, provided a rather poor resolution of 15 cm, but it had a large vertex range and high efficiencies even down to very low multiplicity events.

4.4.1 Au+Au Vertex Finding

In Au+Au events, the vertex was determined by a combination of different algorithms. The variously reconstructed vertices were checked for consistency and the most accurate vertex position determined in all three spatial coördinates. To decide how to weight the different vertices based on their accuracy, reconstructed vertex positions were compared to the true position in MC events. A detailed description of the vertex-finding procedure can be found in [88]. For the analyses presented in this thesis, the z-vertex range was restricted to within -15 to 10 cm. In this range, the composite vertex position, known as RMSSelVertex, was selected from a combination of the three algorithms described below, taking into account their known resolutions in each dimension.

Using the Vertex Detector: ZVertex

As expected from its name, the Vertex detector provided the most accurate determination of the collision vertex in the y and z coördinates. The algorithm began by clustering pads with deposited energy above a minimum threshold as described in Sect. 5.1.1. Then, straight lines joining combinations of hits in the Inner and Outer layers were projected back onto the $y = 0$ plane where the z positions were computed. The peak in the z distribution of these line segments corresponded to the vertex position. The quality of the reconstruction could be estimated by comparing the results of this algorithm performed separately for the upper and lower pairs of Vertex layers.

Projecting the lines from hit pairs instead to the $x = 0$ plane gave an estimate of the y-vertex position, albeit with somewhat worse resolution. The x position could also be determined, though due to the much larger pad sizes in this dimension (see Sect. 2.2.1), it was considerably less precise as shown in Table 4.1. To accurately determine the x-vertex position, information from the Spectrometer was required. Two different algorithms were developed, using straight track segments in the first few silicon layers. While using the Spectrometer allowed the determination of the vertex in three dimensions, these algorithms suffered particularly for low multiplicities due to the very small phase-space coverage.

Vertex Algorithm	X-resolution (μm)	Y-resolution (μm)	Z-resolution (μm)
SpecVertex SpecPN	219 ± 3	297 ± 3	271 ± 4
SpecMainVertex	585 ± 7	385 ± 5	593 ± 10
ZVertex	2424 ± 32	163 ± 1	85 ± 1
RMSSelVertex	238 ± 4	182 ± 2	81 ± 1

Table 4.1: The vertex resolution for the different reconstruction algorithms in the three spatial coördinates. The resolutions were obtained for MC simulations of central Au+Au events [88].

Track Intercept Algorithm: SpecMainVertex

This method used the intersection points of pairs of straight tracks to determine the vertex position. First, straight tracks in the first four layers of the Spectrometer were constructed using the road-following technique described in Sect. 5.2.1, but without the vertex constraint. All tracks with χ^2 greater than 1% based on a straight-line fit were made into pairs. Pairs of tracks with a Distance of Closest Approach (DCA) less than 0.4 cm were retained; the vertex position for such pairs was considered to be the midpoint at their nearest approach. Each coördinate of the vertex position was separately averaged from the retained pairs. The quality of the vertex determination was calculated by comparing the DCA of the straight tracks to the average vertex position.

3-D Fit Algorithm: SpecVertex SpecPN

The SpecVertex procedure also used straight tracks, though in this case the road-following was continued out to the fifth and sixth layers. The vertex position was determined in three-dimensions by a MINUIT minimization of the DCA summed over all selected straight tracks. This routine was somewhat more computationally intensive than the others, but when a vertex was properly reconstructed, it was the most precise in three dimensions (see Table 4.1).

4.4.2 Cu+Cu Vertex Finding

One of the main goals of the Cu+Cu run was to compare experimental observables to Au+Au collisions for similar collision geometry (i.e. fractional cross-section). However, even very central Cu+Cu only had multiplicities comparable to semi-peripheral Au+Au [89]. Clearly, a more efficient vertexing method was required to analyze peripheral Cu+Cu collisions. The Octagon Probability Multiplicity (OctProbMult) algorithm was developed using hits in the single-layer Octagon detector to determine the vertex position.

Using the Octagon: OctProbMultVertex

Because the emission angle of a track determined the number of pads it would traverse, some information about the vertex could be determined from the number of adjacent

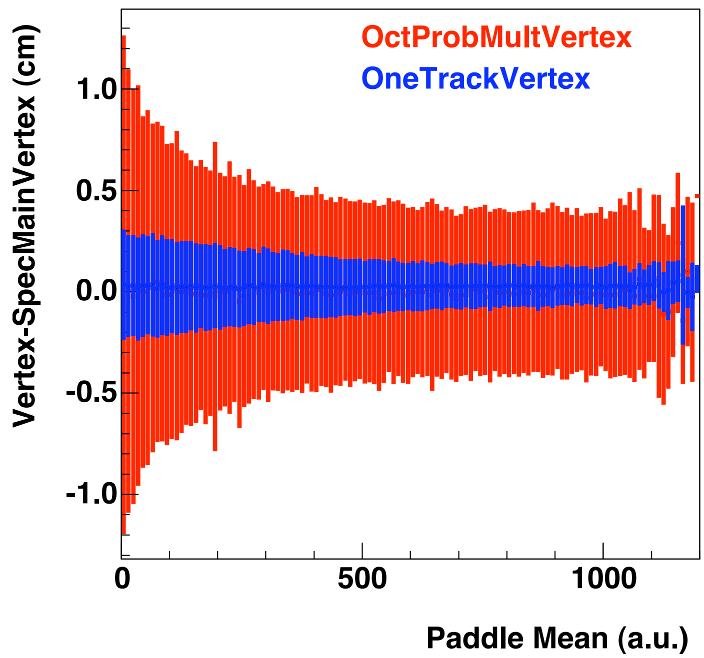

Figure 4.5: The z-vertex resolution in the region $-10 < v_z < 10$ cm for the two methods introduced for the Cu+Cu run, OctProbMultVertex and OneTrackVertex. The resolutions are presented as a function of PdlMean, corresponding to the range of collision centralities in Cu+Cu collisions [87].

pads with hit energy and their z-position. First, clusters were defined to be adjacent pads in a single row with hit energies each above 0.4 MIP and together above 0.6 MIP. For each cluster, the position and number of merged pads were used to construct the probability distribution of z-vertex position. Then, the triangular probability distributions for each cluster were summed together and a region selected where the probability distribution exceeded a set percentage of the maximum (by default the value was 60%). The final vertex position was then determined from one of three possible criteria: 1) the maximum value in this region, 2) the probability weighted mean over the region, or 3) the center of the region. During the 2005 Cu+Cu run, the first method was used.

Whereas the OctProbMultVertex algorithm was efficient down to very low multiplicities, it did not provide a particularly good vertex resolution (see Fig. 4.5). Since a precise initial vertex position was needed by the tracking procedure, another algorithm was developed by Richard Hollis [87] for this purpose, called OneTrackVertex.

Using Individual Tracklets: OneTrackVertex

The OneTrackVertex was so-named because it only required a single track to determine the event vertex. First, 'tracklets' were generated from all pairs of hits in the two vertex layers. Next, the straight tracks were traced backwards and a DCA cut applied on their nearest approach to the beam axis. While only one candidate track was required, if there were many, the average position of candidates within 1 cm of the most frequent vertex was used.

The same procedure was also repeated in the Spectrometer. The best vertex was selected by comparing the values determined in the Vertex and the Spectrometer to a third vertex, for example the OctProbMultVertex described in the previous section. If either of the two OneTrackVertex values agreed with the comparison vertex, or if the two values agreed with each other, the vertex finding was considered successful. The improvement in vertex resolution can be seen in Fig. 4.5. Only a 3% drop in efficiency was observed compared to OctProbMultVertex [87]; this allowed measurements in 200 GeV Cu+Cu collisions with as few as 20 participant nucleons. In the most central Cu+Cu events, fewer than 1% of tracks were lost due to the combined effects of vertex resolution and inefficiency compared to using RMSSelVertex. This was considered an acceptable loss and was accounted for by the MC-based acceptance and efficiency correction, described in Sect. 6.3.1.

5 Particle Reconstruction

The trajectories of particles produced in collision events were characterized by the spatial position of the 'hits' they left in the detector. Merged hits were formed from the calibrated signals in the silicon pads using clustering algorithms. In the Spectrometer, merged hits from different layers were combined to form 'tracks' with reconstructed momenta based on the curvature in the magnetic field region.

5.1 Hit Selection

Particles would often pass through more than one silicon pad, especially where the angle of incidence between the sensor and the trajectory was small. To account for this effect, the deposited energies in adjacent pads were combined based on the selection criteria described in the Sect. 5.1.1.

In the Octagon detector, additional cuts were applied based on the deposited energy, to reduce contamination from secondary particles. For the correlations analysis described in Ch. 8, hits in the first layer of the Vertex detector were projected onto the plane of the Octagon to 'fill' the holes in that detector. Because of the large number of tracks in a Au+Au event and the relatively large pad sizes in the Octagon, each hit was also weighted for occupancy (i.e. more than one particle hitting the same pad) based on the local density of hit pads.

5.1.1 Merging of Hit Pads

Before hit merging was run in the multiplicity detectors (i.e. Octagon and Vertex), channels identified as dead by the procedure in Sect. 3.3 were masked. The basic strategy of the merging algorithm had three steps. First, pads with energy above a noise threshold were selected as seeds. Next, the energy of adjacent pads was merged into candidate hits if the energy passed the merging threshold. Finally, hit candidates were required to have a total merged energy above a hit threshold. These thresholds for the various sub-detectors are listed in Table 5.1. Merging was only performed among neighboring columns not neighboring rows (i.e. in the direction of finer segmentation in the Vertex and Spectrometer detectors).

Octagon Hit Merging

Because the geometry of the Octagon was such that a track could traverse no more than three adjacent pads for events in the nominal vertex range ($-10 < v_z < 10$ cm), this was

	Octagon	Vertex	Spectrometer
Noise Threshold	19.2 keV	0.3 MIP	0.15 MIP
Merge Threshold	$< 65 - 90$ keV	> 0.3 MIP	> 0.15 MIP
Hit Threshold	30 keV	0.7 MIP	0.5 MIP
Maximum Pads to Merge	3	2 – 3	8

Table 5.1: A summary of the thresholds used in the merging algorithms for the different sub-detectors. One MIP corresponds to 80 keV for a 300 μm thick silicon pad.

the maximum number of pads that were merged together. The merging algorithm began by moving outward from the vertex along each row of the Octagon looking for hits that exceeded the 19.2 keV noise cut. When such a hit was found, the angle-corrected energy in each of the neighboring columns was calculated. If the angle-corrected energy in a neighboring pad was below the merging threshold, its energy was added to the candidate hit. The merging threshold was the following function of pseudorapidity: $65.0\ \text{keV} + 8.75\ \text{keV} * \left|\eta\right|$. The candidate was considered a proper hit if its angle-corrected, merged energy exceeded the 30 keV hit threshold (see Fig. 5.1). For pads at $\left|\eta\right| < 0.5$, the merging of neighboring columns was skipped. This was due to high occupancy and relatively perpendicular trajectories relative to the pads. Finally, if the track geometry was such that a track must have traversed more than one pad and yet no shared hits were found, the candidate was rejected.

Vertex Hit Merging

Vertex hits were merged in a similar fashion. Moving along each row, candidate hits were required to have an angle-corrected energy of at least 0.3 MIP, where one MIP corresponds to 80 keV. The hit in the next column was merged to the candidate if it also passed the 0.3 MIP cut on its angle-corrected energy; otherwise, a new hit candidate search began. Only two adjacent pads (or three in the region $\left|\eta\right| > 0.5$) were allowed to be merged. The final candidate was required to have an angle-corrected energy greater than 0.7 MIP to count as a hit. The position of the merged Vertex hit was the energy-weighted mean of the merged pads.

Spectrometer Hit Merging

The merging procedure in the Spectrometer was exactly the same as for the Vertex detector, except for different threshold values. The threshold to be added to a hit candidate was 0.15 MIP and the threshold for final merged hits was 0.5 MIP. Because of the fine resolution in the horizontal direction and the bending power of the magnet, curved tracks could traverse the silicon at quite shallow angles. Thus, the maximum number of adjacent pads that could be merged was increased to eight. Finally, it should be noted that the horizontal pad number of the merged hit was the energy-weighted average of the merged pads rounded to the nearest integer. This was important for the exclusion of hits belonging to the trigger track discussed in Sect. 8.1.

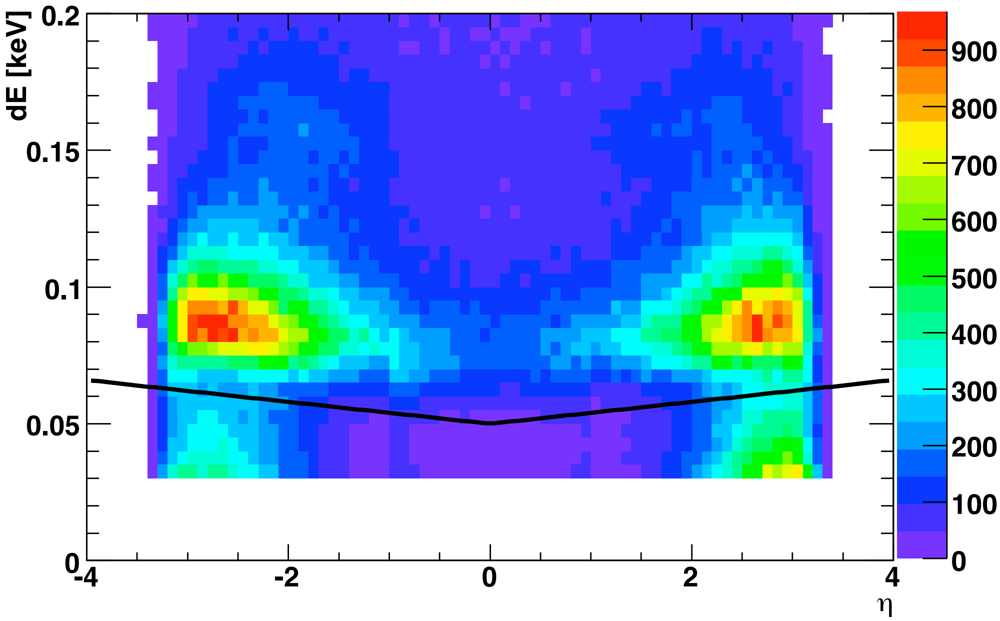

Figure 5.1: The distribution of Octagon hits as a function of pseudorapidity and angle-corrected hit energy. The black line corresponds to the applied cut of $50.0\,\text{keV} + 4.0\,\text{keV} * |\eta|$. The cutoff at 30 keV comes from the hit merging. Note the MIP peak around 80 keV and the concentrations of secondaries at large pseudorapidity and small angle-corrected energy. Faint, two-MIP peaks can be seen at 160 keV with a maximum shifted to mid-rapidity where the occupancy was higher. The paucity of hits at mid-rapidity is due to the Octagon holes.

5.1.2 Secondary Rejection

The deposited energy information was used to exclude many of the hits generated by secondary particles. Figure 5.1 shows the distribution of angle-corrected hit energy for hits in the Octagon as a function of pseudorapidity. The angle correction of hit energies assumed that all hits originated from the event vertex. At large pseudorapidity, primary tracks traverse the Octagon at a shallow angle, depositing significantly more energy than secondaries not coming from the event vertex. Such secondaries are responsible for the concentrations of hits in Fig. 5.1 at large pseudorapidity and small energies – well below the prominent MIP peaks around 80 keV. To exclude these secondaries, a 'v-shaped' pseudorapidity-dependent hit energy cut was applied at $50.0\,\text{keV} + 4.0\,\text{keV} * |\eta|$.

5.1.3 Filling Octagon Holes with Vertex Hits

The Octagon detector had three sensors missing from both its top and bottom faces to allow particles to reach the Vertex detector unimpeded. The Inner Vertex layers covered nearly the same phase space as the Octagon holes. To avoid counting hits twice in the slight overlap between detectors and to provide a more uniform hit density, hits in the Inner Vertex sensors were projected onto virtual sensors with the dimensions and granularity of the adjacent Octagon sensors as in [90]. In practice a projection map was constructed for every 1 mm in z-vertex position, describing the mapping between Vertex and Octagon columns. If the azimuthal angle ϕ of a Vertex hit fell into the acceptance of the Octagon, this hit was ignored as it would already have been counted. Because the Vertex was much more finely pixelized than the Octagon, it was possible that more than one hit would be projected onto a virtual pad. In this case, the energies were added and the spatial coördinates averaged to make a single Octagon hit. Unlike in [90], no attempt was made to insert random hits into the remaining gaps in the acceptance, a procedure that would no doubt have been problematic for a correlations measurement.

5.1.4 Occupancy Weighting

In the mid-rapidity Octagon, uncorrected correlations were very strongly affected by occupancy. At first thought one might think that occupancy should affect signal and mixed events by the same amount. However, in any given event, regions near the reaction plane had higher multiplicity, resulting in greater losses due to occupancy. Conversely out-of-plane regions had lower multiplicity, resulting in slightly less than average occupancy losses. It is clear that this would result in the diminution of the observed magnitude of flow.

To counteract the destructive influence of occupancy on correlations, the local multiplicity had to be determined event-by-event and the hits weighted accordingly. This was tried two different ways: a semi-analog method adapted from the analysis of forward-backward multiplicity correlations [91] and a digital method used in the flow analyses [90]. The semi-analog method, which determined the occupancy weight based on the hit energy and the average energy per hit, was ill-suited to the requirements of the correlations analysis presented in Ch. 8. In particular, it failed in the transition from the Octagon to the Vertex acceptance. On the other hand, the digital correction worked quite well in preserving the input correlations as can be seen in Fig. 8.2.

The digital correction was based on the number of occupied pads in the vicinity of a given hit. In a region of $\pm$ 10 columns and $\pm$ 2 rows centered on a given pad, the total number of live pads (n_{pads}) and the number of hit pads (n_{hit}) were counted. The number of pads without a hit was then $n_0 = n_{pads} - n_{hit}$. Assuming Poisson statistics, the probability that any pad is hit n times is:

$$P(n) = \frac{\mu^n e^{-\mu}}{n!} \tag{5.1}$$

where μ is the mean of the Poisson distribution. The probability that a pad is not hit at all can be written from Eq. 5.1 as follows:

$$\frac{n_0}{n_{pads}} = P(0) = e^{-\mu} \tag{5.2}$$

Thus the average number of times a pad is hit is:

$$\mu = \ln\left(\frac{n_{pads}}{n_0}\right) \tag{5.3}$$

The occupancy weight w that one should apply to a given hit corresponds to the average number of times hit pads are hit.

$$\begin{aligned} w &= \sum_{n=1}^{\infty} \frac{nP(n)}{1-P(0)} && (5.4) \\ &= \frac{1}{1-P(0)} \sum_{n=0}^{\infty} nP(n) && (5.5) \end{aligned}$$

Since the term in the sum is just the definition of μ, it follows that the occupancy weight is related to the fraction of hit pads as follows:

$$w = \frac{\mu}{1-e^{-\mu}} = \mu \cdot \frac{n_{pads}}{n_{hit}} \tag{5.6}$$

5.2 Track Finding

The procedure for finding tracks in PHOBOS consisted of two parts: a straight-line road following algorithm in the first six layers, and a curved tracking algorithm based on Hough transformations in the magnetic field region. After matching the straight and curved segments, a momentum fit determined the best trajectory considering the full covariances between residuals in hit position.

5.2.1 Straight Track Finding

Due to the very low magnetic field in the region of the first six Spectrometer planes (see Fig. 2.4(b) on page 30), the tracks in this region were fit with straight lines. The straight line tracking used in Au+Au and Cu+Cu events relied upon the previous determination of the event vertex from the RMSSelVertex and OneTrackVertex algorithms, respectively (see Sect. 4.4). The angles ϕ and θ were calculated relative to the event vertex for each hit in the first two Spectrometer layers. For every combination of a hit in the first layer with a hit in the second layer, the relative angles $d\phi$ and $d\theta$ were compared to maximum allowed values $d\phi^{max}$ and $d\theta^{max}$. Those pairs that passed the cuts were kept as seeds to be extended through the next four layers.

Starting with these seeds the same procedure was performed for each subsequent layer with the last hit on the candidate track being compared to all the hits in the new layer. The values of the cuts, $d\phi^{max}$ and $d\theta^{max}$, were separately defined for each layer (see Table 5.2). If more than one hit in a new layer could be combined with a candidate track, the track was replicated and a copy with each possible hit propagated to the next

Layer	1	2	3	4	5
$d\phi^{max}$	0.025	0.025	0.025	0.045	0.065
$d\theta^{max}$	0.012	0.010	0.008	0.007	0.004

Table 5.2: Maximum allowed angular differences for the addition of a hit to an existing straight track candidate. The layer numbers refer to the first of the consecutive layers compared.

layer. While hits were required in the first two layers, one layer could be missed in the next four layers.

After each new layer, the track candidates were fit with straight lines in the XZ and the YZ planes. The fit in the XZ plane included all layers, but the fit in the YZ plane never used the last two layers due to the increased vertical pad size (see Table 2.1). The χ^2 was constructed from the displacements of the hits from the straight line using the pad dimensions as weights. Because multiple scattering effects were not included in the χ^2 determination, a relatively loose cut on fit probability was applied ($prob > 0.0005$). When this procedure had been completed for all six layers, a final selection was made on tracks that shared hits; only the track with the best fit probability was retained.

5.2.2 Curved Track Finding

The direction and magnitude of the bending in the magnetic field determined particle momentum and charge sign. Since the field in the outer region of the Spectrometer was not uniform, particles did not follow simple, circular trajectories through the detector. This fact motivated the use of look-up tables to extract the momentum and polar angle (p, θ) of tracks via a 'Hough transformation' [92] from the location of two hits relative to the event vertex.

These so-called 'Hough tables' were generated by simulating single pions in one Spectrometer arm and measuring the two angles described in Fig. 5.2, α and γ, for different simulated values of inverse momentum $1/p$ and polar angle θ[1]. The $1/p$ and θ values were stored for twenty α-bins and twenty γ-bins for each combination of layers in both the central and outer wing regions of the Spectrometer (see Table 5.3). The tables were generated separately for the two bending directions and in 0.5 cm bins of z-vertex from $-15 < v_z < 10$ cm.

The first step in building a curved track was to construct all possible 'Hough sticks', pairs of hits from the adjacent layers described in Table 5.3. To interpolate the track parameters of these sticks from the discretely binned Hough tables, polynomial fits were used to extrapolate between the centers of the bins in α and γ [16]. Once all the Hough sticks had been created and their associated track parameters determined, the process of assembling sticks into 'Hough chains' could begin. Starting with layer 9 and working outwards one layer at a time, all sticks that shared a hit were considered for chain-building. Sticks belonging to a single track should have the same momentum param-

[1] The inverse momentum, related to the bending radius, is the relevant variable in tracking.

Stick	Center	Outer Wing
A	9 - 10	9 - 10
B	10 - 11	10 - 11
C	11 - 13	11 - 13
D	13 - 14	13 - 15
E	14 - 15	15 - 16

Table 5.3: Layers used to form Hough sticks in the central and outer wing regions of the Spectrometer (see Fig. 5.2 for the layer pattern).

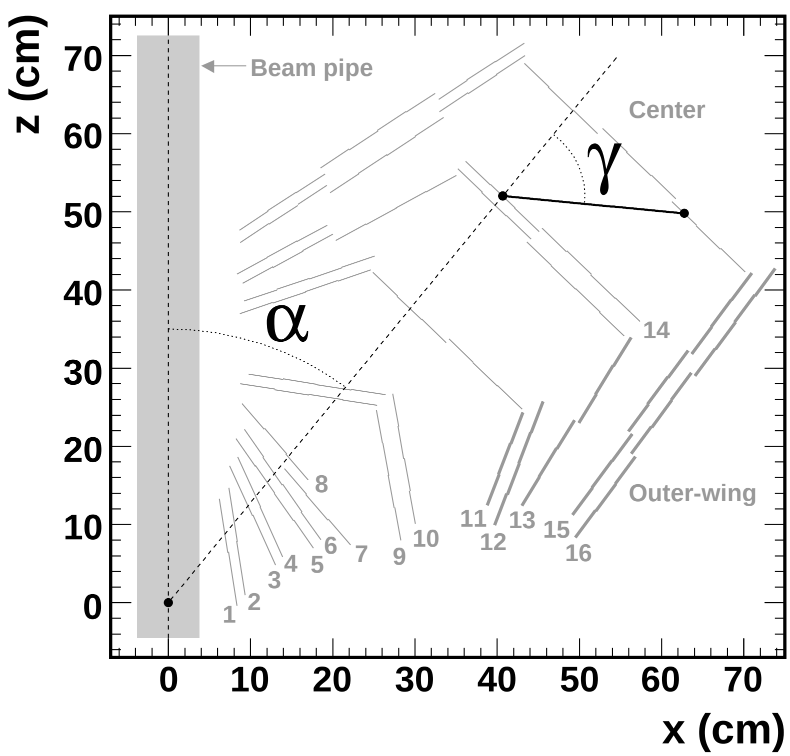

Figure 5.2: A Hough stick between layers 14 and 15 is characterized by two angles: the polar angle between the beam pipe and the first hit, α, and the angle between the two hits, γ. The Hough tracking presumes the independent calculation of the event vertex [16].

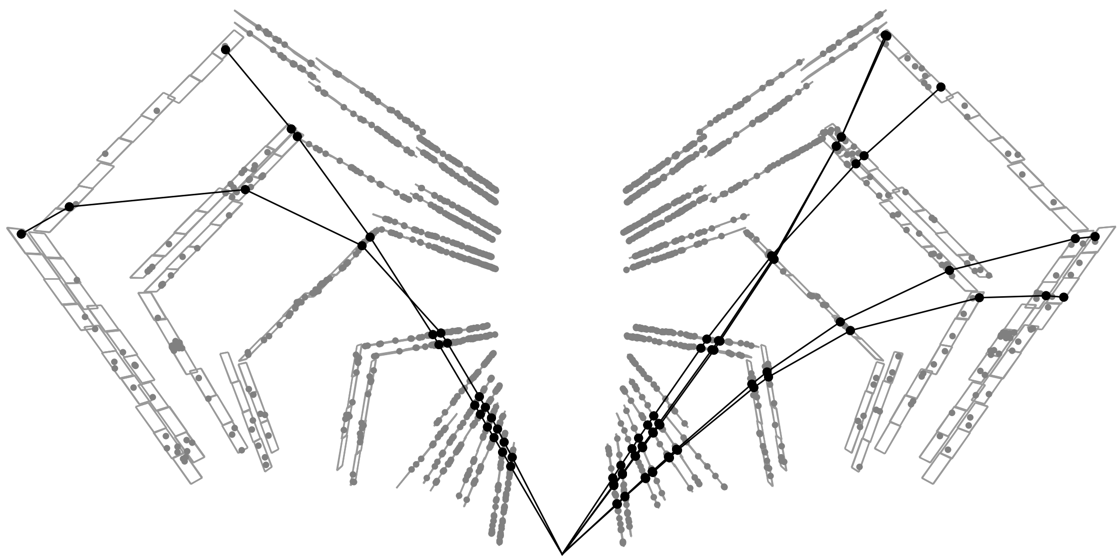

Figure 5.3: An example showing the reconstructed tracks in a central Au+Au event. The gray dots are Spectrometer hits that do not belong to a found track. The hits belonging to found tracks (black dots) are joined by straight line segments to guide the eye [16].

eters; if the sticks had similar values of $1/p$ and θ, they were chained together. As in the straight tracking, if more than one stick could be added to a chain, both candidates were retained.

The final curved tracks were required to contain five sticks (i.e. hits in all six outer layers). Additional cuts were made on fluctuations in the y-position and differences in deposited energy. Finally, the χ^2 was calculated on deviations of hit positions from the expected trajectory, to reject track candidates with low fit probability.

5.2.3 Full Track Momentum Determination

Once the straight and curved track segments had been constructed, they could be joined into full tracks if they shared matching parameters. An illustration of reconstructed full tracks in a central Au+Au event can be seen in Fig. 5.3. The full tracks were then subjected to successive momentum fits, after which a final clean-up was performed by rejecting duplicate tracks based on fit probability.

Track Matching

Several checks were performed on the combinations of straight tracks from the first six layers and curved tracks from the layer 9 onwards to determine if they should be joined. First, a consistent θ angle was required between the two segments ($\Delta\theta < 15$ mrad). Next, a relatively loose cut was made on the average energy losses in the two segments.

It was required that the difference between the average energy losses be no more than 80% of the overall average. This was designed, for example, to prevent the joining of a low momentum proton track in the straight section with a pion track in the curved section. Finally, a straight line fit was performed on the vertical positions of the hits in the curved section using the slope from the straight track. If the χ^2 divided by the number of degrees of freedom (i.e. the six hits) was greater than five, the joined track was rejected. If the criteria were all met, a full track was created with a preliminary θ and ϕ angle from the straight track values, and a total momentum p from the curved track section.

Track Fitting

The usual method of determining the momentum of a track is to fit an analytical form to the collection of hits. However, as has already been mentioned several times, the dipole design of the PHOBOS magnet caused particles to experience non-uniform fields as they traversed the Spectrometer. Instead, the trajectory was determined by swimming a particle through the magnetic field, whose strength was measured at many points and stored in the field map shown in Fig. 2.4(b). Starting with the track origin and momentum direction, the trajectory was traced out in steps using a Runge-Kutta algorithm. To minimize the required computing time, rather large steps (e.g. 10 cm in the central region) were used in regions of uniform field strength. Where there were large gradients (1Tesla/5 cm) the step size was reduced by a half.

Using this trajectory, the χ^2 of a track could be determined from the deviation of its hits from their expected positions. The ideal trajectory of a charged particle through a magnetic field does not, however, account for the effects of energy loss and multiple scattering undergone by real tracks passing through the silicon. The expected residuals were contained in the covariance or error matrices. The diagonal elements of these matrices corresponded to the residuals on hit positions in a single layer. Due to the fact that a large angle scattering in one layer would tend to produce correlated deviations in all subsequent layers, it was *essential* to estimate the off-diagonal elements of the covariance matrices.

Like the Hough tables, the covariance matrices were generated before data-taking to be looked up by the tracking. Matrices were generated separately for the two bending directions, 40 bins of $1/p$ ranging from $p = 0.1 - 10$ GeV, 60 bins in z-vertex from -20 to 10 cm, and 30 bins in polar angle (0.25 rad $< \theta <$ 1.75 rad). The covariances were determined by first swimming a pion through the detector with the starting parameters of the particular bin (q,v_z,θ,$1/p$), assuming an ideal trajectory, i.e. with energy loss and multiple scattering turned off. Then, 5000 pions were generated with energy loss and multiple scattering turned on. The deviations from the ideal trajectory were stored in that bin of the covariance matrix container for later look-up in the tracking.

The actual determination of the best fit entailed the iterative minimization of the χ^2 for five parameters describing the track ($1/p$,θ,ϕ,z_0 and y_0). A simplex routine was used to find the χ^2 minimum. A simplex is a collection of points connected by line segments defining a surface in an n-dimensional space[2]. With initial positions randomly assigned near the input values from the track matching, the χ^2 was calculated at each vertex of the simplex, and the point with the largest value reflected through the opposite face. Repetition of this maneuver resulted in the simplex approaching the minimum until a user-defined cut on incremental improvement was reached. To avoid accidentally settling into a 'local minimum', the minimization procedure was repeated a number of times with different initial random settings.

Duplicate Rejection

The final step in the tracking process was to check tracks for shared hits. If a number of hits were shared by more than one track, it was likely that only one true track existed and that the other(s) were ghosts. To maximize the purity of the final sample, tracks were not allowed to share more than two hits. If they did, the track with the lower fit probability was assumed to be a fake and discarded.

[2]A two-dimensional simplex is a triangle. A three-dimensional simplex is a tetrahedron

6 Obtaining Charged Hadron Spectra

Tracks found in the Spectrometer are used to construct the charged hadron transverse momentum spectra, which are presented in terms of the 'invariant yield'. This quantity describes the number of particles (N) found in a particular momentum range $\vec{p} = (\vec{p}, \vec{p} + d\vec{p})$.

$$E\frac{d^3N}{d^3\vec{p}} = E\frac{d^3N}{dp_x dp_y dp_z} \tag{6.1}$$

Recast into cylindrical coördinates, the invariant yield can be integrated over the azimuthal angle ϕ, as the average single-particle spectra is symmetric in this variable.

$$E\frac{d^3N}{d^3\vec{p}} = \frac{E}{p_T}\frac{d^3N}{dp_T d\phi dp_z} = \frac{E}{2\pi p_T}\frac{d^2N}{dp_T dp_z} \tag{6.2}$$

Using the expressions $E = m_T \cosh(y)$ and $p_z = m_T \sinh(y)$ (see Appendix B), the invariant yield can be written in terms of rapidity (y).

$$E\frac{d^3N}{d^3\vec{p}} = \frac{1}{2\pi p_T}\frac{d^2N}{dp_T dy} \approx \frac{1}{2\pi p_T}\frac{d^2N}{dp_T d\eta} \tag{6.3}$$

Since rapidity transforms additively under Lorentz boosts (y'=y+const.), it is clear that the invariant yield does not depend on reference frame (dy'=dy). Because this analysis does not identify the mass of the charged hadrons, rapidity is replaced by pseudorapidity (see Eq. 6.3). For relativistic particles ($E \gg m$) this is a very good approximation.

Calculating the invariant yield becomes a matter of counting the number of collision events and the number of tracks found in those events. The criteria for selecting collision events are discussed in Sect. 6.1; the track selection procedure is discussed in Sect. 6.2; the various corrections to the raw spectra are explained in Sect. 6.3.

6.1 Event Selection

Even after events had passed the trigger conditions described in Sect. 4.1, additional cuts were made to ensure the rejection of beam-gas events in favor of true collisions. A list of these cuts can be found in Table 6.1. For the Cu+Cu run, the standard IsCol selection was not finalized until after data processing had begun. For this reason, many trigger bits were set manually in this analysis of the data.

First, the difference between the positive and negative Paddle times (PdlTDiff) was required to be less than 5.0 ns. This selected collisions from the center of the detector (±75 cm), rejecting beam-gas events outside the Paddle region. Next, to avoid recording

Variable	Condition	Description
L1&0x0100	False	Remove heartbeat events
abs(PdlTDiff)	< 5.0 ns	Valid collision timing
TrgTExtra46	False	Exclude post-pileup events
TrgTExtra62	False	Exclude pre-pileup events
TrgTExtra7	True	Good L1 timing
OctProbMultVertex	Valid	Successful vertex reconstruction
OneTrackVertex	Valid	Successful vertex reconstruction
OctProbMultVertex	$-10 < v_z < 10$ cm	z-vertex within nominal range

Table 6.1: A summary of the event cuts used in the charged hadron spectra analysis of Cu+Cu collisions at $\sqrt{s_{\rm NN}} = 62.4$ and 200 GeV.

signals remaining in the detector from the previous collision, events that were triggered less than 5 μs after another event were flagged as 'pre-pileup'. Similarly, to avoid recording signal from the following event before the current collision had finished reading out, events that were triggered less than 0.5 μs before another event were flagged as 'post-pileup'. Finally, a good L1 timing required that when the previous event was rejected by the trigger logic, the fast clearing of the trigger signals had finished before the current event was recorded [87]. 'Heartbeat' events – periodic read-outs of the detector by the DAQ – also needed to be removed.

Events were also required to have a successfully reconstructed collision vertex in the range of the Spectrometer acceptance ($-10 < v_z < 10$ cm). OctProbMultVertex was used for the event vertex, but a valid OneTrackVertex was also required, since this vertex was used as a seed in the tracking algorithm.

The same vertex cuts were applied in the selection of MC events. The Paddle timing and pile-up cuts were not needed as there are no beam-gas or pile-up events in the MC.

6.2 Track Selection

Once collision events were selected, additional cuts were placed on tracks. Tracks were only taken from the pseudorapidity range $0.2 < \eta < 1.4$, within which the acceptance of the Spectrometer was relatively flat. This simplified the calculation of the differential yield in pseudorapidity (the $d\eta$ in Eq. 6.3), such that it only required dividing by the selected eta range ($1.4 - 0.2 = 1.2$).

Tracks with a very poor momentum fit probability were also rejected. The fit probability value corresponded to the likelihood that a track with the same properties would be assigned a higher χ^2 value in the track fitting procedure. For correctly calculated covariances of Gaussian-distributed measurements, a flat probability distribution would be expected. The large deviation from this expectation for tracks with fit probability below 4% indicated that the momentum of these tracks was not properly reconstructed (see Fig. 6.1(a)). Since they were most likely 'ghost' tracks, constructed from incorrectly

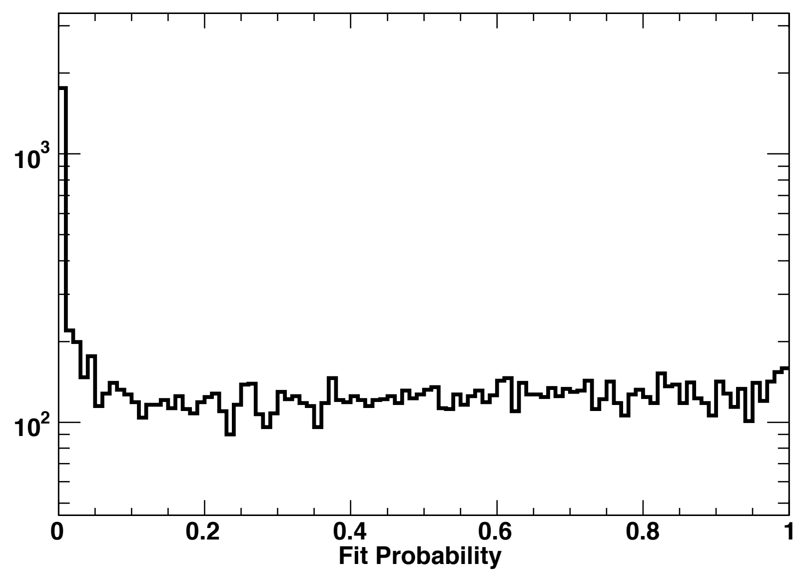

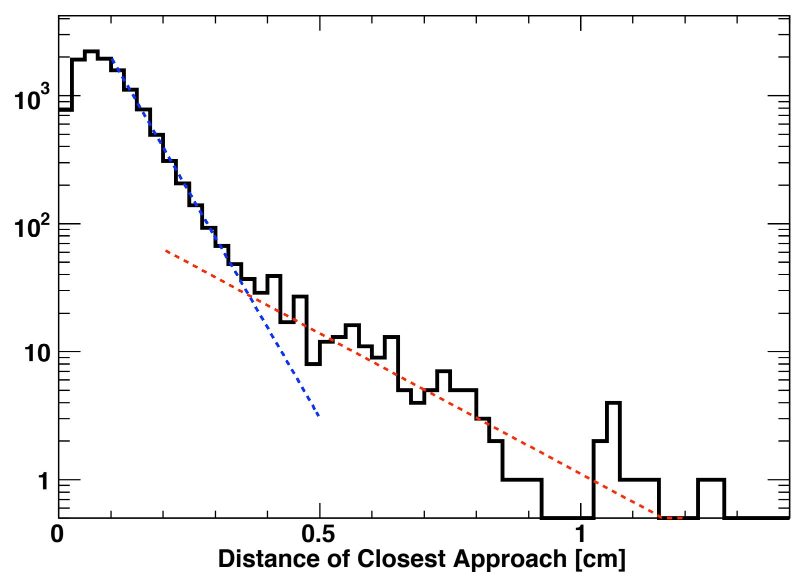

Figure 6.1: (a) Fit probability distribution of found tracks. Notice the excess of 'ghosts' below 0.04 that are removed by the cut. (b) The distribution of DCA, the distance of closest approach of found tracks to the event vertex. The two lines are exponential fits in the regions dominated by primaries and secondaries. The cut is placed at 0.35 cm, where the secondary contribution begins to dominate.

Variable	Minimum	Maximum
Rapidity (y)	0.0	1.5
Transverse Momentum (p_T)	0.1 GeV/c	10.0 GeV/c
Azimuthal Angle (ϕ)	-0.2	+0.2
Vertex Position (v_z)	-15 cm	+10 cm

Table 6.2: The ranges over which MC single pions were simulated for determination of the acceptance and efficiency correction.

matched hits, tracks with fit probability less than 0.04 were excluded from the analysis.

Secondary particles, that is those not originating from the Cu+Cu collision, were rejected using a cut on the Distance of Closest Approach (DCA). In the last stage of the momentum fit, tracks were not constrained to originate from the collision vertex. The value of DCA is defined as the closest distance between the fitted track trajectory and the collision vertex location. Because secondary tracks began to dominate above DCA$\sim$ 0.35 cm, a cut was placed at that distance to maximize the fraction of primary tracks (see Fig. 6.1(b)).

6.3 Corrections to Raw Spectra

Ideally one would use a detector that perfectly reconstructs all the particles originating from a collision event. However, in the real world, a number of corrections must be applied to account for detector effects that make the number of reconstructed particles differ from the number of true particles. The largest single correction accounts for the limited acceptance of the detector and the track reconstruction efficiency. Additional factors correct for momentum resolution and finite p_{T}-binning, 'ghost' tracks, secondaries and feed-down decays, tracks lost due to high occupancy, and dead and hot Spectrometer pads.

6.3.1 Acceptance and Efficiency Correction

The combined correction for the acceptance of the detector and the efficiency of track reconstruction was estimated by swimming single-tracks through a simulation of the detector and calculating the fraction that were reconstructed using the same cuts as in the data. In total 35 million events were generated, each with a single MC pion embedded into an empty event. Both magnet polarities, both track charge signs, and both Spectrometer arms were generated with equal statistics. Single pions were embedded with flat distributions in rapidity, transverse momentum, and azimuthal angle. The respective ranges are listed in Table 6.3. The event vertex was chosen randomly from a flat v_z distribution between -15 and +10 cm. The simulated ϕ range was chosen to cover the full Spectrometer acceptance, but not the complete 2π azimuthal angle. Therefore, an additional factor of ($2\pi/0.8 \approx 7.85$) was applied to correct the raw results to the azimuthally averaged quantity in Eq. 6.3.

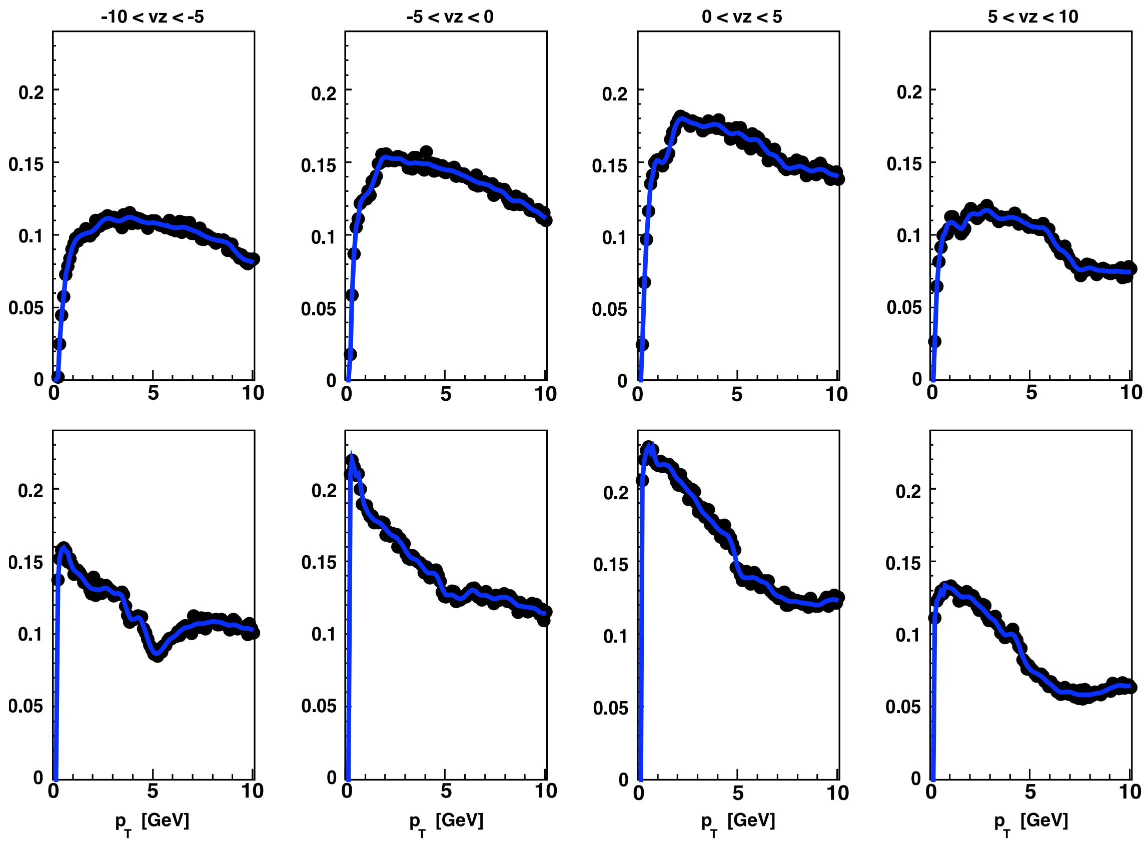

Figure 6.2: Correction factor for acceptance and efficiency as a function of transverse momentum for four vertex bins ($-10 < v_z < -5$ cm, $-5 < v_z < 0$ cm, $0 < v_z < +5$ cm, and $+5 < v_z < +10$ cm) and two bending directions (top row: positive charge-polarity, bottom row: negative charge-polarity). The corrections are averaged over the two Spectrometer arms.

The correction function was calculated separately for the two bending directions and for four vertex ranges ($-10 < v_z < -5$ cm, $-5 < v_z < 0$ cm, $0 < v_z < +5$ cm, and $+5 < v_z < +10$ cm). Each correction was constructed by dividing a histogram binned in p_T of reconstructed tracks that passed the DCA and fit probability cuts by a histogram of the embedded tracks. The resulting histograms were smoothed to remove statistical fluctuations except in the quickly changing part at low-p_T. The correction functions for each vertex range and bending direction are shown as a function of p_T in Fig. 6.2. Particles with negative charge-polarity bend away from the beam, accounting for the larger acceptance at low momentum. (Recall that the tracking algorithm was not performed in the Inner Wing due to high hit densities – see Fig. 5.2 and 5.3.)

It should be noted that in both cases the tracks were binned based on the true momentum not the reconstructed momentum. The difference between the two is separately accounted for by the momentum resolution correction in Sect. 6.3.2. Ghost tracks

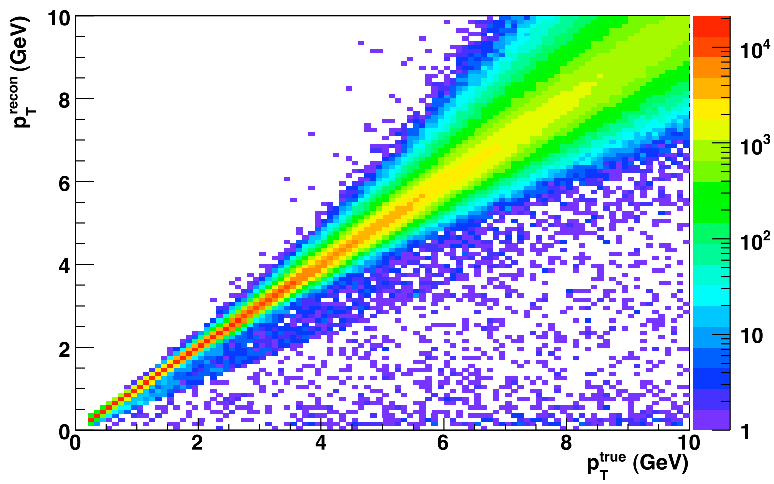

Figure 6.3: The momentum resolution shown is a p_T dependent function determined by single-track studies of reconstructed versus true momentum.

and secondaries did not contribute to this correction, since if the simulation resulted in more than one 'findable' track or if more than one track was found, the whole event was rejected. This occurred in <1% of simulated events.

Whereas the tracking routine in these studies was given the exact vertex position from which the single tracks were generated, it was considered that the resolution of One-TrackVertex in the data might cause some inefficiency in the tracking that would not be accounted for by this correction. Studies of single-tracks reconstructed from smeared vertex positions concluded that no additional tracks were lost until the vertex strayed by more than ±7.5 mm. Since the resolution on OneTrackVertex ranges from 1 mm in central events to 3 mm in peripheral events, the calculated efficiencies should be sufficient.

6.3.2 Momentum Resolution and Binning

The combination of a steeply falling p_T spectrum and a finite resolution in the momentum determination results in an excess of particles at higher p_T in the raw spectra. Correcting for this effect required the precise determination of the momentum resolution as a function of transverse momentum. Shown in Fig. 6.3 is a comparison of the true generated momentum to the reconstructed momentum for the single-track sample discussed in Sect. 6.3.1.

The determination of the correction proceeded in a number of steps:

1. The measured raw p_T spectrum was fit with a functional form (see Fig. 6.4(a)).

2. The reconstructed p_T distribution in each true p_T bin was taken from Fig. 6.3 and normalized to the same integral.

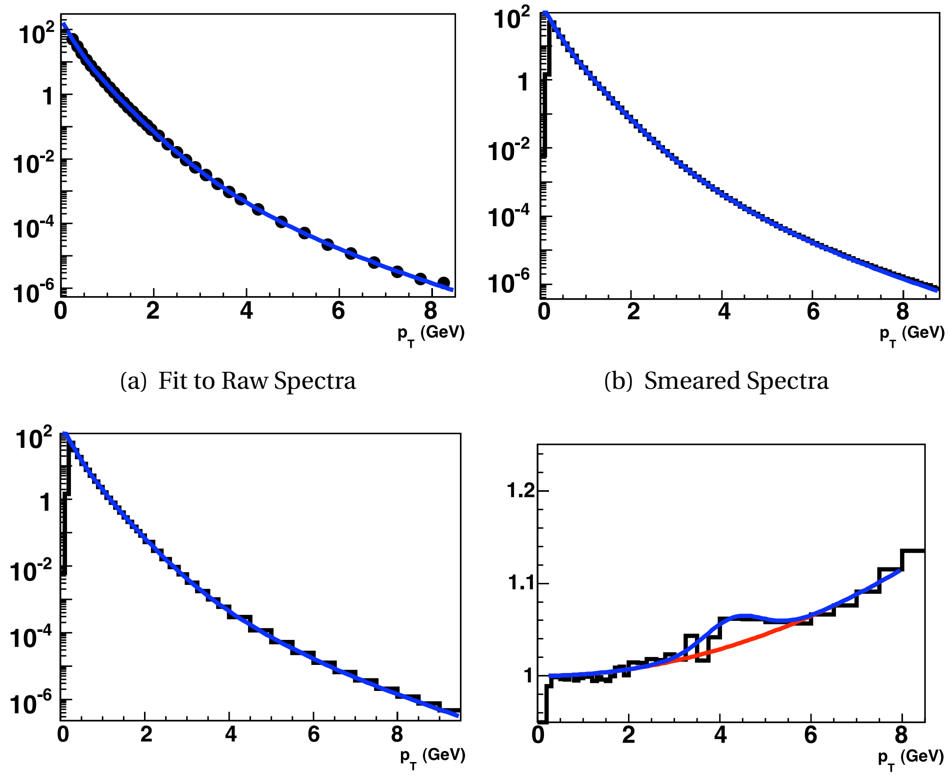

(a) Fit to Raw Spectra

(b) Smeared Spectra

(c) Re-binned Spectra

(d) Momentum Resolution Correction

Figure 6.4: (a) Power law + exponential fit to measured, raw p_{T} spectra with small polynomial correction to ensure fit quality better than 10%. (b) Spectra smeared by momentum resolution. (c) Smeared spectra re-binned in same bins as data. (d) Final correction is the ratio of (c) to (a), fit with a second-order polynomial plus a Gaussian to account for the change in bin width.

3. The reconstructed p_{T} distribution was weighted by the value of the fit evaluated at the center of each true p_{T} bin.

4. The weighted 2-D histogram was projected onto the reconstructed p_{T} axis and divided by bin width and $(2\pi p_T)^{-1}$ to get the smeared p_{T} spectra (see Fig. 6.4(b)).

5. The smeared p_{T} spectra were re-binned into the same binning as the data (see Fig. 6.4(c)).

6. The re-binned, smeared p_{T} spectra were divided by the fit to the raw spectra and the ratio fitted with a polynomial + Gaussian function (see Fig. 6.4(d))[1]. This was the momentum resolution and binning correction that was applied to the measured spectra.

[1]Previous analyses did not account for bin width changes, covered by the assigned systematic error.

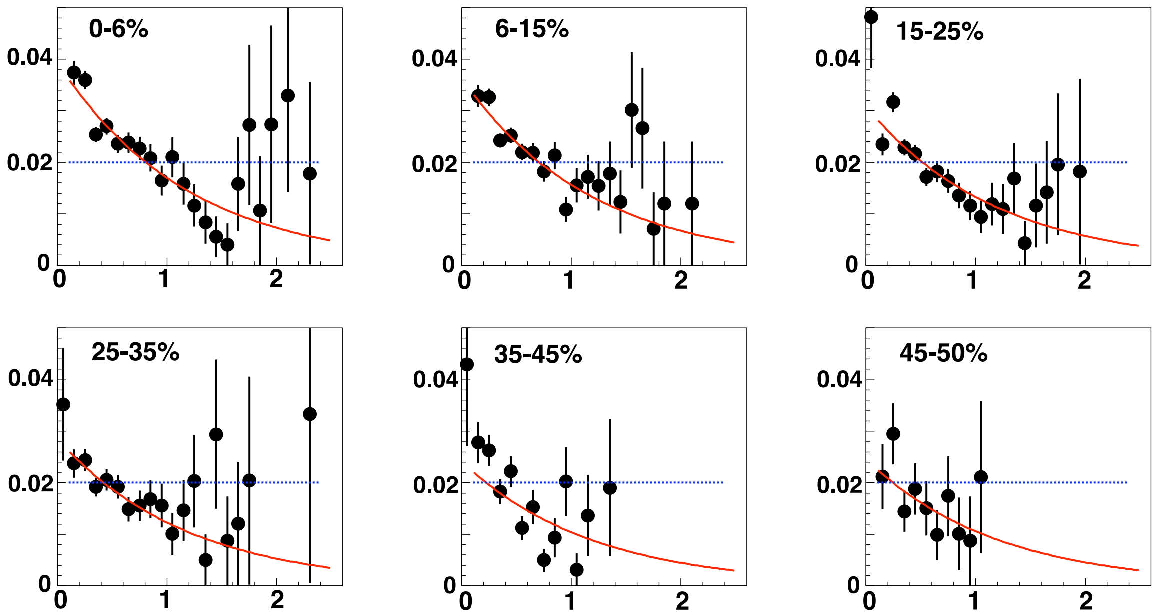

Figure 6.5: Ghost fraction in 200 GeV Cu+Cu events as a function of p_T for six centralities (0-6%, 6-15%, 15-25%, 25-35%, 35-45% and 45-50%). Exponential fits use the same width for all centralities. The dashed line represents the systematic error assigned to this correction.

6.3.3 Ghost and Secondary Corrections

Besides correcting for tracks lost due to acceptance and efficiency, one must also account for a surplus of reconstructed tracks not belonging to any primary track. Whereas the acceptance correction could be estimated using single-tracks, estimating the non-primary contribution required full simulations of Cu+Cu events generated by HIJING; the statistics were limited by the size of the simulated HIJING sample. One source of non-primary tracks, called 'ghosts', came from the reconstruction of tracks from hits not belonging to any one track. Another source came from fully reconstructed secondary tracks, including feed-down from weak decays.

Determining the ghost and secondary fractions required matching reconstructed tracks to the known track trajectories from HIJING. If a simulated HIJING track deposited energy in the same silicon pad as a hit belonging to a reconstructed track, the hit was considered to be shared. The best track match was the one with the most shared hits. Secondaries were identified as reconstructed tracks with a non-primary best match. Ghosts were reconstructed tracks that did not share more than nine hits with any simulated particle.

The ghost fraction was simply the number of reconstructed tracks identified as ghosts divided by the total number. This ratio was first determined as a function of p_T for the average of all centrality bins and fitted with an exponential. Then, an exponential fit to the ghost fraction was separately performed in each centrality allowing only the ampli-

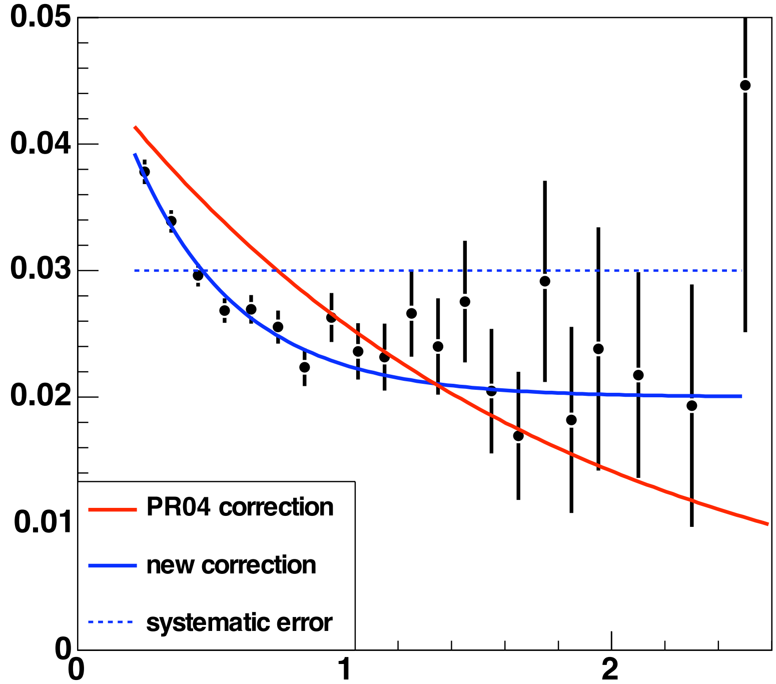

Figure 6.6: Secondary and feed-down fraction for 200 GeV Cu+Cu for all centralities from 0-50%. The correction is an exponential plus constant offset fit to the non-primary fraction. The assigned systematic error is indicated by a dashed line.

tude to vary. The width was fixed to the value extracted from the average. Figure 6.5 shows the ghost fraction and the corresponding exponential fits for six centrality bins in Cu+Cu events at $\sqrt{s_{\mathrm{NN}}} = 200$ GeV.

Since the secondary fraction does not depend much on centrality, the correction was calculated as a function of p_{T} for all centralities together. The secondary correction is illustrated in Fig. 6.6, where it has been fit with an exponential plus a constant offset term. The inclusion of the constant offset, which was not present in earlier studies of secondaries [76], provided a better overall fit to the higher statistics HIJING sample used in this study. The systematic error on the non-primary fraction (i.e. secondary + feed-down) was chosen conservatively to reflect the relatively large uncertainty in weakly decaying parent distributions in HIJING.

6.3.4 Occupancy Correction

Because the efficiency correction in Sect. 6.3.1 was calculated using only single-tracks, it was necessary make an occupancy correction to account for the increased likelihood of losing tracks in a high multiplicity environment. To evaluate the correction, single-tracks were embedded with a flat p_{T}-distribution into real data events binned in cen-

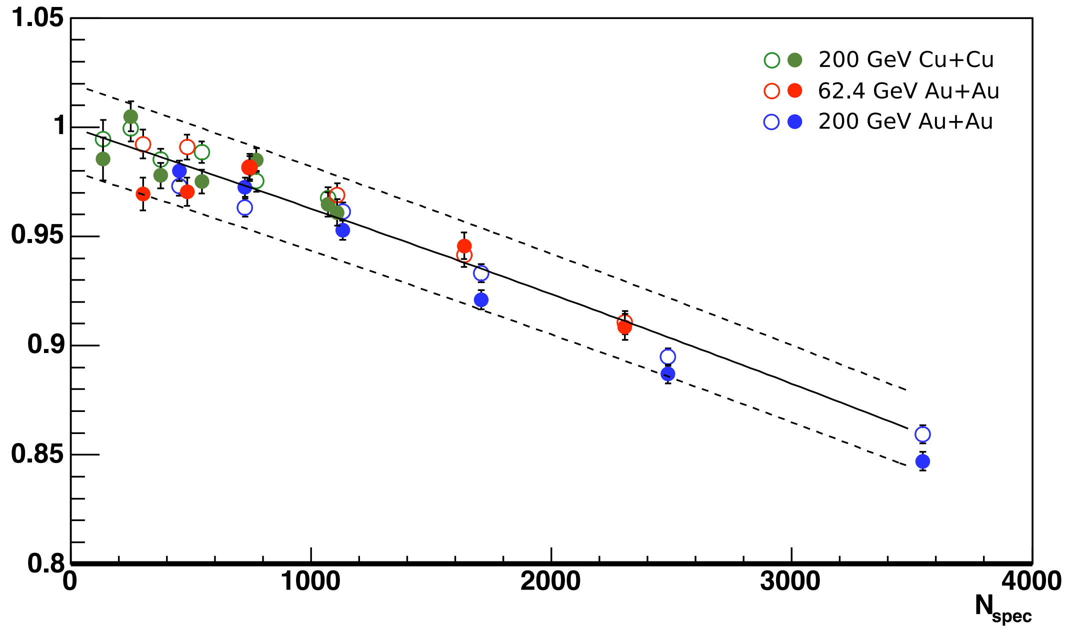

Figure 6.7: Occupancy corrections in Au+Au and Cu+Cu plotted together versus the number of Spectrometer hits. The dashed lines represent a ±2% systematic error.

trality. The fraction of embedded tracks that were reconstructed had a similar p_{T} dependence as the single-tracks with an overall decrease in efficiency that was most pronounced for central collisions. In central Au+Au events this correction was on the order of 10-15% [93]; for central Cu+Cu, the effect was less pronounced. In fact, the occupancy factor appears to scale smoothly with the number of Spectrometer hits for both species at two energies (see Fig. 6.7).

6.3.5 Dead and Hot Spectrometer Pads

One final correction was required to account for faulty Spectrometer channels. As described in Sect. 3.3, a map was created of all the dead, hot and noisy channels (collectively referred to here as simply 'dead'). For practical considerations, the tracks in the data were reconstructed without masking out dead channels[2]. Also, the effect of dead channels was not considered in the acceptance and efficiency correction in Sect. 6.3.1. To properly account for dead channels, one would like to mask them out before track finding, both in the data and in the single track simulations used to estimate the efficiency.

[2]First, the track reconstruction could proceed without waiting for a dead channel map, and second, the map could be changed at a later date, only affecting the correction.

$$\text{Yield} \propto \frac{\text{Data Tracks (Masked)}}{\text{Single Track Efficiency (Masked)}} \tag{6.4}$$

However, since neither the data nor the single tracks were reconstructed with the dead channels masked, the yields had to be multiplied by a correction factor equal to the following:

$$\text{Correction} = \left(\frac{\text{Data Tracks (Masked)}}{\text{Data Tracks (Unmasked)}}\right) \Big/ \left(\frac{\text{Single Tracks (Masked)}}{\text{Single Tracks (Unmasked)}}\right) \tag{6.5}$$

The correction was calculated from a sub-sample of the full data set, by counting the number of tracks found with and without applying the dead channel mask. It was computed as a function of transverse momentum, in consideration of the possibility that the spatial distribution of dead channels might affect the tracking differently at different momenta. Despite only a few percent of Spectrometer channels being dead, their effect on the efficiency was magnified by the large number of hits required to reconstruct a track (see Sect. 5.2). The ratios in Eq. 6.5 were found to equal 0.9146 in data and 0.8471 in MC, independent of p_{T}. The applied correction was $0.9146/0.8471 = 1.080$.

The magnitude of the above ratios can be understood by considering the two extreme limits. In the limit where all the masked channels are completely dead, the ratio of masked to unmasked samples in data would be one, since the masked channels would have recorded no hits. For the single tracks, the ratio of masked to unmasked samples would be some amount less than one corresponding to the lost acceptance. In the other limit, where none of the masked channels are dead, applying the mask simply corresponds to removing some acceptance from the detector. In this case, the ratio in data would be less than one by the same amount as the single tracks. In reality, the situation was somewhere between these two extremes. The fact that the ratio in data was significantly below unity reflects the hard cuts used in the creation of the dead channel map to ensure quality data.

Whereas for the d+Au run, there was a large discrepancy in the number of dead channels between the positive and negative Spectrometer arms[3], the situation was much more symmetric in the later Au+Au and Cu+Cu runs. For this reason, the same correction was applied for both arms, with the possibility of a slight difference being covered by the 4% systematic error assigned to this correction.

6.4 Summary of Systematic Errors

The systematic errors assigned to each correction are shown in Fig. 6.8. The largest single uncertainty, arising from the acceptance and efficiency correction, was quantified by comparing the yields in different sub-samples of the data. This included the yields calculated separately for the two different magnet polarities, the two Spectrometer arms,

[3]The concentration of channels classified as dead in the fifth layer of the negative arm exacerbated the discrepancy.

and the four z-vertex bins. The particular p_T dependence of the acceptance and efficiency error was chosen to cover the variation observed in each of these sub-samples.

The systematic error assigned to the momentum resolution and binning correction comes from two sources. First, an error of 1.6%+0.4%*p_T was estimated for the non-commutativity of the momentum smearing and tracking efficiency. Second, a 10% error on the fit to the spectral shape and a 10% error on the momentum resolution combined to give a 15% error on the size of the final correction.

The errors assigned to the other corrections are discussed in the preceding sections. As shown in Fig. 6.8, the final quoted systematic error consisted of the separate errors added in quadrature.

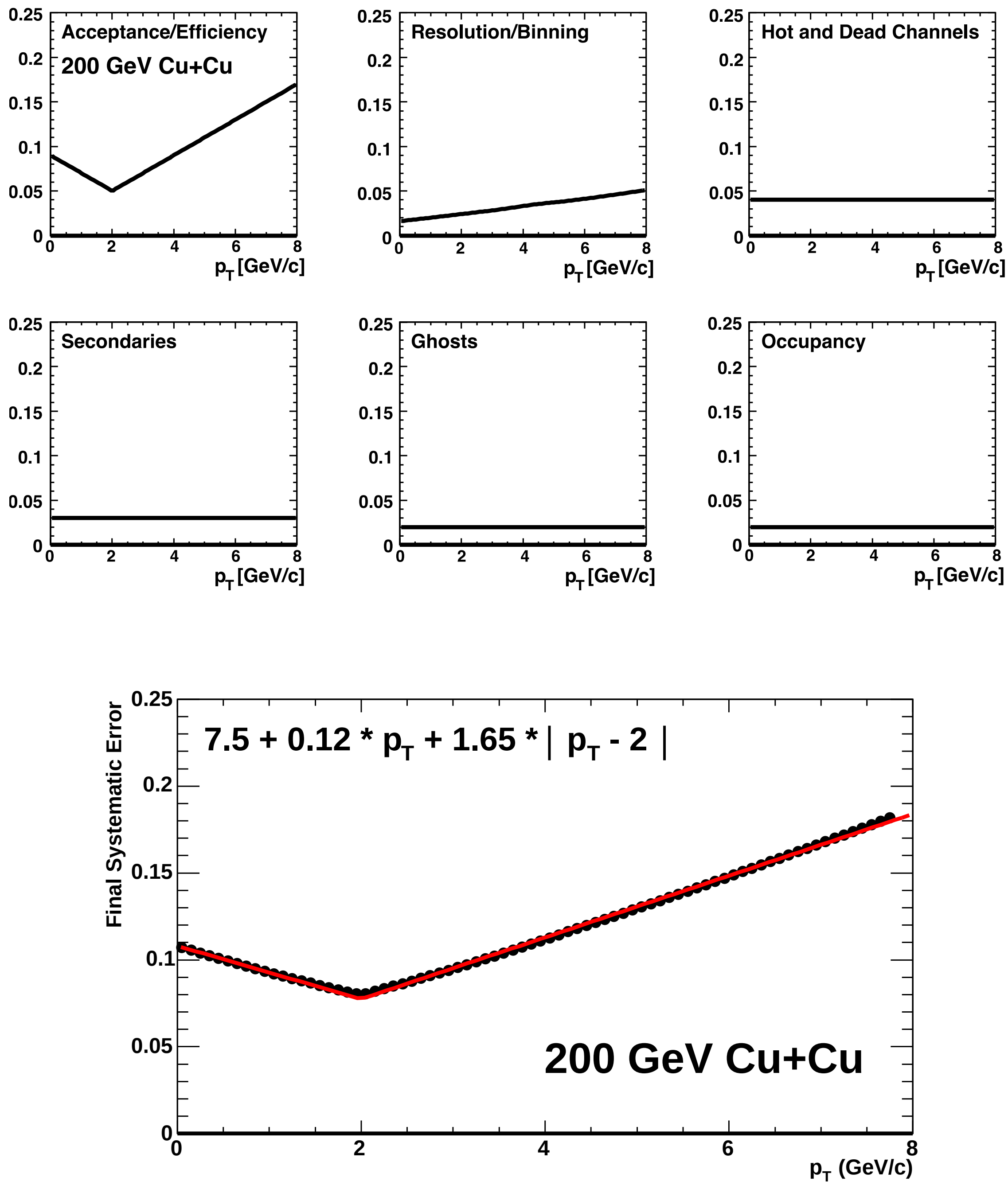

Figure 6.8: The various contributions to the systematic error in 200 GeV Cu+Cu and their sum in quadrature, corresponding to the final quoted error.

7 Cu+Cu Spectra Results and Discussion

Using the analysis methods described in the previous chapter, the Cu+Cu spectra have been measured at $\sqrt{s_{NN}} = 62.4$ and 200 GeV. These measurements were motivated by previous spectra results from Au+Au collisions at $\sqrt{s_{NN}} = 62.4$, 130, and 200 GeV, which showed a strong suppression relative to the expectation of binary collision scaling [57–59, 94, 95]. As described in Sect. 1.6.3, the absence of such a suppression in d+Au collisions supported the interpretation of parton energy loss in the final state [55, 60, 61]. The Cu+Cu spectra presented in this thesis (and published in [63]) bridged the gap between the d+Au and Au+Au systems, allowing an examination of the dependence of high-p_T suppression on system size.

To quantify the observed suppression, a reference spectrum was constructed from charged hadron measurements in p+p (or p+p̄) collisions. This reference spectrum was used to calculate the nuclear modification factor (see Eq. 7.1) as a function of centrality and transverse momentum. The suppression in Au+Au and Cu+Cu was then compared to various model calculations to elucidate the dependence of parton energy loss on path length.

7.1 p+p Reference Spectra

The charged hadron transverse momentum spectra have been measured for 200 GeV p+p̄ collisions by the UA1 experiment [96]. Their results are shown in Fig. 7.1, where they have been divided by a fitted power law function. This fit function had to be corrected for the different angular acceptances of PHOBOS and UA1. Whereas the PHOBOS Spectrometer covered the range $0.2 < \eta < 1.4$, the UA1 results were measured for $|\eta| < 2.5$. A correction to account for the different acceptances was constructed using the PYTHIA event generator [97]. p+p̄ events were generated at 200 GeV and the resulting 'true' tracks from the different pseudorapidity acceptances were histogrammed in p_T. The resulting correction was just the ratio of these two histograms [93].

The charged hadron spectra in the range $p_T = 0.25 - 3.0$ GeV/c have been measured at the Intersecting Storage Rings (ISR) in 62 GeV p+p collisions [98]. Additionally, identified pions for $p_T = 3.8 - 12$ GeV/c were measured at 63 GeV [99]. Using the ratios π^+/h^+ and π^-/h^- that were presented as a function of p_T in the latter paper, the high-p_T spectrum of charged hadrons could be inferred. The resulting fit to the combined spectra was a power law of the form $43.231(1 + p_T/2.188)^{-15.37}$. The final p+p reference again incorporated a PYTHIA-based correction accounting for the difference between the PHOBOS acceptance and those of the ISR measurements ($0.5 < y < 1.0$ in [98] and $0.52 < y < 0.88$ in [99]).

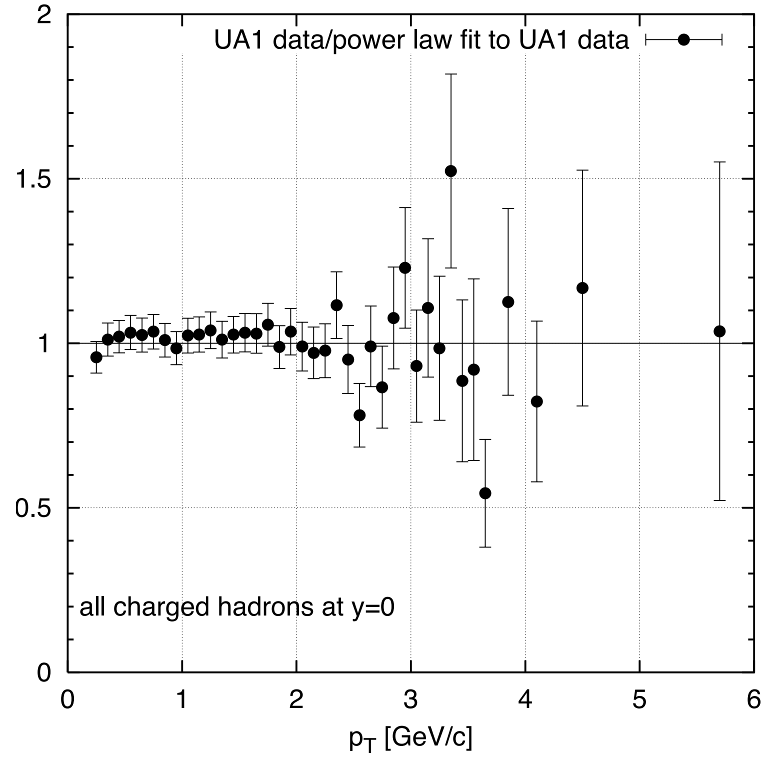

Figure 7.1: The charged hadron p_{T} spectra were measured by UA1 in p+p̄ collisions at $\sqrt{s_{\mathrm{NN}}} = 200$ GeV and fitted with the power law function, $50.9(1 + p_T/1.59)^{-11.2}$. Shown here is the ratio of the data to the fit.

7.2 Cu+Cu Spectra Results

Once the corrections detailed in Sect. 6.3 had been applied, the evolution of the yields with centrality and system size could be studied. The invariant yield of charged hadrons (see Eq. 6.3 on page 67) was obtained from the average of the positive and negative hadron yields. It is shown in Fig. 7.2 [63] as a function of transverse momentum and centrality for Cu+Cu collisions. At 62.4 GeV, the yields were measured in the interval $0.25 < p_{\mathrm{T}} < 5.0$ GeV/c, while at 200 GeV they were measured for $0.25 < p_{\mathrm{T}} < 7.0$ GeV/c.

Since the invariant yields span seven orders of magnitude, it is generally more instructive to normalize these spectra by the p+p references determined in Sect. 7.1. The nuclear modification factor R_{AA} is defined as the ratio of the nucleus-nucleus yield to the p+p yield scaled by the average number of binary collisions $\langle N_{\mathrm{coll}} \rangle$,

$$R_{AA}(p_T) = \frac{\sigma_{pp}^{inel}}{\langle N_{\mathrm{coll}} \rangle} \frac{d^2 N_{AA}/dp_T d\eta}{d^2 \sigma_{pp}/dp_T d\eta}, \tag{7.1}$$

where the differential cross-section in p+p is divided by the total inelastic cross-section σ_{pp}^{inel} to get the yield. Note that if the particle production in heavy ion collisions scaled with the number of binary nucleon-nucleon collisions, the value of R_{AA} would be equal to 1.

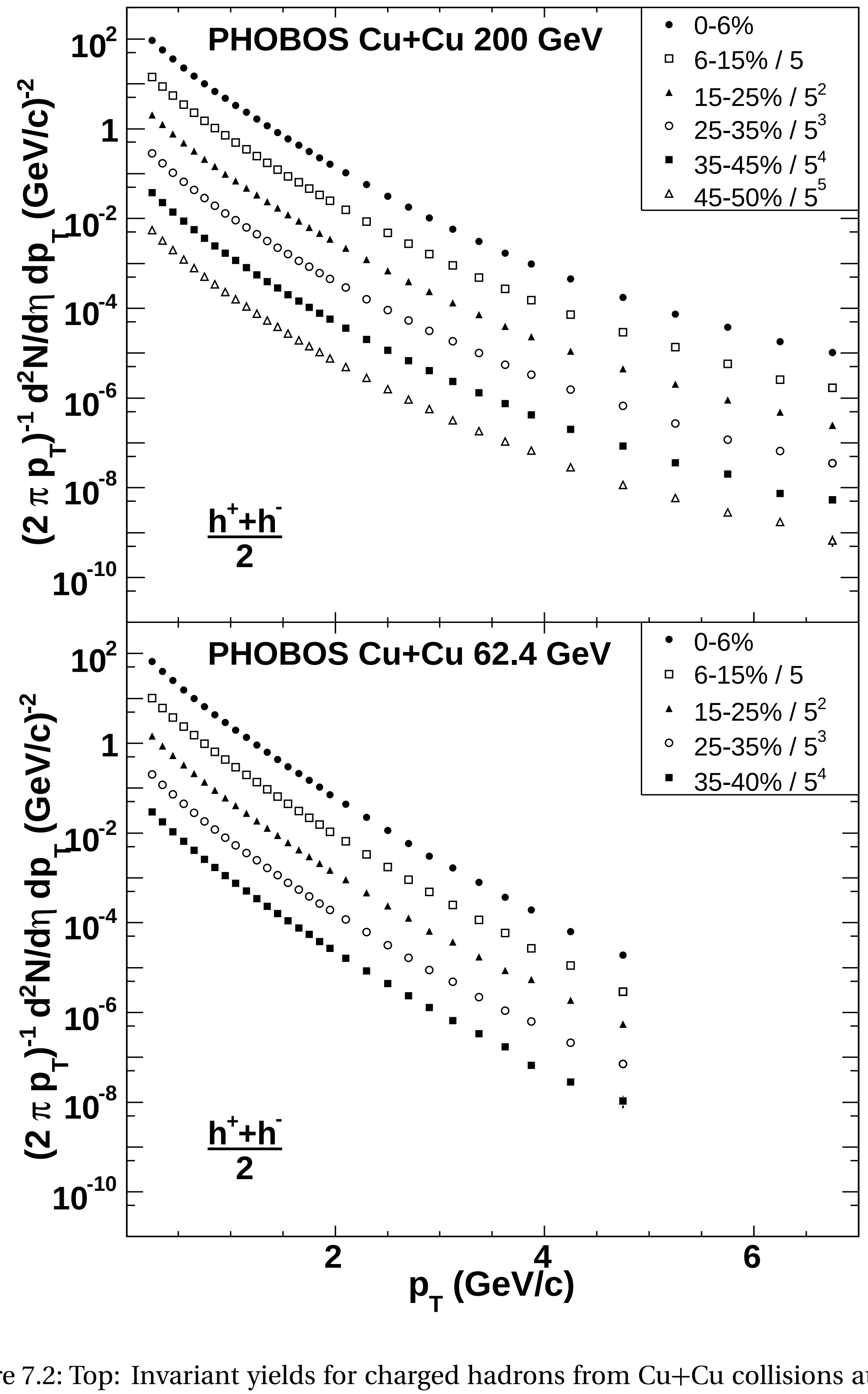

Figure 7.2: Top: Invariant yields for charged hadrons from Cu+Cu collisions at $\sqrt{s_{\rm NN}} = 200$ GeV in the pseudorapidity interval $0.2 < \eta < 1.4$ as a function of $p_{\rm T}$ for six centrality bins. Bottom: The same for $\sqrt{s_{\rm NN}} = 62.4$ GeV. For clarity, successive centrality bins are scaled by a factor of 5 [63]

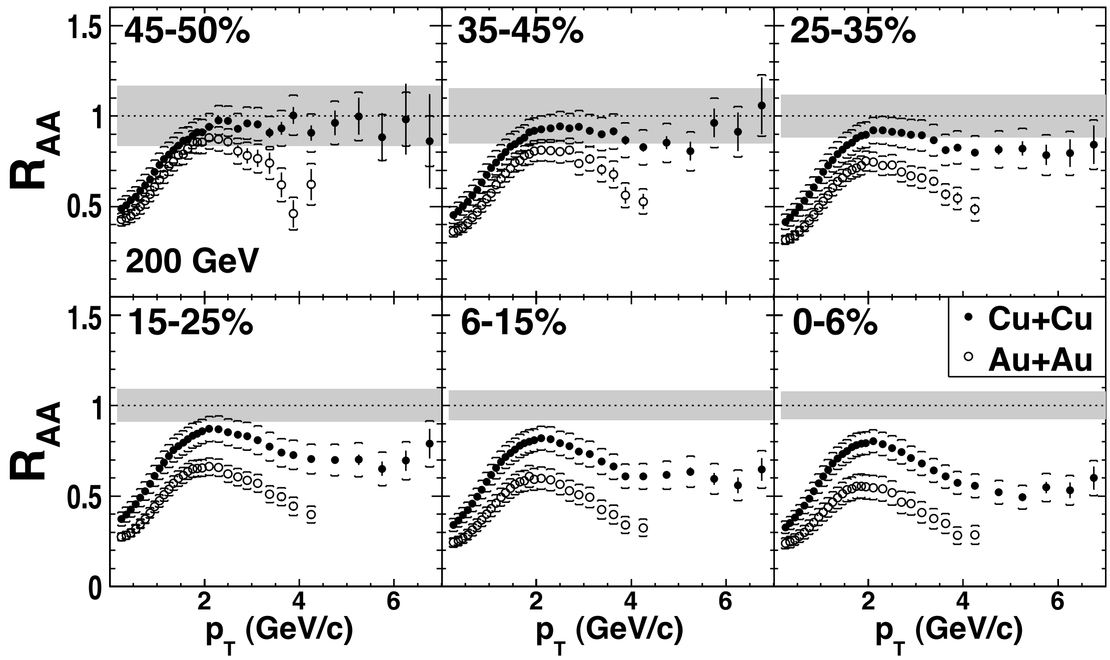

Figure 7.3: Nuclear modification factor, $R_{AA}(p_T)$, in bins of fractional cross-section for Au+Au (open symbols) and Cu+Cu (closed symbols) at $\sqrt{s_{NN}} = 200$ GeV. The gray bands indicate the uncertainty on the estimate of $\langle N_{coll} \rangle$.

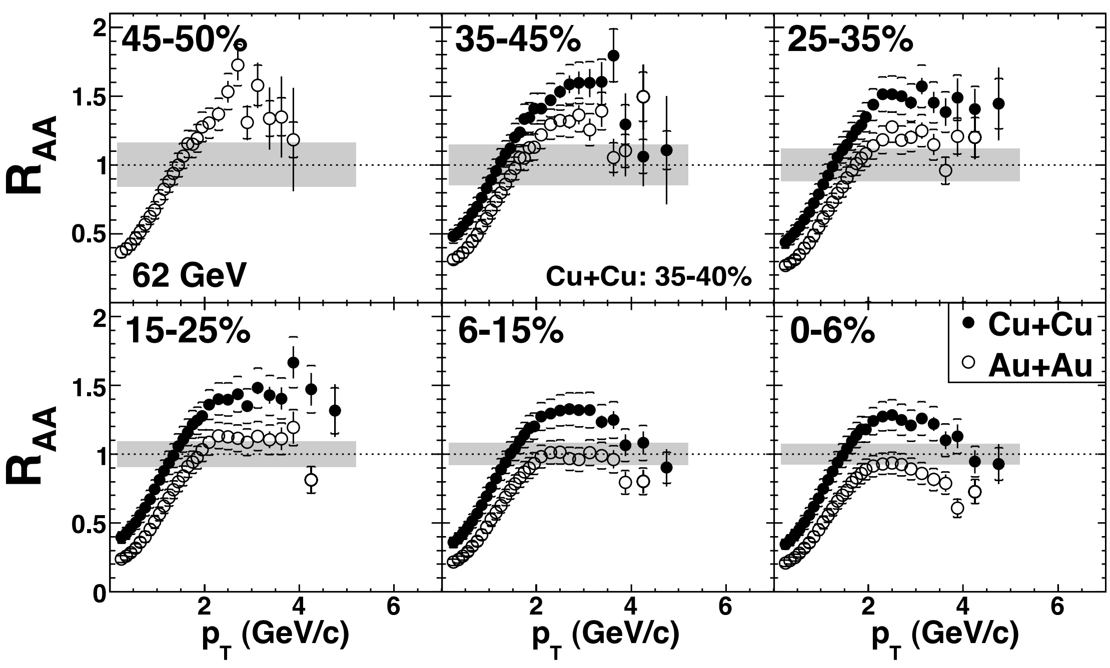

Figure 7.4: Nuclear modification factor, $R_{AA}(p_T)$, in bins of fractional cross-section for Au+Au (open symbols) and Cu+Cu (closed symbols) at $\sqrt{s_{NN}} = 62.4$ GeV.

The centrality evolution of $R_{AA}(p_T)$ is shown in Fig. 7.3 and 7.4 for Cu+Cu collisions at 200 and 62.4 GeV, respectively. As a comparison, the results for Au+Au collisions at both energies [57, 95] are also shown in the same fractional cross-section bins. Due to the inefficiency of the vertex reconstruction in low multiplicity events, the most peripheral bin analyzed in 62.4 GeV Cu+Cu was 35-40%.

At both energies, R_{AA} is greater in Cu+Cu than Au+Au for the same fractional cross-section bin. At 200 GeV (see Fig. 7.3), Cu+Cu collisions exhibit a high-p_T suppression ranging from approximately 0.5 in central collisions, to essentially no suppression in peripheral collisions.

7.2.1 Nuclear Effects on Spectra

The shapes of $R_{AA}(p_T)$, seen in Fig. 7.3 and 7.4, are related to the interplay of many nuclear effects that can enhance or suppress the spectra with respect to binary-scaled p+p. Even in p+A collisions, where there is no expectation of partonic energy loss from induced gluon radiation in the dense medium, the spectra are modified due to nuclear modification of the parton distribution functions and nuclear k_T broadening [100]. In the quantitative study of nucleus-nucleus collisions, it is also important to account for these effects.

From the Deep-Inelastic Scattering (DIS) of leptons or neutrinos from nuclei, the structure functions of the nucleus have been explored [101]. Compared to the structure functions of the deuteron[1], the amount of nuclear modification, F_2^A/F_2^D, depends on Bjorken x. For $x < 0.05 - 0.1$, the effect of 'shadowing' drives this ratio below one. The enhancement at $x \approx 0.1 - 0.2$ has been referred to as 'anti-shadowing'. At larger x, the ratio falls below unity again, called the EMC effect, then rises sharply as $x \to 1$ due to the Fermi motion of the nucleons within the nucleus. These effects increase with the size of the nucleus [102], and would be expected to differ between copper (A=63) and gold (A=197).

A large enhancement of hadron production, called the 'Cronin effect', has been seen in p+A collisions relative to p+p collisions scaled by the effective nuclear thickness [103]. The characteristic enhancement from the Cronin effect is clearly visible in Fig. 7.3 and 7.4 as a 'bump' around $p_T = 2 - 3$ GeV. This behavior has been ascribed to multiple initial-state scatterings [104, 105], which effectively increase the $\langle k_T^2 \rangle$ of the beam partons [2]. Although the general features of the Cronin effect can be described by such models, they cannot account for the much larger enhancement for baryons compared to mesons [103, 106]. This so-called 'baryon-meson anomaly' may be more successfully described by a final-state recombination approach [107]. While the phenomenology responsible for the Cronin effect is not completely understood, it bears careful consideration in the extraction of the energy loss from the nuclear modifica-

[1] The deuteron is used as the reference because heavier nuclei contain both protons and neutrons. Since the proton and neutron structure functions are known to be quite different, the deuteron is a better reference than the single proton.

[2] Note that the partons have some intrinsic k_T already, due to their confinement within the nucleon. By the uncertainty principle, the magnitude is on the order $\Delta p \approx 1/2\Delta x \approx 0.5$ fm^{-1} ≈ 100 MeV/c

tion factor – what might appear as no suppression could instead be the combination of Cronin enhancement and final-state energy loss.

7.2.2 Introduction to Jet Quenching

One of the most important discoveries at RHIC has been that, in addition to nuclear shadowing and the Cronin effect, jet energy loss has an important role in determining the final spectra. At high-p_T, the energy loss of partons can be treated formally within the framework of perturbative QCD (pQCD). Calculating the spectrum of gluon radiation from an energetic parton passing through a dense medium is analogous to the QED effect described by Landau, Pomeranchuk, and Migdal [108, 109].

The QCD formalism considers a very energetic quark of energy E propagating through a medium of length L [110]. Multiple scatterings from particles in the medium induce gluon radiation, leading to energy loss. The main assumption[3] in the calculation is that the energetic parton scatters independently from screened Coulomb potentials with Debye screening mass μ. This condition is related to the mean free path λ of the energetic parton as $\mu^{-1} << \lambda$, where λ depends on the density ρ of the medium as $\lambda = 1/\rho\sigma$ [110].

The calculation of quenching weights [112], namely the probability P(ΔE) that an energetic parton will lose a fraction of its energy ΔE, has been carried out in the two extreme approximations [93][4]:

- The multiple soft scattering limit, that is $L \gg \lambda$, known as the Baier Dokshitzer Mueller Peigné Schiff (BDMPS) model [111].
- The thin plasma limit of a single, hard scattering, known as the Gyulassy Lévai Vitev (GLV) model [114].

The effect of the medium on the incident parton is characterized by the *transport coefficient*:

$$\hat{q} = \frac{\langle k_T^2 \rangle}{\lambda} \tag{7.2}$$

where $\langle k_T^2 \rangle$ is the average transverse momentum squared that is transferred to the parton per unit path length λ. After multiple soft scatterings, gluons in the hard parton wavefunction are considered to be emitted if they have picked up sufficient k_T to decohere. As outlined in [112], the decoherence condition corresponds to picking up a phase difference φ of order 1.

$$\varphi = \left\langle \frac{k_T^2}{2\omega} \Delta z \right\rangle \sim \frac{\hat{q}L}{2\omega} L = \frac{\omega_c}{\omega} \tag{7.3}$$

[3]This assumption allows a treatment of 'time-ordered' scattering events, neglecting the amplitudes from four-gluon vertices as in Fig. 1 in [111].

[4]In the limit of strong LPM suppression, where BDMPS is valid, these two formalisms have been shown to be equivalent [113].

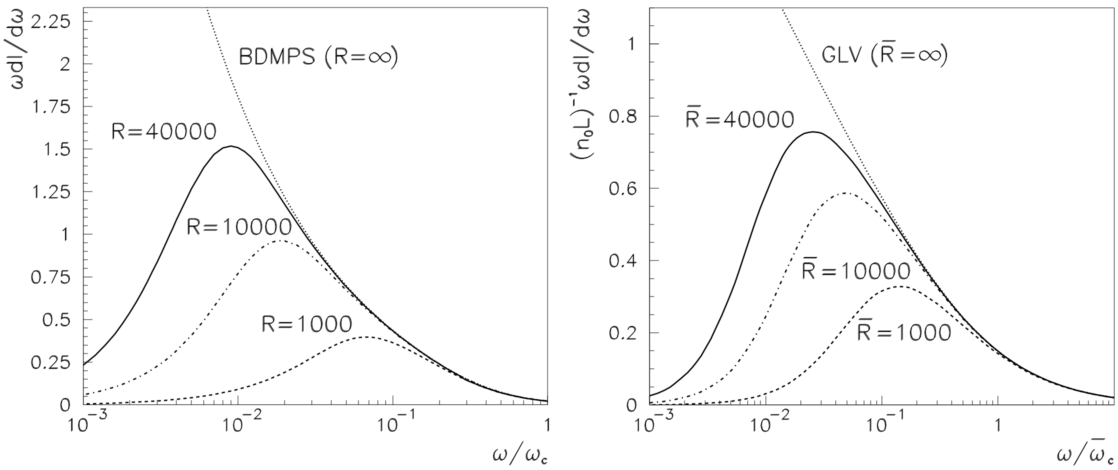

(a) Multiple scattering limit (BDMPS) (b) Thin plasma limit (GLV)

Figure 7.5: Medium induced gluon radiation distribution $\omega dI/d\omega$ (a) in the multiple soft scattering limit for different values of the kinematic constraint $R = \omega_c L$ (b) in the single hard scattering limit for different $\bar{R} = \bar{\omega_c} L$ [112].

where the characteristic gluon frequency $\omega_c = \hat{q}L^2/2$ sets the energy scale of the induced radiation. In [112], a kinematic constraint is imposed, requiring that $k_T < \omega$ (the transverse momentum of the radiated gluon cannot exceed its own energy). This condition introduces a dimensionless scale parameter R, that relates the characteristic scales of ω^2 and k_{T}^2, i.e. ω_c^2 and $\hat{q}L$, respectively (the latter from its definition in Eq. 7.2).

$$R = \frac{2\omega_c}{\hat{q}L} = \frac{1}{2}\hat{q}L^3 = \omega_c L \tag{7.4}$$

Similar equations govern the single hard scattering limit:

$$\bar{\omega_c} = \mu^2 L^2/2 \qquad and \qquad \bar{R} = \bar{\omega_c} L \tag{7.5}$$

where μ is the transverse momentum transferred in the single hard scattering.

The spectra of induced gluon radiation are shown in Fig. 7.5 for the two scenarios. Notice that the single hard scattering scenario results in a harder spectrum of gluons than the multiple scattering, but that the gross features are similar. The overall scale of the spectrum is governed by ω_c, while R determines the shape as ω goes to zero. For the limit of $R \to \infty$, which corresponds to an infinitely extended medium, the BDMPS and GLV results are retrieved.

In the infinite energy limit, the average energy loss can be expressed as the integral over the induced radiation spectrum:

$$\langle \Delta E \rangle_{R\to\infty} = \lim_{R\to\infty} \int_0^\infty d\omega\, \omega \frac{dI}{d\omega} \simeq \frac{2\alpha_s C_R}{\pi} \begin{cases} \sqrt{\frac{\omega_c}{2\omega}} & \text{for} \quad \omega < \omega_c \\ \frac{1}{12}\left(\frac{\omega_c}{\omega}\right)^2 & \text{for} \quad \omega \geq \omega_c \end{cases} \tag{7.6}$$

It is clear from Fig. 7.5 that this integral is dominated by the region $\omega < \omega_c$. Integrating Eq. 7.6 up to ω_c gives:

$$\langle \Delta E \rangle_{R\to\infty} \propto \alpha_s C_R \omega_c \propto \alpha_s C_R \hat{q} L^2 \tag{7.7}$$

The quadratic dependence of energy loss on path length is thus retrieved for an infinitely energetic parton traversing a static medium of infinite extent. Note, however, that this is not the general case. In particular, for a rapidly expanding medium, the density ρ (and thus the transport coefficient $\hat{q}$) decreases as $1/L$, making the energy loss linear with path length.

7.2.3 Centrality Dependence of Suppression

At RHIC, the background energy of the underlying event makes direct jet reconstruction difficult. While there have been recent attempts at full jet reconstruction [115], the most effective tools for measuring jet quenching are still high-p_T single-particle spectra and two-particle correlations. To distinguish between various models of parton energy loss, it is useful to vary the geometry of the medium, such that partons must traverse different path lengths.

To this end, the centrality dependence of the nuclear modification factor, R_{AA}, is shown in Fig. 7.6 [63] for different p_T bins in 200 GeV collisions in both the Cu+Cu and Au+Au system. Since the published PHOBOS Au+Au spectra at 200 GeV did not achieve the same statistics that allowed the measurement of the Cu+Cu spectra out to 7 GeV/c, Au+Au results from the PHENIX collaboration are also included for comparison [58].

Within the systematics of the measurement, these data show a simple scaling with the volume of the system (measured either by N_{part} or N_{coll})[5], that is for the same number of participant nucleons, the Cu+Cu and Au+Au spectra are strikingly similar over the broad range of p_T that was measured. This observed scaling has been extended by PHENIX out to $p_T \sim 15$ GeV/c [117]. While the statistics are more limited at $\sqrt{s_{NN}} = 62.4$ GeV, this scaling appears to hold for the lower energy as well (see Fig. 7.7 [63]).

Parton Quenching Model

A number of predictions were made for the Cu+Cu system that had successfully described the centrality dependence of high-p_T charged hadron yields and back-to-back correlations in the Au+Au system. One such model is the Parton Quenching Model (PQM), which uses the BDMPS quenching weights described in Sect. 7.2.2 and a realistic collision geometry to describe parton energy loss [116]. The overall scale of $\hat{q}$ was set by fixing the observed suppression to match the data in central Au+Au collisions. Using this prescription, the model was able to describe the centrality dependence of R_{AA}, as shown in Fig. 7.6. One complication arose in how to treat lower energy partons, to which the calculated quenching weights assigned an increasing probability of losing $\Delta E > E$.

[5]Note that the values of N_{coll} for Cu+Cu and Au+Au collisions with the same N_{part} are indistinguishable (see Fig. 4.4(c) on page 52).

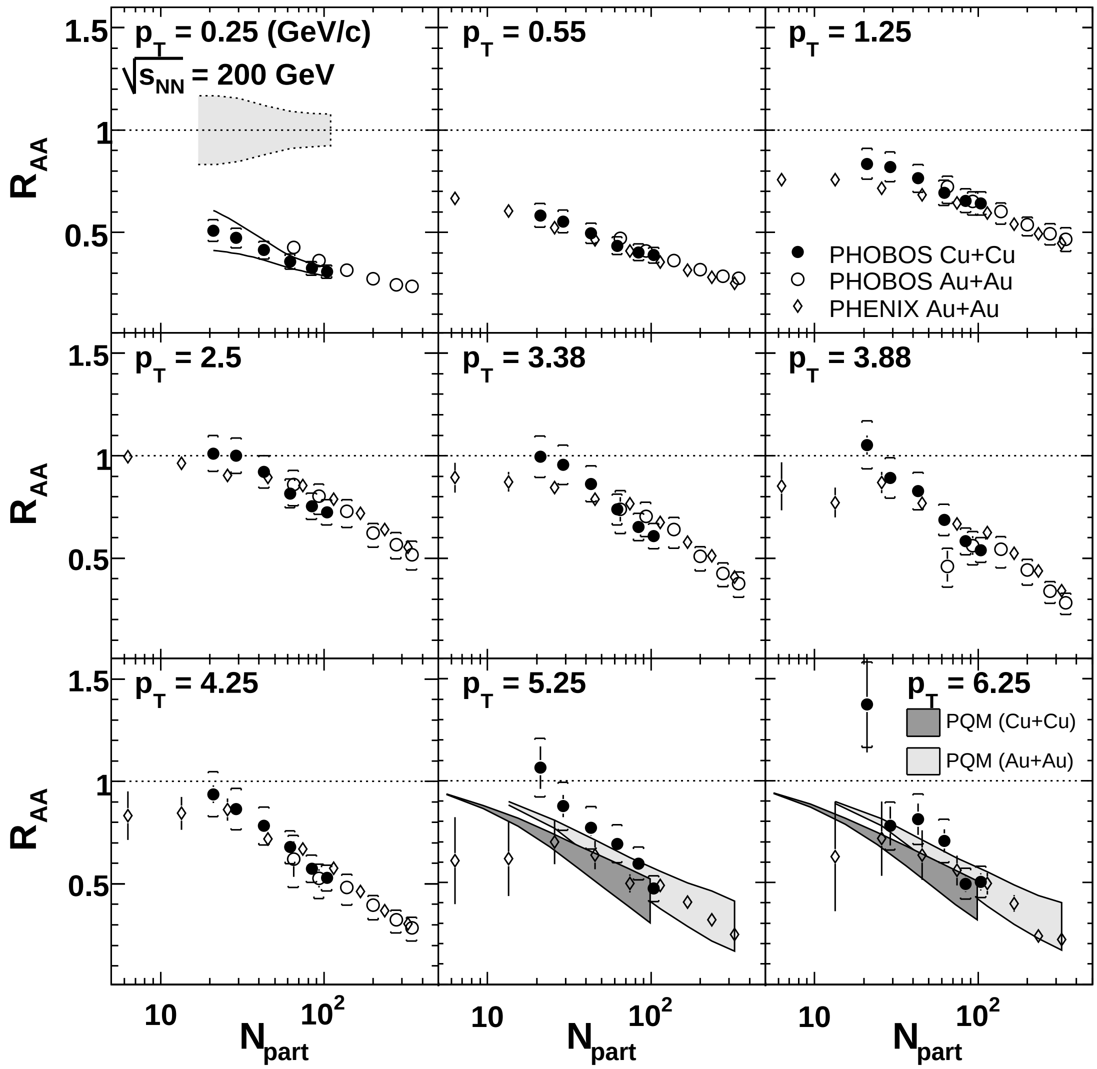

Figure 7.6: The nuclear modification factor, R_{AA}, as a function of the number of participants, $N_{\rm part}$, in bins of transverse momentum, p_T, for Cu+Cu (closed symbols) and Au+Au (open symbols) collisions at $\sqrt{s_{NN}} = 200$ GeV [57, 58]. The gray band in the first frame represents the relative uncertainty on $\langle N_{\rm coll}\rangle$; the solid lines show the effect of this uncertainty on the measured R_{AA}. The bands at high-p_T show the predictions of the PQM model [116].

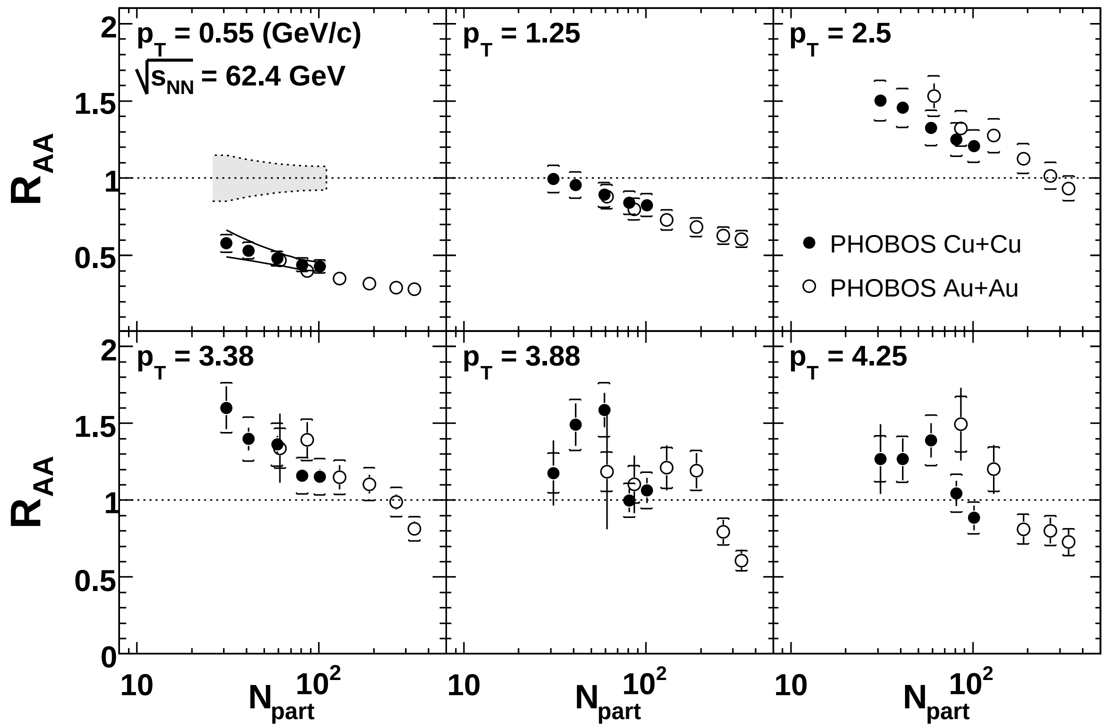

Figure 7.7: The nuclear modification factor, R_{AA}, as a function of the number of participants, N_{part}, in bins of transverse momentum, p_{T}, for Cu+Cu (closed symbols) and Au+Au (open symbols) collisions at $\sqrt{s_{\mathrm{NN}}} = 62.4$ GeV [95].

The different methods for truncating the high-energy tail introduced the major source of uncertainty in the model.

Using the same constant of proportionality between nuclear overlap density and $\hat{q}$ from central Au+Au, a prediction was made for the centrality evolution in Cu+Cu. Our Cu+Cu results in Fig. 7.6 suggest that PQM slightly overestimates the suppression in the smaller system, deviating from the observed N_{part} scaling.

Predictions of N_{part} scaling

There are a number of models that *do* explicitly predict a scaling between systems at the same N_{part}. The simple jet absorption model described in [118] assigns a survival probability to each produced jet, using only two inputs. First, a Glauber-based collision geometry determines the locations of the hard scatterings and the density distribution of the medium in the transverse plane. Then, the probability of jet absorption is treated as quadratic in path length and attenuated by an expanding medium (equivalent to a static medium with linear energy loss).

This prescription is similar to the aforementioned PQM model. However, instead of rigorously employing quenching weights to determine the energy loss, the survival probability of each jet, e^{-KI}, is calculated from the path length density integral I and

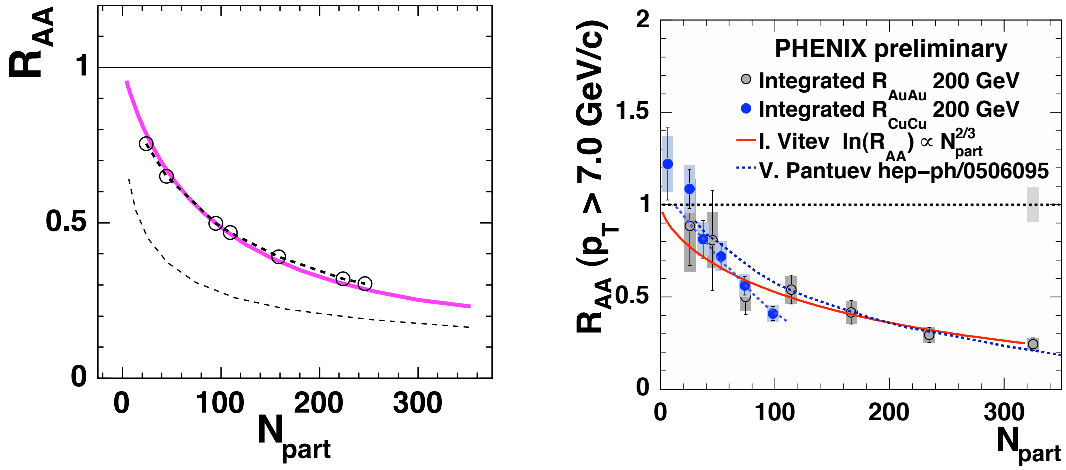

Figure 7.8: (a) Prediction of R_{AA} for central (0-5%) collisions of lighter nuclei (open circles joined by dashed line) compared to the centrality dependence in Au+Au (solid line) [118]. The lower dashed line corresponds to N_{part} scaling. (b) Scaling predicted by I. Vitev [119] and model of corona effect by V. Pantuev [120], with PHENIX Cu+Cu R_{AA} data taken from [117].

a free parameter K, called the absorption coefficient. Assuming the same absorption coefficient for all systems, this model predicted that central collisions of smaller nuclei would exhibit the same suppression as collisions of larger nuclei at the same N_{part} (see Fig. 7.8(a)). This is a simple consequence of geometry; to first order, the volume of the system scales with N_{part}.

The GLV model predicted an explicit scaling between $\ln R_{AA}$ and $N_{\text{part}}^{2/3}$ [119] based on dimensional considerations. The result is readily derived from the expression for fractional energy loss in a (1+1)-dimensional Bjorken expansion, in the limit of large parton energy. This is achieved by simply substituting N_{part} for the gluon density, $N_{\text{part}}^{1/3}$ for the path length, and $N_{\text{part}}^{2/3}$ for transverse area,

7.2.4 Further Observations

The similar high-p_T spectra in Au+Au and Cu+Cu collisions with the same N_{part} can be explained by similar average path lengths (despite the quite different path length distributions). It is not obvious, however, that this similarity ought to persist to such low momentum. As described in Sect. 7.2.1, particle production in heavy-ion collisions is expected to be influenced by many effects. These include p_T-broadening due to initial and final state multiple scattering (the 'Cronin effect'), the medium-induced energy loss of fast partons, and the effects of collective transverse velocity fields as well as parton recombination [63, 100]. Considering the significantly different geometries of Au+Au and Cu+Cu collisions with the same number of participant nucleons, it is not obvious, *a priori*, that these effects should conspire to give similar spectra in both systems over such a large range in p_T. This simple scaling of the hadron yields over a broad range of transverse momentum, as well as a broad range of pseudorapidity [89], appears to be a fundamental feature of heavy ion collisions at these energies. A full explanation of this phenomenon may well present a challenge to theoretical models of particle production.

8 Obtaining Correlated Yields

As discussed in Ch. 5, the PHOBOS experiment is capable of measuring the angular position of charged particles over a very broad acceptance, as well as the momentum information over a more limited region. Both of these components are used in the analysis of p_{T}-triggered correlations over a large range of relative pseudorapidity ($-4 < \Delta\eta < 2$) and over the complete azimuthal angle ($0 < \Delta\phi < 2\pi$). The trigger particles for this analysis are tracks reconstructed in the Spectrometer with transverse momentum, $p_{\mathrm{T}} > 2.5$ GeV/c. Associated particles, whose angular position is measured relative to the trigger, come from merged hits in the Octagon subdetector. Since the Octagon is a single-layer detector, there is no p_{T} selection on the associated particles. All particles escaping the beam pipe enter into the correlation, corresponding to a low-p_{T} cutoff of 4 MeV/c at $\eta = 3$ and 35 MeV/c at $\eta = 0$. Merged hits from the first layers of the Vertex and Spectrometer subdetectors are also used to fill the holes in the Octagon acceptance.

8.1 Constructing the Correlation Function

By design, the angular correlation function measures the increased likelihood that two particles will be found in a particular angular configuration compared to random pairs drawn from the single particle distribution. Typically, such a correlation involves the construction of a signal distribution of same event pairs and a background distribution of pairs mixed from different events. It is of critical importance that the signal and background distributions have similar multiplicity and matching detector acceptance. For this reason, the analysis has been performed in small bins of collision centrality and event vertex (1 mm).

For events that pass the cuts listed in Table 8.1, a 2-D histogram is filled in each centrality bin with the relative pseudorapidity ($\Delta\eta$) and the relative azimuthal angle ($\Delta\phi$) between trigger tracks and merged hits from the Octagon and the first layers of the Vertex and Spectrometer detectors. An example of the signal histogram in one z-vertex bin is shown in Fig. 8.1(a). To have been successfully reconstructed, the trigger track must have left a hit in the first layer of the Spectrometer. This hit is excluded from being paired with the trigger track. Since hit merging can affect adjacent pads, these are excluded as well. The analysis module stores the following information about the trigger track in a tree for later use in event mixing: η^{trig}, ϕ^{trig}, centrality bin, and position of pad hit in first spectrometer layer.

The mixed event background uses the same event selection as the signal events except that there is *no requirement* of a track with $p_T > 2.5$ GeV/c. For each event, a trigger

Event Cuts:	
Trigger Condition	IsCol && NotPrePileup && NotPostPileup
Vertex Range	$-15 < v_z < 10$ cm, using RMSSelVertex
Collision Centrality	Bin 7 ($45-50\%$) through 17 ($0-3\%$), using PR04 PdlMean cuts (Appendix C)
Track Cuts:	
η Range	0 - 1.5
Fit Probability	$\chi^2 > 0.04$
Secondary Rejection	$\lvert dca \rvert < 0.35$ cm
Trigger (signal only)	$p_\mathrm{T} > 2.5$ GeV/c

Table 8.1: A summary of the event cuts and track selection criteria for the triggered correlations analysis.

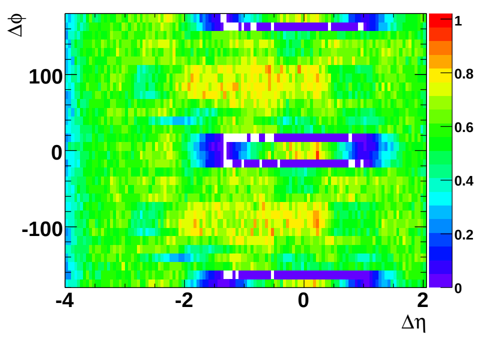

(a) Signal

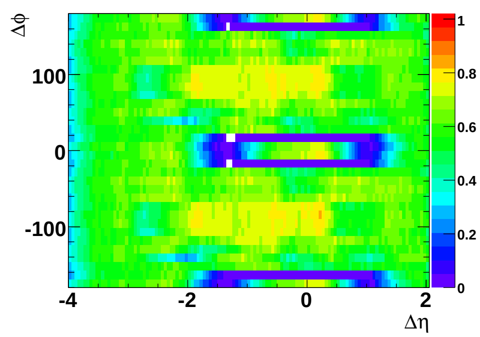

(b) Mixed Event Background

Figure 8.1: (a) Signal and (b) mixed event $\Delta\eta$,$\Delta\phi$ distributions in one vertex bin ($0.3 < v_z < 0.4$ cm) for the 10-15% centrality bin. Distributions are normalized by the number of triggered events.

track is selected randomly from the stored tree making sure that it came from an event with the same centrality and z-vertex bin. The 2-D histogram of the pair distribution is filled as in the signal, again requiring that the track not be paired with a hit in the same pad as its own first hit. The mixed event background histogram is shown for one z-vertex bin in Fig. 8.1(b).

8.1.1 Correlated Yield

The quantity that will be quoted as a final result is the per trigger correlated yield of charged particles as a function of $\Delta\eta$ and $\Delta\phi$. Since the mixed event construction does not preserve the event-wide elliptic flow correlation, the background is first multiplied by this term before being subtracted from the signal.

$$\frac{1}{N_{trig}}\frac{d^2N_{ch}}{d\Delta\phi\, d\Delta\eta} = S(\Delta\phi,\Delta\eta) - B(\Delta\eta)\cdot a(\Delta\eta)\left(1+2V(\Delta\eta)\cos(2\Delta\phi)\right) \tag{8.1}$$

$$= B(\Delta\eta)\cdot\left[\frac{s(\Delta\phi,\Delta\eta)}{b(\Delta\phi,\Delta\eta)} - a(\Delta\eta)\left(1+2V(\Delta\eta)\cos(2\Delta\phi)\right)\right] \tag{8.2}$$

$S(\Delta\phi,\Delta\eta)$ and $B(\Delta\eta)$ correspond to the acceptance corrected *per trigger* signal and background distributions; $a(\Delta\eta)$ is a scale factor very close to unity, which accounts for a slight mismatch in multiplicity between signal and background; and $V(\Delta\eta) = \left\langle v_2^{trig}\right\rangle\left\langle v_2^{assoc}\right\rangle$ is the product of the mean flow magnitudes for trigger and associated particles.

In practice, it is convenient to rearrange the terms of Eq. 8.1 such that the detector acceptance cancels in the ratio of signal and mixed events (the lowercase s and b signifying that the distributions are uncorrected)[1].

8.1.2 Averaging Vertex Bins

The information over the full vertex range is combined by averaging the 250 separate vertex bins. Because the detector acceptance looks quite different for different z-vertex positions, this cannot be achieved by simply adding the histograms and dividing by their number. Naïvely, one might try to combine the results by constructing the error-weighted mean where the error in each bin is just the square root of the number of entries. However, for the ratio of two low-statistics, Poisson-distributed variables, this can be shown to consistently underestimate the true mean value. The preferred solution is the same that was used to average different bending directions in the p_T spectra analysis [93]. The average value of the correlation in a given $\Delta\eta$,$\Delta\phi$ bin becomes

$$\langle\text{Correlation}\rangle = \frac{\sum\limits_{vertex}\text{SignalHits}}{\sum\limits_{vertex}\left(\text{SignalTriggers}\cdot\dfrac{\text{BackgroundHits}}{\text{BackgroundTriggers}}\right)} \tag{8.3}$$

where the sums are over the 250 vertex bins. The relative error on the average correlation is just the square root of the total number of signal hits in a given $\Delta\eta$,$\Delta\phi$ bin.

Figure 8.2 shows the results of performing the correlation analysis (including the averaging over vertex bins) on simulated HIJING events run through a full detector simulation. The method accurately retrieves the known azimuthal correlation that was artificially introduced into the raw simulated events.

When measured in real data events, the dominant feature of the two-particle correlation is a term proportional to $\cos(2\Delta\phi)$, clearly seen in Fig. 8.3, characteristic of elliptic flow. In the following section, the procedure for subtracting the sizeable flow-like correlation to extract the additional jet-like correlation is discussed.

---

[1] Because the signal and background have been carefully constructed in small bins of z-vertex, the same acceptance factor $A(\Delta\phi,\Delta\eta)$ relates the two raw distributions to the true distributions i.e. $s(\Delta\phi,\Delta\eta) = S(\Delta\phi,\Delta\eta)\cdot A(\Delta\phi,\Delta\eta)$ and $b(\Delta\phi,\Delta\eta) = B(\Delta\eta)\cdot A(\Delta\phi,\Delta\eta)$.

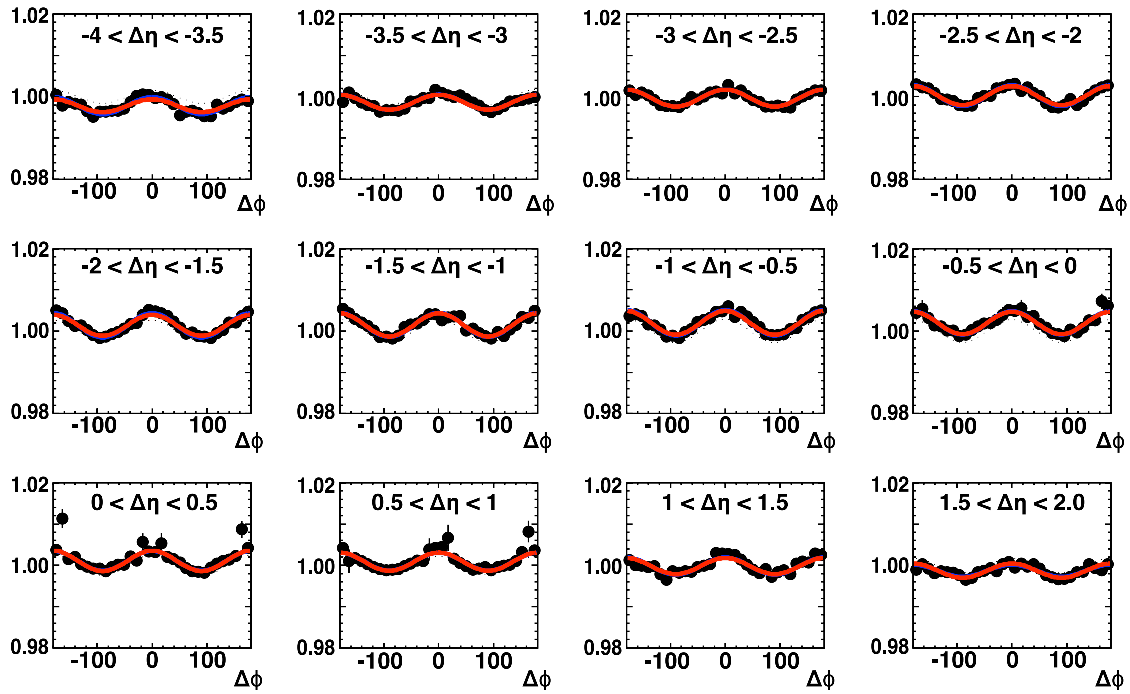

Figure 8.2: $\Delta\phi$ projections of the correlation function averaged over $-10 < v_z < 10$ cm for reconstructed HIJING events ($0-10\%$ central) run through a full detector simulation. The separate panels correspond to 0.5 unit-wide $\Delta\eta$ slices of the reconstructed correlation from -4 to 2. The raw HIJING events have had a flow correlation artificially introduced through the random reassignment of particle ϕ angles based on a $\cos(2\phi)$ modulation with a magnitude of 5% at mid-rapidity falling off linearly to zero at $\eta = 6$. The input correlation (scaled by the occupancy and suppression factors discussed in Sect. 8.2.2 and 8.2.3) is represented by the red lines.

8.2 Subtraction of Elliptic Flow

For Au+Au events at RHIC, elliptic flow introduces a harmonic term into the distribution of single particles proportional to $1 + 2v_2\cos(2(\phi - \Psi_R))$, where Ψ_R is the reaction plane angle[2]. The corresponding harmonic correlation term for pairs of particles is then $1 + 2\left\langle v_2^{trig} v_2^{assoc}\right\rangle \cos(2\Delta\phi)$. This is just a consequence of both the trigger and associated particles being preferentially produced in alignment with the reaction plane. For the purposes of this analysis, $\left\langle v_2^{trig} v_2^{assoc}\right\rangle$ is approximated as $\left\langle v_2^{trig}\right\rangle\left\langle v_2^{assoc}\right\rangle$. This approximation is actually more robust than one might think against fluctuations in v_2, which are known to be relatively large [121]. This is because the event plane method used by PHOBOS to measure flow is actually sensitive to the RMS not the mean [49] of

[2]The reaction plane angle is defined by the orientation of the initially asymmetrical overlap region between colliding nuclei. It points on a line in the transverse plane joining the centers of the two nuclei. Positive v_2 corresponds to preferential production of particles along this line.

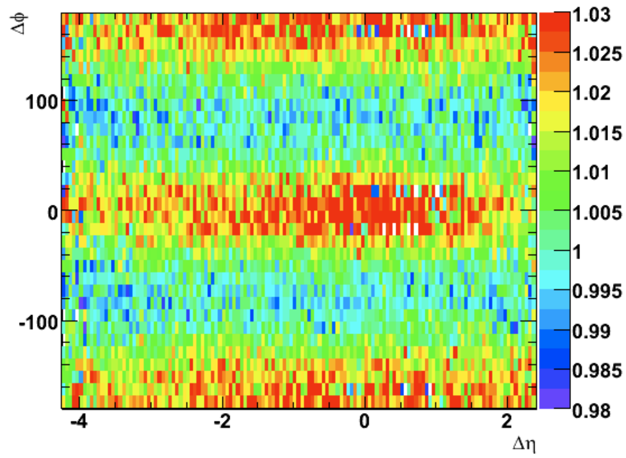

Figure 8.3: $\Delta\eta, \Delta\phi$ correlation averaged over $-15 < v_z < 10$ cm ($15-20\%$ central Au+Au). Note that the peculiar detector acceptance seen in Fig. 8.1 is cancelled in the ratio of signal to mixed events. Additionally, the various holes around the Spectrometer and Vertex layers are largely filled by averaging over different vertex positions.

v_2. In a situation where fluctuations were driven by event-by-event shape differences in the initial source, v_2^{trig} and v_2^{assoc} should fluctuate together, making the above approximation an exact equality.

8.2.1 Fits to Published Elliptic Flow Measurements

It is clear from Eq. 8.1, that one needs to know the mean v_2 of the trigger and associated particles to extract the correlated jet yield. To determine the value of v_2 at arbitrary values of N_{part}, p_{T} and η, it is assumed that v_2 can be factorized into three functions, each depending on a single variable. The validity of this assumption is demonstrated in Fig. 8.5 and 8.6. The v_2 estimates were derived from fits to published PHOBOS measurements, which used the event plane procedure described in [90, 122].

Beginning with the N_{part} dependence of the track-based and hit-based PHOBOS v_2 results [50], a third order polynomial fit is found to effectively describe the data over the centrality range of this analysis. A comparison of the fit function to the data can be found in Fig. 8.4.

The next step is to find the functional form of $v_2(p_T)$. The published results only show $v_2(p_T)$ for one minimum bias bin and for a somewhat limited range in p_T. However, a preliminary analysis of the much higher statistics 2004 data set allows the division into multiple centrality bins. In Fig. 8.5, these preliminary results are plotted after being scaled to the minimum bias value of $N_{part} = 236$ using the already described polynomial fit to $v_2(N_{part})$. Indeed, v_2 does appear to factorize nicely between these two variables, an observation previously shown by PHENIX [123]. Because the $v_2(p_T)$ results are only needed for the trigger particle, the fit is optimized in the region

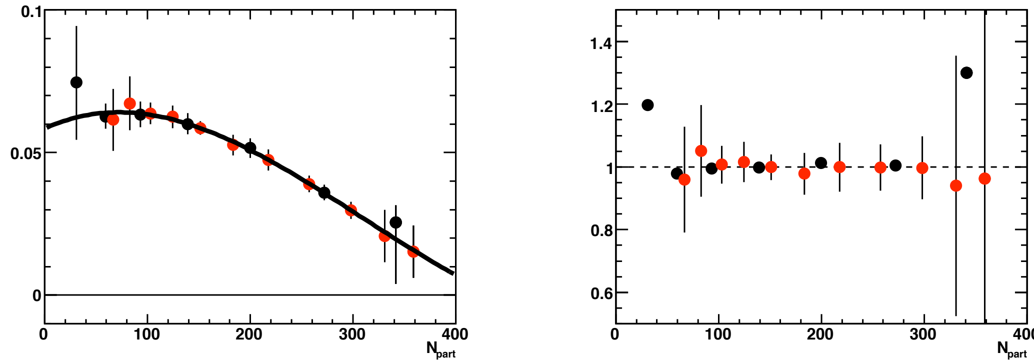

Figure 8.4: $v_2(N_{part})$ from track- (red) and hit-based (black) analyses. Errors are statistical plus systematic. Black line is a 3rd-order polynomial fit to both data sets. On the right the data points have been divided by the fit. Note that the N_{part} range of this analysis is the same as the track-based v_2 analysis.

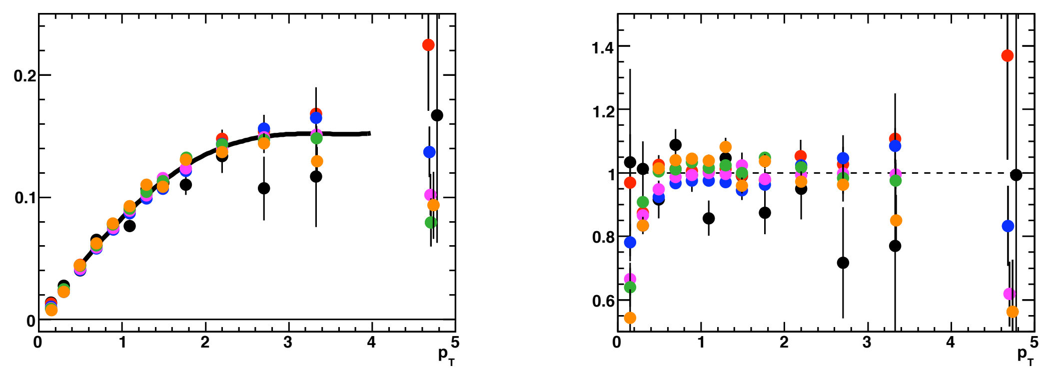

Figure 8.5: $v_2(p_T)$ divided by $v_2(N_{part})/v_2(N_{part} = 236)$. Errors are statistical only. 3-6% (black), 6-10% (red), 10-20% (blue), 20-30% (magenta), 30-40% (green), 40-50% (orange). The fit is a fourth-order polynomial with zero constant term. On the right the points are divided by the fit.

of $\left\langle p_{\mathrm{T}}^{trig} \right\rangle \approx 3$ GeV/c.

Finally, a fit to $v_2(\eta)$ is needed. The published results are shown for three centralities (3-15%, 15-25% and 25-50%). The hit-based results span a broader η range than is used in this analysis. There are also track-based results within the narrower Spectrometer range ($0 < \eta < 1.5$). In Fig. 8.6, the published $v_2(\eta)$ results are shown after scaling to the mid-central points at $N_{part} = 200$. The coefficients of the three polynomial fit functions are listed in Appendix D.

Before constructing the v_2 correlation, however, one must account for the fact that the observed magnitude of the correlation is reduced from the true value by two effects. First, v_2^{trig} is reduced because more tracks are lost due to occupancy in-plane than out-of-plane. Second, v_2^{assoc} is reduced because of secondary hits that are uncorrelated (or at least less correlated) to the reaction plane than true primary tracks.

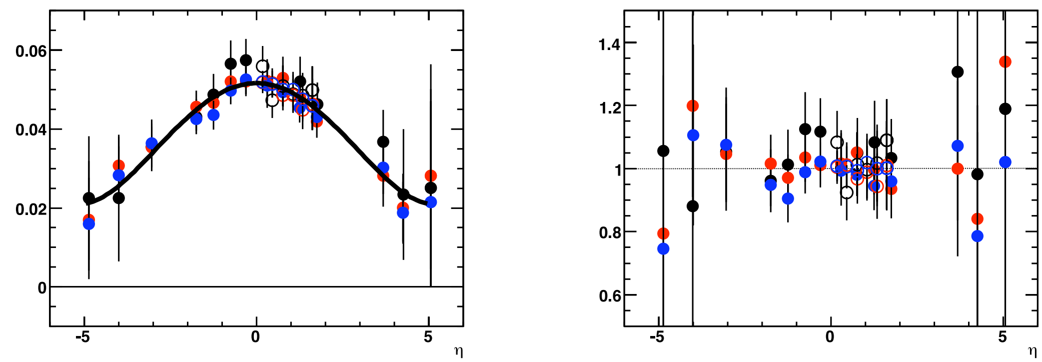

Figure 8.6: $v_2(\eta)$ divided by $v_2(N_{part})/v_2(N_{part}=200)$ for published track- (open circles) and hit-based (closed circles) results. 3-15% (black), 15-25% (red), 35-50% (blue). The fit is an even, fourth-order polynomial. Ratio of data to fit shown in right panel.

8.2.2 Effect of Spectrometer Occupancy on Flow

To estimate the occupancy effect on v_2^{trig}, the parameterization of the occupancy factor with Spectrometer hit density is taken from Sect. 6.3.4, where studies of embedded tracks in real data events determined the fraction of tracks that are lost due to occupancy (see Fig. 8.7(a)). Then, a toy MC generates a ϕ-distribution of tracks with the assigned input flow magnitude. Using the known occupancy factor to randomly discard the appropriate fraction of these tracks based on the local occupancy, it is possible to estimate by how much the observed v_2 of trigger tracks will be diminished from the true value. The magnitude of this effect is shown in Fig. 8.7(b) as a function of multiplicity with the corresponding fit.

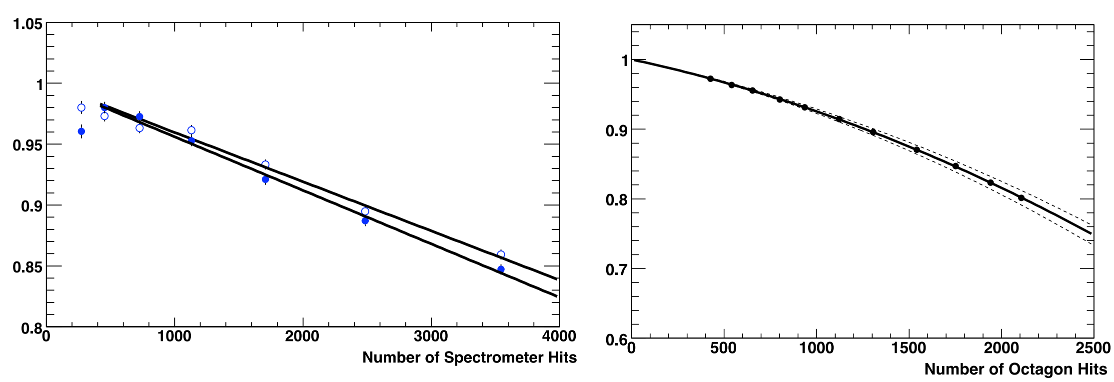

(a) Spectrometer Track Occupancy Factor

(b) Occupancy Effect on v_2^{trig}

Figure 8.7: (a) The fraction of tracks lost to occupancy in the Spectrometer as a function of multiplicity in Au+Au for different bending directions (open and closed symbols). (b) The factor by which occupancy in the Spectrometer diminishes the observed v_2^{trig}. The dashed lines correspond to the uncertainty on this effect.

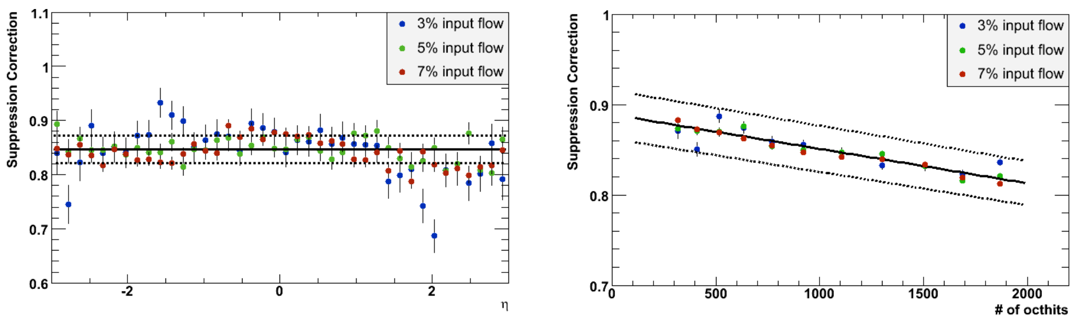

(a) Suppression Correction (b) Centrality Dependent Correction

Figure 8.8: Left: The suppression factor for Octagon hits as a function of η for 3%, 5% and 7% flow in centrality bin 13. Right: The suppression factor as a function of multiplicity, read-off as a constant from the previous panel.

8.2.3 Suppression Correction

To account for the effect of non-primary hits, a sample of HIJING events with known input flow strength is run through the full detector simulation and reconstruction. The output flow (i.e. the magnitude of the $\cos(2\Delta\phi)$ fit to the distribution of reconstructed hit angles compared to the known HIJING reaction plane angle) is compared to the input flow. The ratio of output to input is shown for the Octagon subdetector in Fig. 8.8(a) as a function of η for different values of input flow strength. This ratio, known as the suppression correction, is extracted as a constant in η and is shown in Fig. 8.8(b) as a function of multiplicity.

Studies have shown that non-flow correlations are suppressed by the same amount as flow due to uncorrelated secondary hits. For this reason, after the v_2 subtraction has been performed, the remaining correlation is scaled up by the same suppression factor.

8.2.4 Average Flow Correlation

To compare the average correlation function in data to the estimated flow correlation, the factorized fit function is used to fill a histogram as a function of $\Delta\eta$ and $\Delta\phi$ with the harmonic term of Eq. 8.2 on page 95. The magnitude of v_2^{trig} is calculated using the $\langle p_T \rangle$ and $\langle \eta \rangle$ of trigger tracks in the particular z-vertex bin in question. These values are shown as a function of z-vertex in Fig. 8.9(a). The $\langle p_T \rangle$ is essentially independent of vertex position with a value of ≈ 2.95, whereas the $\langle \eta \rangle$ depends strongly on vertex position, ranging from around 1.2 for the most negative positions to around 0.3 for the most positive[3].

In principle, the flow correlation histograms constructed in this way could be compared at each z-vertex position to the correlation function in the data. However, due the

[3]The gaps in the acceptance of trigger tracks coincide with the particular value of η where the track moves from the central region of the spectrometer to the outer wing, see Sect. 5.2

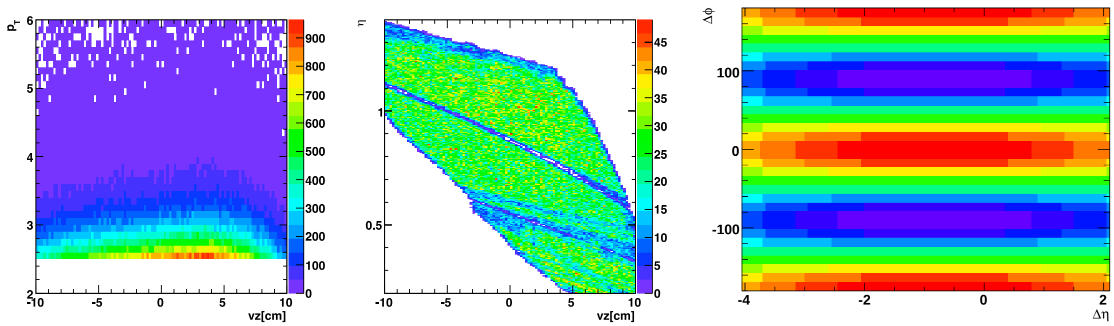

(a) Trigger track p_{T} and η distributions

(b) Vertex averaged flow correlation

Figure 8.9: (a) Trigger track p_T and η distributions as a function of z-vertex position. (b) $\Delta\eta, \Delta\phi$ correlation from the estimate of $v_2(N_{part}, \eta, p_T)$ averaged over all vertex bins and over centrality bins 11 through 13. Notice that the peak of the distribution is somewhat displaced to the negative $\Delta\eta$ since the $\langle\eta\rangle$ of trigger tracks is somewhat forward.

meager statistics in each vertex bin of data this is not a useful comparison, particularly as one would like to estimate the constant scale factor, $a(\Delta\eta)$, by comparing these two distributions. Instead, the flow correlation is first averaged over the full range of vertex bins (see Fig. 8.9(b)) and then compared to the averaged correlation function shown in Fig. 8.3.

8.2.5 Scale Factor

The value of the scale factor, $a(\Delta\eta)$ in Eq. 8.2, was calculated using two methods: Zero Yield at Minimum (ZYAM) [124] and Zero Yield at One (ZYA1) [67]. The ZYAM method hypothesizes that the correlated yield in $\Delta\phi$ is equal to zero at some value (i.e. there exists a point where the flow term just equals the measured correlation). In practice, the scale factor is calculated in each centrality bin as a function of $\Delta\eta$ by constructing the vertex average of the quantity

$$\frac{s(\Delta\phi)}{b(\Delta\phi)\cdot[1+2V\cos(2\Delta\phi)]} \tag{8.4}$$

and extracting the minimum value with a parabolic fit in the region $20 < \Delta\phi < 90$ degrees (see Fig. 8.10). Though the scale factor is easier to extract in the ZYA1 method, which simply fixes the yield to be zero at $0.8 < \Delta\phi < 1.2$ radians, it is not guaranteed that the actual minimum occurs here. The more general ZYAM method is used for the mean result; a comparison to ZYA1 determines the magnitude of the systematic uncertainty introduced in finding the scale factor.

Finally, to smooth out statistical fluctuations and allow the interpolation in $\Delta\eta$ between the centers of the twelve $\Delta\eta$ slices, the extracted ZYAM scale factor is fit with a second-order polynomial in $\Delta\eta$. The scale factor is essentially flat for the the most cen-

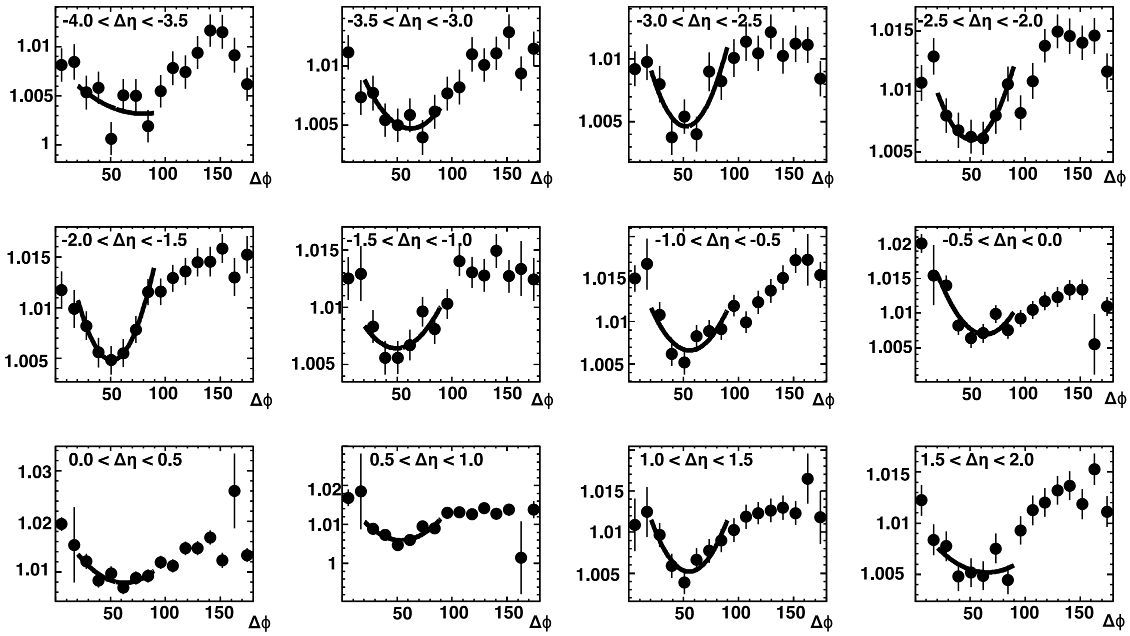

Figure 8.10: To determine the scale factor $a(\Delta\eta)$ in Eq. 8.2, the ratio of the raw correlation to the flow modulation (see Eq. 8.4) is fitted with a second-order polynomial in twelve slices from $-4 < \Delta\eta < 2$ (shown for the 15-20% centrality bin). The location of the minimum is not fixed in the ZYAM method; the value at the minimum corresponds to the scale factor $a(\Delta\eta)$.

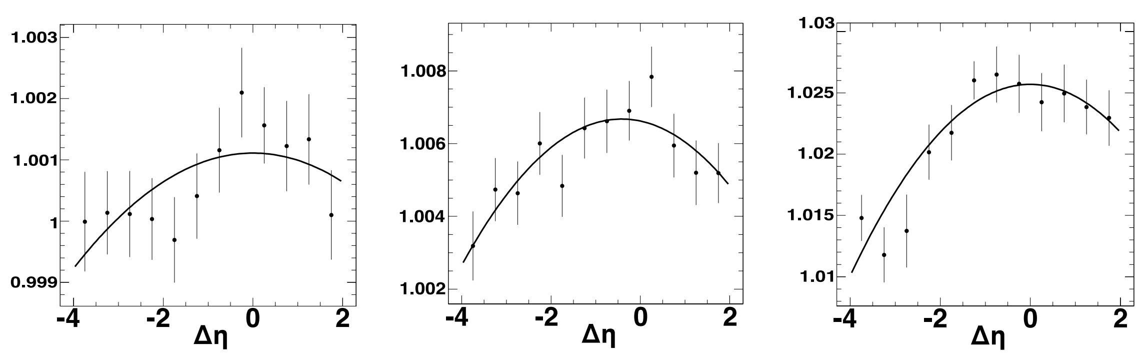

(a) 0-3% (b) 15-20% (c) 40-45%

Figure 8.11: A smooth function is fit to the extracted ZYAM scale factors versus $\Delta\eta$ from $-4 < \Delta\eta < 2$ in three bins of centrality.

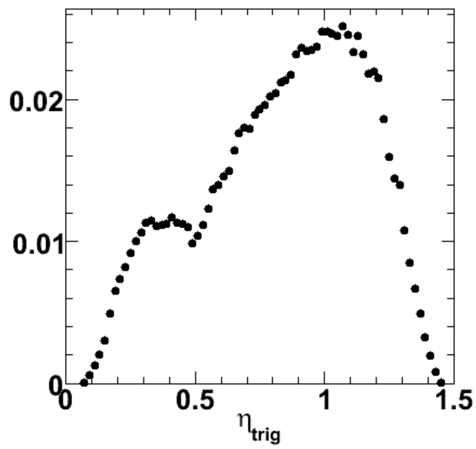

(a) Normalized trigger track distribution

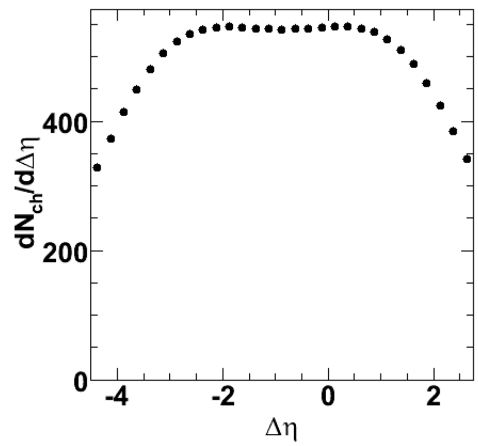

(b) Corrected mixed-event pair distribution

Figure 8.12: Convoluting the normalized trigger distribution with the published $dN/d\eta$ results (not shown) gives the corrected mixed-event pair distribution.

tral bin, growing increasingly peaked at $\Delta\eta = 0$ for more peripheral bins (see Fig. 8.11). This appears to be consistent with the $\Delta\eta$ correlation structure observed in the inclusive two-particle correlations [125], the main difference being that the size of the structure goes as 1/N due to the differently constructed correlation functions.

8.3 Overall Normalization

There is one remaining term in Eq. 8.2 on page 95 that has yet to be discussed, namely the overall normalization, $B(\Delta\eta)$. Multiplying by the per-trigger, acceptance-corrected, mixed-event distribution turns the v_2-subtracted correlation function into the *total yield* of correlated particles. Assuming that the acceptance of pairs is just the product of the single particle acceptances, the trigger acceptance cancels when the distribution is normalized by the number of triggers. The only corrections required are for the associated particles (e.g. acceptance, efficiency, secondaries).

The corrected distribution of associated particles is measured very nicely in the published $dN/d\eta$ measurements [126]. Generating the corrected background distribution (Fig. 8.12(b)) is just a matter of convoluting the published measurements with the normalized η distribution of trigger tracks (Fig. 8.12(a)).

One important feature of this normalization method is that it effectively corrects for pair acceptance as well as single particle acceptance. Consider a region near the edge of the two-particle acceptance at $\Delta\eta = -4$. This could come from a trigger/associated pair at $(\eta_1, \eta_2) = (1, -3)$ or at $(0.2, -3.8)$. However, the associated particle in the second pair falls outside the Octagon acceptance. If the corrected background distribution, $B(\Delta\eta)$, was constructed using the limits of the Octagon acceptance, it would underestimate the

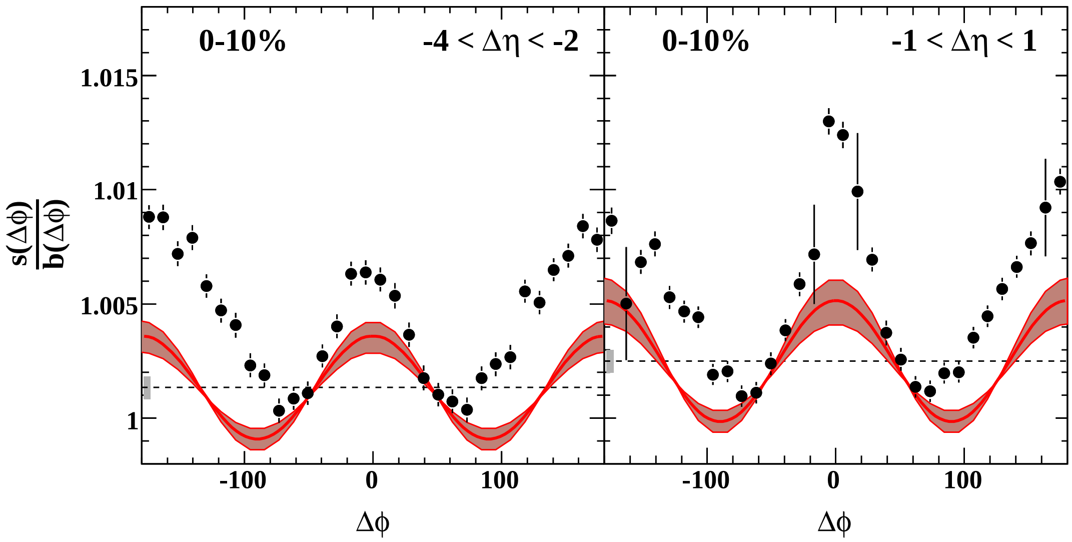

Figure 8.13: Ratio of signal to background for the 10% most central collisions at long-range (left) and short-range (right). Estimated flow modulation and uncertainty are represented by the red line and shaded band. The scale factor, $a(\Delta\eta)$, and its associated uncertainty are represented as a dashed line and a gray box, respectively.

strength of the correlation near the edges of the two-particle acceptance. By using the published results, which include the Ring subdetectors out to $|\eta| < 6$, this problem is avoided.

8.4 Systematic Errors

The dominant systematic error in this analysis comes from the uncertainty in estimating the magnitude of $\left\langle v_2^{trig} \right\rangle \left\langle v_2^{assoc} \right\rangle$. This flow uncertainty is typically on the order of 15-20%, though in central collisions, where the subtracted flow is quite small compared to the resulting jet correlation, the uncertainty reaches 50%. In Fig. 8.13, the relative sizes of the raw correlation, the flow correlation and the flow error are shown for 0-10% central Au+Au at both short-range and long-range. As can be seen in Fig. 9.3 on page 108, these errors translate to roughly a 30% uncertainty on the measured magnitude of the ridge correlation.

Additional systematic uncertainty is introduced from the error on the assignment of the scale factor from the ZYAM procedure described in Sect. 8.2.5. This error is determined from the errors on the minimum values from the ZYAM fits (see Fig. 8.10), as well as a comparison of different assumptions (ZYA1 versus ZYAM). The value of the uncertainty on the per-trigger correlated yield per unit $\Delta\eta$ and $\Delta\phi$ is a constant ± 0.025.

9 Triggered Correlation Results and Discussion

As with the single-particle spectra, it is informative to compare correlations in Au+Au collisions to the more elementary p+p collision system. The choice of p+p reference and the p+p correlation structure are discussed in Sect. 9.1.

After subtracting elliptic flow and averaging over the full vertex range, the per-trigger correlated yields in Au+Au are presented in Sect. 9.2 as a function of pseudorapidity ($\Delta\eta$) and azimuthal angle ($\Delta\phi$) relative to the trigger. The results have been measured for the top half of the Au+Au cross-section and were divided into five centrality bins (0-10%, 10-20%, 20-30%, 30-40% and 40-50%). The essential new feature of this measurement – extending correlated yields out to $\Delta\eta = 4$ – is made possible by the broad pseudorapidity acceptance of the PHOBOS multiplicity array. These data, which were presented in preliminary form at the 2008 Quark Matter conference [127], are being prepared for publication at the time of writing, but should still be considered preliminary.

Besides the triggered correlations measurement described in this thesis, there exist a number of related measurements relevant to this topic. The experimental properties of Au+Au correlations in general and the 'ridge' structure in particular are discussed in Sect. 9.3.

Finally, a summary of proposed theoretical interpretations for the observed Au+Au correlation structure is contained in Sect. 9.4. Particular attention will be paid to whether this new PHOBOS measurement at large $\Delta\eta$ either rules out or supports any of these proposed mechanisms.

9.1 p+p Reference

To understand the effect of the hot, dense medium on correlated particle production in heavy ion collisions, it is essential to compare the correlation in Au+Au to an elementary reference system – p+p collisions. However, due to low statistics, this analysis could not be repeated using PHOBOS p+p data[1]. Instead, 5 million MC events generated by PYTHIA version 6.325 [97] were used as a reference.

To test the validity of this substitution, the magnitude of the correlated yield in PYTHIA was compared to published STAR p+p results at mid-rapidity [67], using the

[1] While PHOBOS has recorded approximately 100 million p+p events to tape, many are either outside the nominal vertex range or fail the IsCol criteria. Additionally, the small angular acceptance of the Spectrometer reduces the number of high-p_T trigger tracks by a factor of 50-100 compared to a similar number of generated MC events.

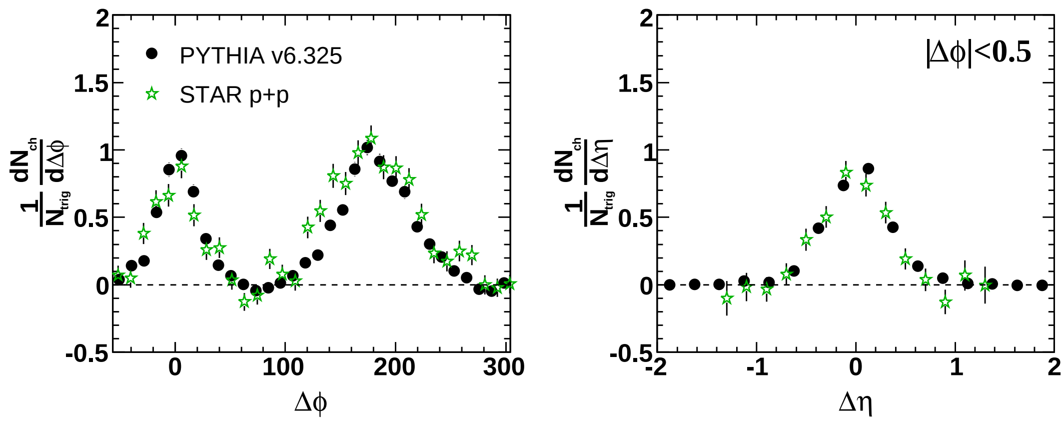

Figure 9.1: Correlations in PYTHIA p+p compared to published STAR results [67] with trigger p_T of 4-6 GeV/c, associated p_T of 0.15-4 GeV/c, and $|\eta| < 1$. Correlated yield is shown versus $\Delta\phi$ (left) and versus $\Delta\eta$ (right) for $|\Delta\phi| < 0.5$.

same triggered and associated selection criteria. Figure 9.1 shows PYTHIA to be in good agreement with the STAR results, as a function of both $\Delta\eta$ and $\Delta\phi$.

While the trigger of $p_{\mathrm{T}} > 4$ GeV/c is slightly higher than the trigger used in this Au+Au analysis ($p_{\mathrm{T}} > 2.5$ GeV/c), the very good agreement between STAR and PYTHIA inspires confidence in this choice of reference. It should be noted that, for this study only, the ZYA1 method (see Sect. 8.2.5) was used to normalize the PYTHIA correlation to match the choice made in this STAR publication.

For comparison with the Au+Au results presented in this thesis, the correlated yield in raw PYTHIA was calculated by subtracting the per-trigger background distribution from the per-trigger signal distribution using the ZYAM method for normalization. The resulting 2-D correlated yield is shown in Fig. 9.2(a) as a function of $\Delta\eta$ and $\Delta\phi$.

There are two prominent features of the high-p_{T} triggered p+p correlation structure. The narrow peak centered at $\Delta\phi \approx \Delta\eta \approx 0$ is a consequence of jet fragmentation. The hadronization of a scattered parton results in a narrow cone of particles associated with the leading hadron that is the trigger. The structure at $\Delta\phi \approx \pi$ comes from particles in the away-side jet correlated with the near-side jet. The away-side correlation is similarly narrow in $\Delta\phi$ but extended in $\Delta\eta$. The broad $\Delta\eta$ extent of the away-side can be understood by considering hard scatterings between partons with very different fractions of the total momentum of the colliding protons.

9.2 Correlations in Au+Au

In central Au+Au collisions, particle production correlated with a high-p_{T} trigger is strongly modified. Figure 9.2(b) shows the conditional yield of charged hadrons relative to a trigger with $p_{\mathrm{T}} > 2.5$ GeV/c. Not only is the away-side yield much broader in

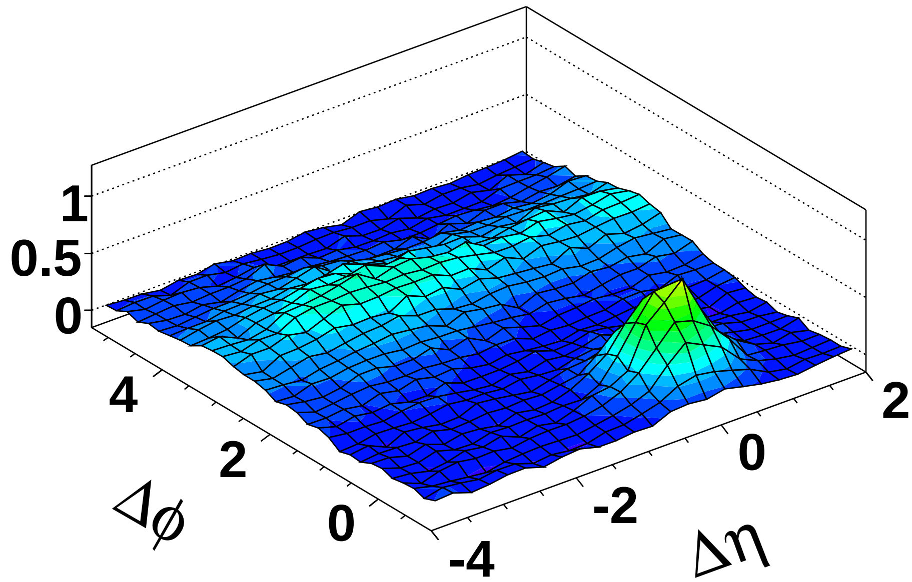

(a) p+p PYTHIA

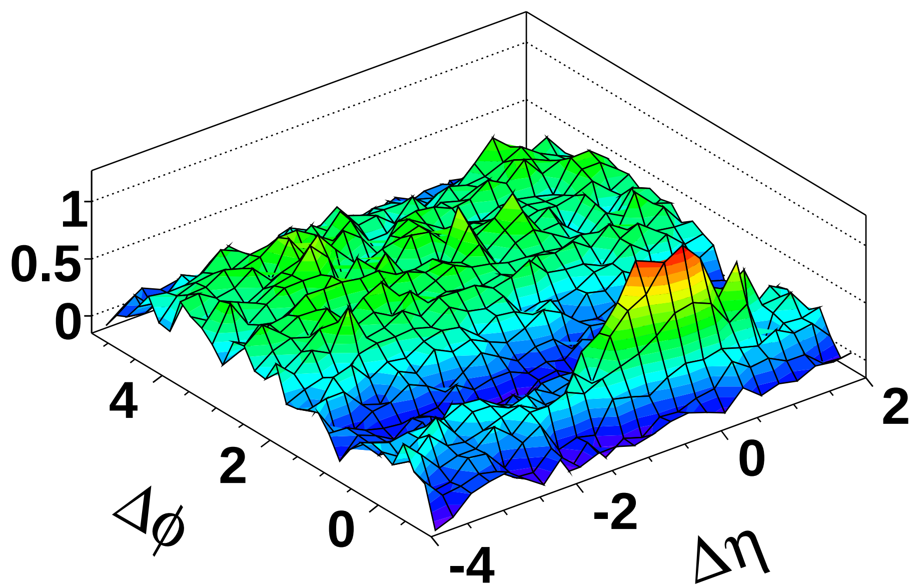

(b) Au+Au 0-30% (PHOBOS)

Figure 9.2: 2-D correlated yield as a function of $\Delta\eta$ and $\Delta\phi$ for (a) 200 GeV PYTHIA p+p and (b) 0-30% central Au+Au. The same cuts are used for PYTHIA as in the Au+Au data ($p_T^{trig} > 2.5$ GeV/c).

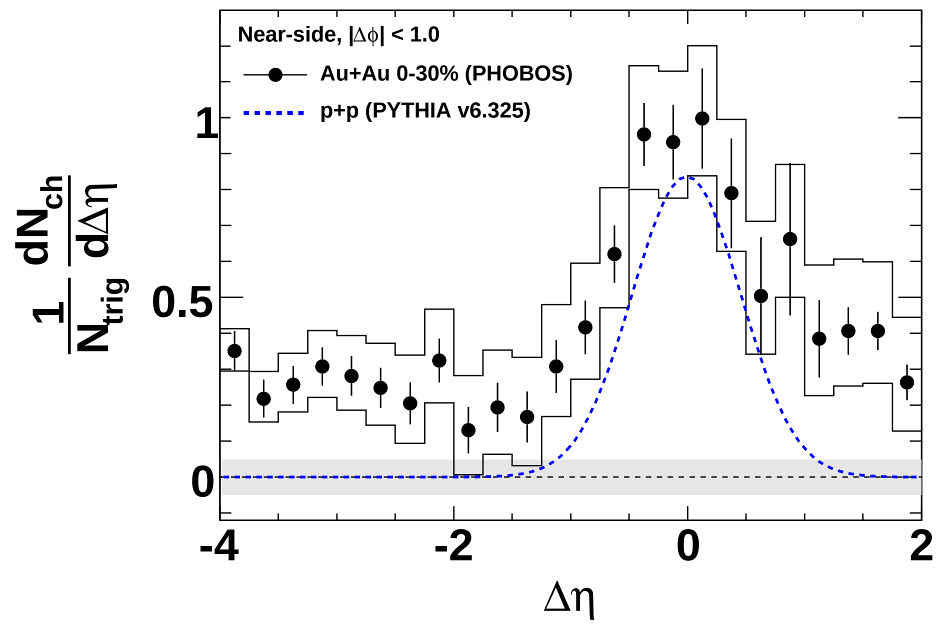

Figure 9.3: Near-side yield integrated over $|\Delta\phi| < 1$ for 0-30% Au+Au compared to PYTHIA p+p (dashed blue line) as a function of $\Delta\eta$.

$\Delta\phi$ than in the p+p system, the near-side peak now sits atop an unmistakable ridge of correlated partners extending continuously and undiminished all the way to $\Delta\eta = 4$.

To examine the near-side structure more closely, the correlated yield is integrated over the region $|\Delta\phi| < 1$ and plotted as a function of $\Delta\eta$ in Fig. 9.3. For the most central 30% of Au+Au collisions, there is a significant and relatively flat correlated yield of about 0.25 particles per unit pseudorapidity far from the trigger. Previously observed by the STAR experiment over a more limited $\Delta\eta$ range [64], the ridge correlation is clearly a novel feature of the system produced in the collision of heavy ions, given its absence from the p+p correlation structure.

A more detailed examination of the correlation structure is possible by projecting the correlation onto the $\Delta\phi$ axis as in Fig. 9.4. In the top row of that figure, the correlated yield in Au+Au is compared for three centrality bins (0-10%, 20-30%, and 40-50%) to PYTHIA-simulated p+p events at short-range (i.e. integrated over the region $|\Delta\eta| < 1$). In the bottom row, the same comparison is shown at long-range (i.e. integrated over the region $-4 < \Delta\eta < -2$).

Focusing first on the away-side correlation, a number of features become apparent. First, the shape of the correlation is considerably broader in $\Delta\phi$ for Au+Au collisions compared to p+p in all measured centrality bins. Additionally, the magnitude of the away-side yield is enhanced relative to p+p, increasingly so for more central Au+Au collisions. Finally, within the systematics associated with the v_2 subtraction, the away-side correlation seems to have a similar shape and centrality dependence at both short- and long-range. This last observation is explored more quantitatively in Fig. 9.5, where

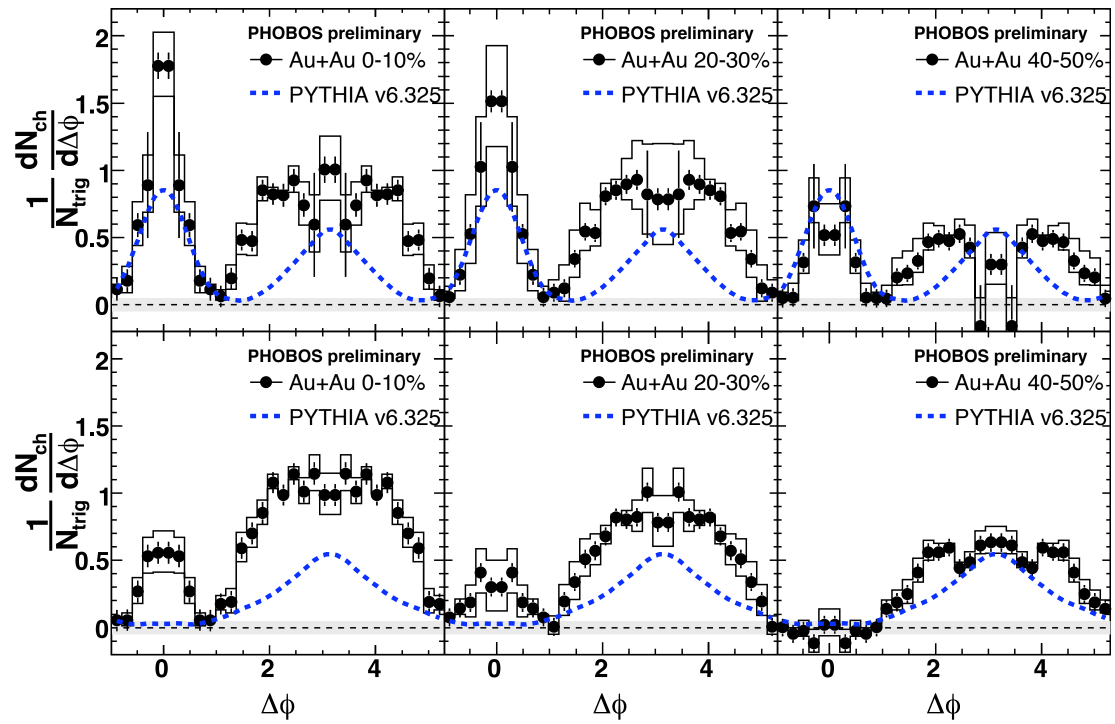

Figure 9.4: Projections of the correlated yield versus $\Delta\phi$ at short-range (top row, $|\Delta\eta|<1$) and long-range (bottom row, $-4 < \Delta\eta < -2$) for three centrality bins (most central on left). The points with very poor statistics in the top row correspond to the $\Delta\phi$ locations of the Spectrometer holes (see Fig. 8.1 on page 94). Dashed, blue line is p+p PYTHIA for comparison. Black boxes represent the uncertainty from flow subtraction. The error on the ZYAM procedure is shown as a gray band at zero.

integrated away-side yields ($\Delta\phi > 1$) are presented as a function of participating nucleons (N_{part}) at short- and long-range (open and filled squares respectively).

Moving to the near-side, an equally rich picture emerges. At short-range (top row of Fig. 9.4), a narrow peak at $\Delta\phi \approx 0$ is observed. In central collisions, this peak has a large contribution in excess of the p+p jet yield. The near-side, short-range correlation decreases in magnitude with decreasing centrality, reaching the same height as p+p in the 40-50% bin.

At long-range (bottom row of Fig. 9.4), the persistence of the ridge correlation to very large $\Delta\eta$ is evident in the peak at $\Delta\phi \approx 0$ for central Au+Au collisions. This effect is completely absent in more elementary systems. The ridge yield also decreases in magnitude for more peripheral collisions until it disappears in the 40-50% bin.

The similar centrality dependence of the short- and long-range yields in excess of the p+p jet correlation suggests a decomposition of the near-side correlation into distinct jet and ridge components. The separation into two components is supported by previous STAR measurements of the associated particle p_T spectra, the centrality inde-

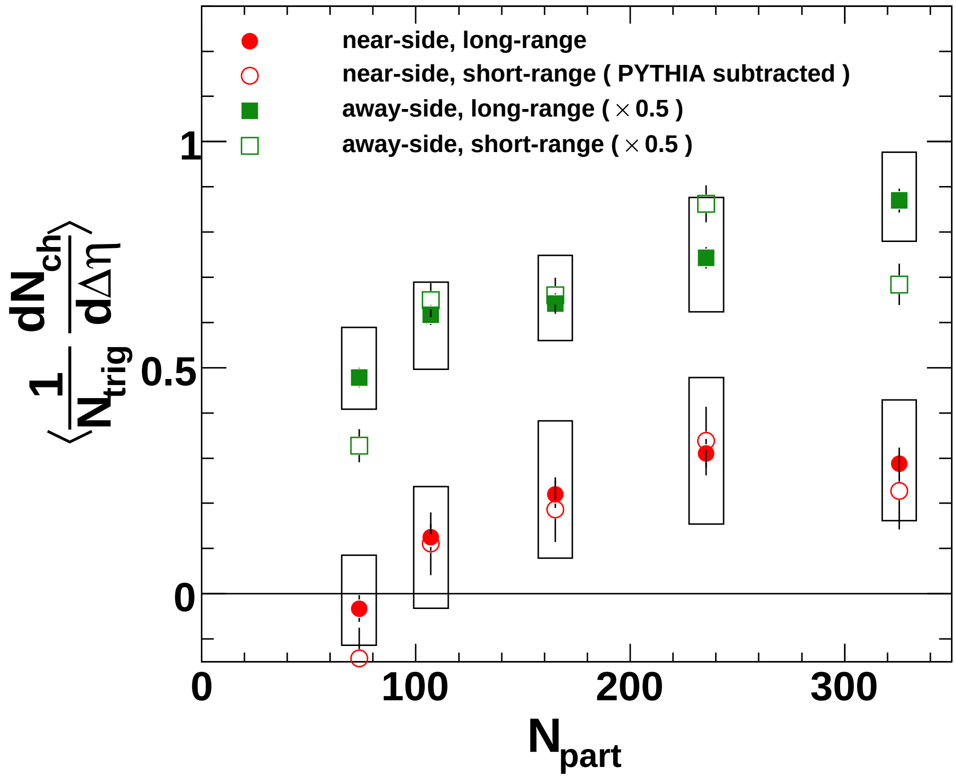

Figure 9.5: Average near-side ridge yields ($|\Delta\phi| < 1$) and away-side yields ($\Delta\phi > 1$) as a function of N_{part} at both short-range ($|\Delta\eta| < 1$) and long-range ($-4 < \Delta\eta < -2$) for the top 50% of the total inelastic cross-section. The away-side yields have been scaled down by a factor of 2. To extract the ridge component of the near-side yield at short-range, the PYTHIA jet yield has been subtracted. Boxes correspond to the combined v_2 and ZYAM systematic errors.

pendence of the jet-like yield, and the ridge-subtracted fragmentation function [64] (for more details see Sect. 9.3). In Fig. 9.5, the integrated ridge yield at long-range (filled circles) is compared to the short-range yield minus the corresponding PYTHIA yield (open circles).

After subtracting the near-side PYTHIA yield, the ridge yield is the same within experimental uncertainties at all $\Delta\eta$. It decreases as one goes towards more peripheral collisions and is consistent with zero in the most peripheral bin analyzed (40-50%). While the systematic errors do not completely exclude a smooth disappearance of the ridge as one approaches p+p collisions, these data suggest the ridge may have already disappeared by $N_{\text{part}} = 80$.

A summary of the main findings of this analysis of high-p_{T} triggered two-particle correlations is listed below:

- A broadened away-side correlation persists over the full pseudorapidity range.
- For central Au+Au collisions, the near-side ridge continues to at least $\Delta\eta = 4$.

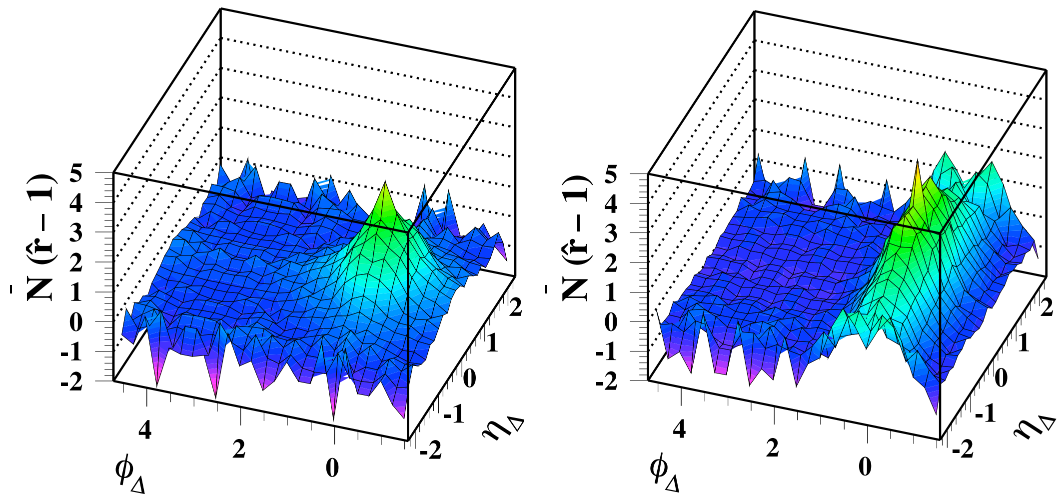

(a) 40-70%

(b) 0-5%

Figure 9.6: Charge-independent autocorrelations in $\Delta\eta$,$\Delta\phi$ after subtraction of dipole and quadrupole terms in $\Delta\phi$ [128]. Notice the much broader 'minijet' peak in the more central collisions.

- The ridge yield decreases for more peripheral collisions; it is consistent with zero at $N_{\text{part}} \approx 80$.

- For all centralities, the ridge yield is the same at small and large $\Delta\eta$ after subtracting a jet-like component taken from p+p PYTHIA.

Precise, quantitative measurements of correlations between particles can shed light on the evolution of the system produced in heavy ion collisions and the underlying mechanisms responsible for particle production. This analysis adds a very important piece to the puzzle, namely the longitudinal extent of the ridge correlation. However, there are many other known features of correlated particle production, and any serious theoretical description ought to simultaneously account for these various features. Therefore, a brief description of related correlation measurements is included first, before addressing the numerous theoretical interpretations.

9.3 Experimental Properties of the Ridge

A near-side correlation structure elongated in $\Delta\eta$ was first observed by STAR in the study of charge-independent autocorrelations at $\sqrt{s_{\text{NN}}} = 130$ GeV [128]. The properties of this elongated structure have since been extensively studied through both autocorrelations and triggered correlations near mid-rapidity. This includes varying the trigger and associated p_{T} requirements, using identified trigger particles, and selecting on the relative position of the trigger to the reaction plane angle. In addition, correlations have been measured for associated particles at forward pseudorapidity.

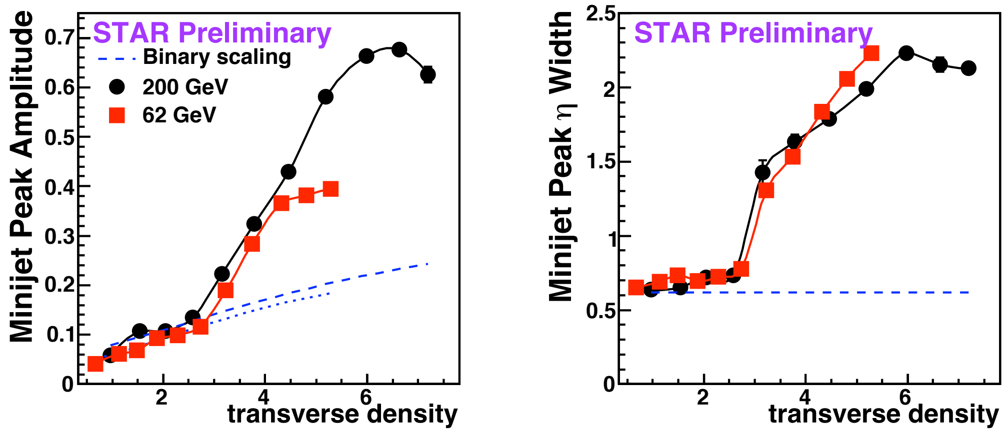

Figure 9.7: Same-side Gaussian peak amplitude and $\Delta\eta$ width as a function of centrality at two energies taken from [130]. Centrality is measured in transverse particle density, i.e. $\frac{3}{2}\frac{dN_{\mathrm{ch}}/d\eta}{\langle S\rangle}$, where $\langle S\rangle$ is the initial overlap area. Transverse density was proposed as a scaling variable for the two collision energies. The location of the abrupt transition corresponds to approximately $N_{\mathrm{part}} = 100$ at 62.4 GeV and $N_{\mathrm{part}} = 40$ at 200 GeV.

9.3.1 Autocorrelations

Inclusive correlations, or 'autocorrelations', avoid the distinction between trigger and associated particles, instead pairing all charged hadrons on equal footing. As a result, such correlations are dominated by low-momentum pairs.

PHOBOS inclusive correlation measurements have largely focused on the strength of the one-dimensional Gaussian correlation in $\Delta\eta$, parameterized generically in terms of 'cluster' size and width [129]. The analysis integrated over $\Delta\phi$ to avoid having to subtract a flow term. However, this integration prevents direct access to ridge-like correlations among inclusive particle pairs. Nonetheless, the intriguing splitting between near-side and away-side cluster size as a function of centrality may be an indirect manifestation of such a 'soft ridge'.

The analysis of autocorrelations in STAR attempts to decompose the correlation structure into a minimum set of unique features [130]. In the p+p system, p_{T} correlations suggest a natural separation of hard and soft processes. The soft part is fit with a one-dimensional Gaussian in $\Delta\eta$ (as in the PHOBOS analysis) attributed to string fragmentation and an exponential near $\Delta\phi = \Delta\eta = 0$ to account for the Hanbury-Brown and Twiss Effect (HBT) and e^+e^- conversions. The hard part is fit with a two-dimensional Gaussian centered at $\Delta\phi = \Delta\eta = 0$ ascribed to 'minijets' and a $-\cos(\Delta\phi)$ term characterizing the conservation of momentum on the opposite-side. In the Au+Au analysis one additional term is added, proportional to $\cos(2\Delta\phi)$ to account for elliptic flow.

Extracting the 'minijet' contribution from the Au+Au fit gives an interesting behavior as a function of centrality. For peripheral Au+Au events, the 'minijet' term is symmetric in $\Delta\phi$ and $\Delta\eta$ as for p+p collisions. However, increasing the centrality of the Au+Au events results in a rapid change around mid-peripheral collisions. As can be seen in Fig. 9.7 [130], there is a rapid increase in the $\Delta\eta$ width as well as the total yield of the 'minijets'. This feature has been referred to as the so-called 'soft ridge' — an extended near-side correlation, first seen in 130 GeV Au+Au autocorrelations (see Fig. 9.6 [128]).

9.3.2 Jet-Ridge Decomposition

Extensive systematic studies of high-p_{T} triggered correlations have been done by the STAR experiment. Assuming that the near-side correlation can be decomposed into jet and ridge components corresponding to distinct underlying phenomena, the following observations were made [64]:

- The ridge yield is largely independent of the trigger p_{T} up to $p_{\mathrm{T}}^{trig} \sim 9$ GeV/c^2.
- The jet yield is independent of centrality and in agreement with the yield in p+p collisions. In contrast, the ridge yield increases for more central Au+Au collisions, consistent with the PHOBOS results shown in Fig. 9.5.
- The associated p_{T} spectrum of ridge particles is similar to the inclusive spectrum and does not depend on p_{T}^{trig}. On the other hand, the jet spectrum is significantly harder with a p_{T}^{trig} dependence that is consistent with jet fragmentation.
- After subtracting the ridge component, the jet fragmentation function ($z_T = p_{\mathrm{T}}^{assoc}/p_{\mathrm{T}}^{trig}$) is independent of p_{T}^{trig} and similar to d+Au measurements.

These observations support the ansatz that the near-side correlation consists of a jet component similar to p+p or d+Au events and a ridge component with similar properties as the medium. Additionally the ridge component is found to be nearly independent of the flavor [131] and the meson/hyperon classification [132] of the trigger particle.

Finally, preliminary measurements show the jet yield to be essentially independent of the angle between the trigger and the reaction plane, whereas the ridge yield appears to be larger for in-plane triggers ($\phi^{trig} - \Psi_R \approx 0$) than out-of-plane triggers ($\phi^{trig} - \Psi_R \approx \pi/2$) [133]. The proposed interpretation of this result is that the medium is more opaque to out-of-plane jets, such that surviving in-plane jets may have deposited more energy into correlated ridge particles.

[2]This observation has been touted as evidence that the ridge is associated with hard partonic scattering and jet production, as opposed to recombination, for example. In light of the proposed theoretical mechanisms in Sect. 9.4.2, this observation might instead suggest that the surface bias induced by jet quenching has little dependence on trigger p_{T}.

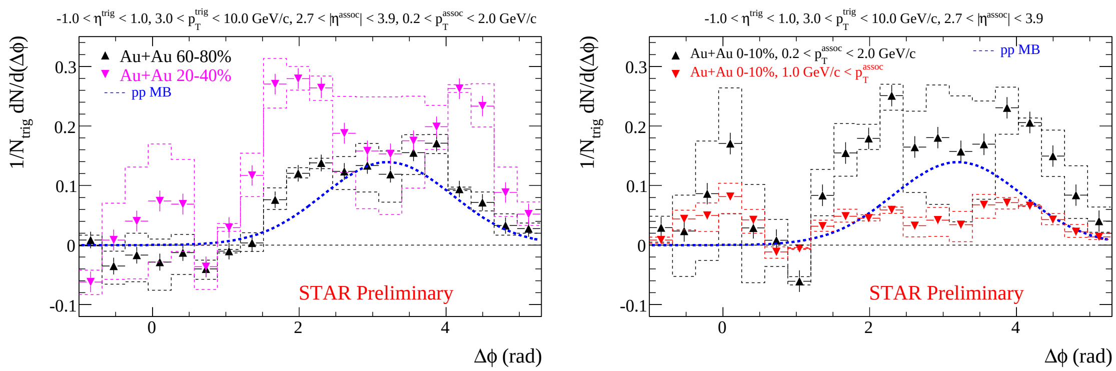

Figure 9.8: Preliminary STAR correlation functions between $p_{\mathrm{T}} > 3$ GeV/c triggers at mid-rapidity and forward associated particles, taken from [134]. (a) Correlation functions in 60-80% and 20-40% central Au+Au collisions at $\sqrt{s_{\mathrm{NN}}} =$ 200 GeV. (b) Correlation functions for two associated p_{T} ranges in 0-10% central Au+Au collisions.

9.3.3 Forward STAR Measurements

The STAR experiment can measure correlations between associated particles at forward pseudorapidity detected in the Forward Time Projection Chamber (FTPC) [135] and trigger particles at mid-rapidity detected in the Time Projection Chamber (TPC) [136]. The preliminary results of this measurement, presented at the 2006 Quark Matter Conference [134], showed a possible ridge correlation at forward rapidities in central events that was absent in more peripheral events. Although the systematic uncertainties made it impossible to rule out zero long-range correlations (see Fig. 9.8(a) [134]), the significance of the result was improved by using only associated particles with $p_{\mathrm{T}} > 1$ GeV/c. As shown in Fig. 9.8(b) [134], there is a non-zero long-range correlation for the higher associated p_{T} cut.

Despite the larger systematic uncertainties from which it suffers, this measurement still provides important evidence that the long-range ridge correlation does not arise exclusively from very low-p_{T} particles.

9.4 Theoretical Interpretation

In recent years, many different theoretical mechanisms have been proposed that qualitatively describe an extended near-side ridge correlation. In the broadest sense, these can be considered to belong to three very different families:

1. Jet fragmentation modified by the medium.

2. Longitudinally separated particles with sources correlated in the transverse plane, coupled to strong radial flow.

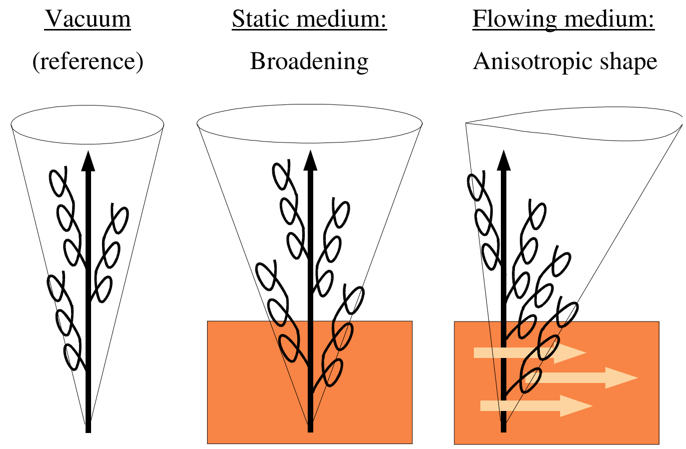

Figure 9.9: Diagram of vacuum fragmentation, the broadening in the presence of a dense medium, and the anisotropy introduced by a flowing medium, taken from [137].

3. Particles in the medium that have been excited by their proximity to the trajectory of the jet trigger.

9.4.1 Medium Modification of Fragmentation

It has been proposed that the modified near-side correlation structure in Au+Au collisions is due to the effect of the medium on jet fragmentation. Among the theories in this family, the mechanism responsible for the asymmetrical broadening of radiated gluons varies substantially, including coupling to longitudinal flow [137], turbulent color fields [138], anisotropic plasma [139], and glasma [140]. Nonetheless, all the theories within this family attribute the correlated particle production to jet fragments.

Longitudinal Collective Flow

In a dense medium, Brownian motion of jet fragments induces a broadening of the jet structure (see Fig. 9.9 [137]). However, the medium-induced gluon radiation depends not just on the energy density of the medium, but also on its collective flow [137]. The presence of longitudinal flow can break the rotational symmetry of the jet energy distributions in $\Delta\eta$ x $\Delta\phi$.

This scenario was able to reproduce the centrality dependence of the $\Delta\eta$ and $\Delta\phi$ widths of triggered correlations measured in STAR [141]. It has not been explained, however, how this mechanism would produce the relatively flat structure of the near-side ridge correlation, not to mention its extent over four units of rapidity.

Anisotropic Plasmas, Turbulent Color Fields, and Glasma

It is suggested by Romatschke [139] that rapid expansion can result in a large anisotropy in the momentum distribution of partons making up the medium. Propagating a heavy quark through this expanding medium results in a greater broadening in the longitudinal direction due to elastic collisions. It is proposed that this mechanism could be responsible for the ridge.

A number of issues with this explanation are noted in [138]. First, elastic scatterings are likely not the main source of energy loss for the light partons that are responsible for the ridge. Also, the large values of momentum anisotropy ($\xi \sim 10$) that are required to generate a ridge at $\Delta\eta = 2$ are not consistent with the low shear viscosity ($\eta/s \leq 0.3$) implied by the data[3].

Majumder *et al* [138] provide yet another possible mechanism involving plasma instabilities. Turbulent color fields, which have already been considered as a candidate for the fast equilibration times of the medium, are shown to induce a broadening in the induced gluon radiation pattern. The instability pattern results in a dominance of the transversely polarized color magnetic field mode, accounting for the preferential deflection along the beam direction.

Finally, Mizukawa *et al* have investigated the possibility of momentum broadening in a pre-thermalized glasma[4] state [140]. The authors show that an anisotropic broadening from this early state, corresponds to a ridge structure in the final-state hadrons after simulating energy loss in a QGP and hadronization.

Causality

An important consideration in the discussion of long-range correlations is the concept of causality. Figure 9.10 shows a space-time diagram of the system evolution after a collision of two relativistic nuclei. At the freezeout surface, interactions between particles cease – they stream freely into the detectors. Therefore, any event that has a causal influence on a particle must lie within the light cone pointing back in time from freezeout (see the shaded regions in Fig. 9.10). Correlations between pairs of particles can only come from a space-time region defined by the overlap between their respective light cones. Assuming boost invariance, the condition for the latest time a correlation can be generated is [143]:

$$\tau \leq \tau_{freezeout} e^{-\frac{1}{2}|y_A - y_B|} \tag{9.1}$$

where y_A and y_B are the rapidities of the two correlated particles. For a rapidity gap of four units, the causal event must occur almost an order of magnitude before freezeout.

[3] The momentum anisotropy parameter ξ of the expanding medium is related to shear viscosity η by the relation $\xi \approx 10\eta/(s\tau T)$, where s is entropy, τ is proper time after the initial hard collision, and T is temperature [138].

[4] Glasma is the highly coherent matter making the transition from a Color Glass Condensate (CGC) initial state to an equilibrated QGP. It is characterized by the decay of longitudinal color electric and magnetic fields [142].

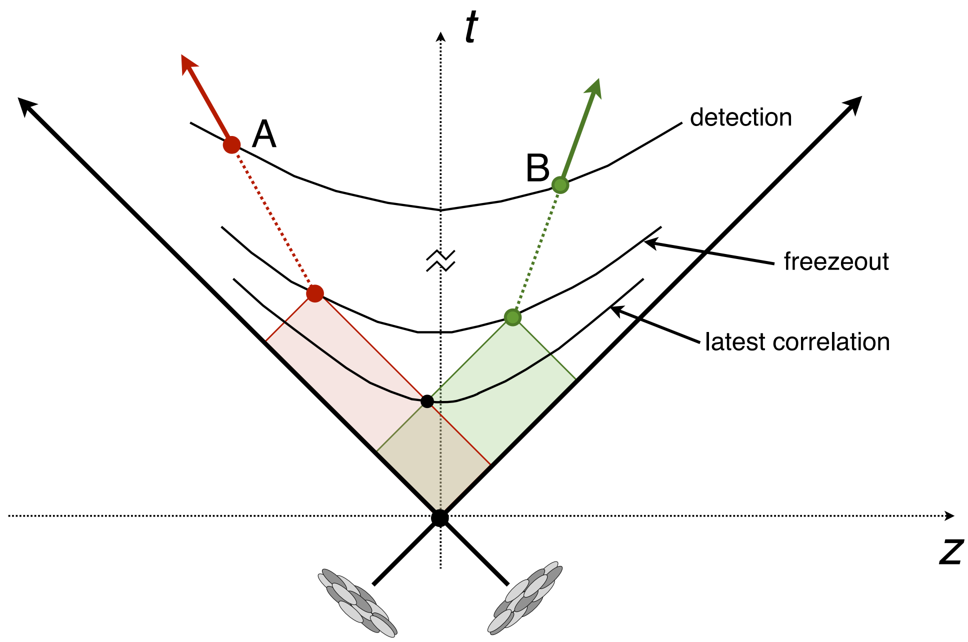

Figure 9.10: A space-time diagram of a heavy ion collision [143]. The two nuclei approach at speeds near the speed of light and collide at the origin. Curved lines represent surfaces of constant proper time, τ. The shaded areas are the regions of causal influence on particles A and B before freezeout. Correlations can only be generated in the overlap region.

For long-range correlations this is a powerful constraint, but it should be noted that the condition $\eta \approx y$ is violated for very low-p_T particles. For instance, a pion with $p_\mathrm{T} = 20$ MeV/c at $\eta = 3$ corresponds to a rapidity of only 1.16. Because the single-layer multiplicity detectors in PHOBOS cannot select on the momentum of associated particles, it has been asked whether the large $\Delta\eta$ correlations might be dominated by very low-p_T particles. However, BRAHMS measurements show that the particle spectra at y=0 and y=3 are quite similar (the inverse slope parameters vary by no more than 20%) [144]. As a consequence, there are very few particles with such low transverse momentum. Additionally, the forward STAR data with an associated trigger of $p_\mathrm{T} > 1$ GeV/c show if anything an increased long-range correlation compared to the lower-p_T^{assoc} sample [134].

The above caveat notwithstanding, the persistence of the ridge correlation out to $\Delta\eta = 4$ seems impossible to reconcile with the coupling of gluon radiation to longitudinal flow depicted in Fig. 9.9. It is less clear how the other modified fragmentation proposals listed in Sect. 9.4.1 are affected by causality considerations, as they rely on various pre-equilibrium mechanisms. Nonetheless, without more quantitative theoretical work, it remains difficult to see how any models of this type could reproduce the relative flatness of the near-side correlation structure.

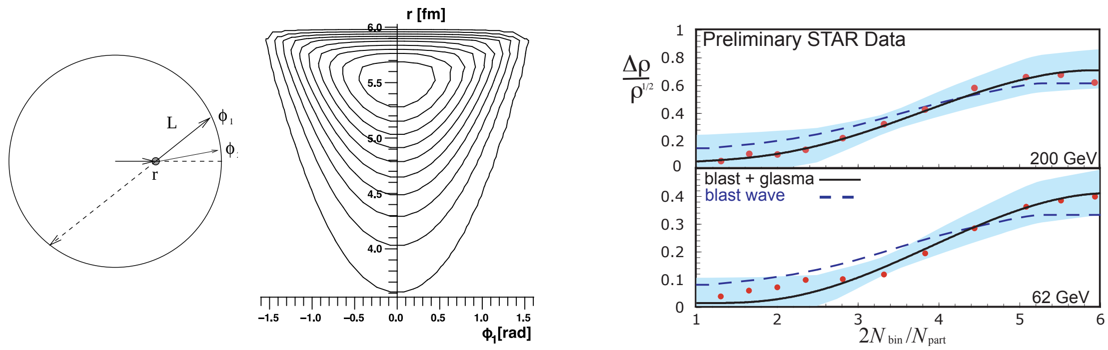

(a) Transverse Plane (b) Surviving Jets (c) Blast-wave + Glasma Model

Figure 9.11: (a) The location of a hard scattering in the transverse plane of a central heavy ion collision. The survival probability depends on the path length (L), which is a function of radius (r) and jet direction (ϕ_1). (b) Distribution of surviving jets in the r-ϕ_1 plane [146]. The majority of surviving jets emerge almost radially outwards ($\phi_1 = 0$) from points near the surface ($r \gtrsim 5$ fm). (c) Minijet correlation amplitudes extracted from STAR autocorrelations [130] as a function of centrality at $\sqrt{s_{\mathrm{NN}}} = 62.4$ and 200 GeV. The data are compared to a blast-wave model with and without the effect of glasma flux tubes [147].

9.4.2 Coupling to Radial Flow

In the second theoretical family, the long-range correlations do not come from particle pairs within the same jet. Instead, longitudinally separated particles have sources correlated in the transverse plane. Two different scenarios for such a correlation – QCD bremsstrahlung along the beam [145, 146] and glasma flux tubes [143, 147] – will be described in detail in the following sections. In both cases, the narrowness in $\Delta\phi$ of the near-side structure is a consequence of the coupling to strong radial flow.

QCD Bremsstrahlung

It has been suggested in [146] that the ridge structure is essentially an artifact of the correlation between the transverse location of a hard collision and the angular distribution of the surviving jet. Because of jet quenching, high-p_T trigger particles originate primarily from the edge of the nucleus (see Fig. 9.11(b) [146]). As shown in Fig. 9.11(a) [146], the survival probability of a trigger parton is maximized by taking the shortest path through the medium – radially outwards – coinciding with the direction of collective flow.

Hard collisions produce not just the two familiar jets, but also gluon radiation along the beam direction. In heavy ion collisions, particles associated with this QCD bremsstrahlung can be boosted transversely by the radial expansion of the system.

Since the location of the hard scattering is localized in the transverse plane, this radial boost correlates the remnants of the forward gluon radiation to the angular direction of the triggered jet at mid-rapidity.

Because the QCD bremsstrahlung has a similarly wide rapidity distribution as the bulk, a ridge structure that is quite broad in $\Delta\eta$ is naturally reproduced. It will be interesting to see if this model can reproduce the abundance of data on the correlation strength versus centrality and system size, using realistic values of radial flow and source geometry dependent jet quenching.

Glasma Flux Tubes

The existence of long-range rapidity correlations is not unique to heavy ion collisions. They have been observed in p+p collisions at the CERN ISR [148], by the UA5 experiment at SPS [149], and most recently by the PHOBOS experiment at RHIC [150]. Such long-range correlations are intrinsic features of string breaking models.

Unlike in p+p collisions, coupling to radial flow in heavy ion collisions can induce azimuthal correlations. In string breaking models, particles are produced independently along the length of the flux tubes. However, their common transverse position corresponds to a common transverse expansion, collimating the long-range correlation into a ridge that is narrow in $\Delta\phi$. In Fig. 9.11(c) [147], the result of combining string breaking and radial flow is shown to agree qualitatively with the centrality dependence of the autocorrelation strength measured by STAR [130].

The essential new feature of *glasma* flux tubes, put forth in [143], is their localization in a transverse region of size $1/Q_s$, where Q_s is the saturation scale. An improved agreement is found between this model [147] and the centrality and collision energy dependence of STAR autocorrelations [130], again using a blast-wave parameterization of radial flow. While this model has not yet been applied to triggered correlations, the longitudinal flux tubes should still produce a broad correlation in $\Delta\eta$. In fact, an explanation of the ridge involving radial flow is supported by the slightly harder spectrum of ridge particles observed in triggered correlations compared to the bulk [64]. Because most of the surviving triggers originate near the surface, correlated particles would pick up a greater than average radial boost.

9.4.3 Medium Excited by Jet Energy Loss

For the third family of theories, the ridge correlation is a consequence of medium partons that have been excited by their proximity to the trajectory of the jet trigger. The clear advantage to such an explanation is that it effortlessly explains the preponderance of evidence showing the ridge properties to be similar to the bulk (see Sect. 9.3.2). In the recombination model [151, 152], the medium is excited by the localized heating of thermal partons, while in the momentum kick model [153–155], scatterings by the trigger impart a momentum kick on medium partons in the trigger direction. One further proposal, which will not be discussed in detail due to the lack of quantitative predictions, is hydrodynamic ‘backsplash’ from the away-side jet [156]. Analogous to a raindrop

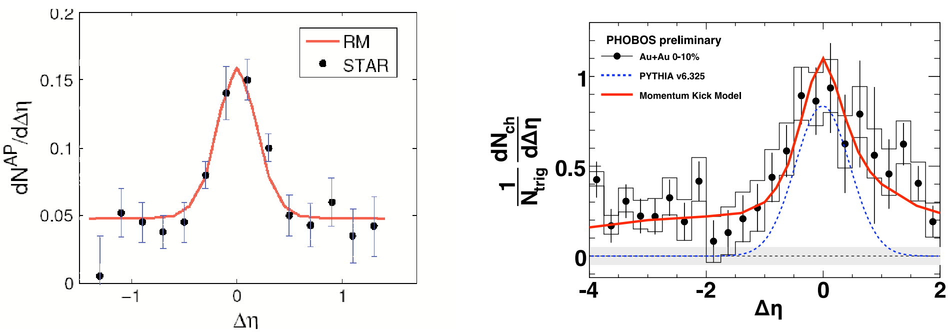

(a) Recombination Model

(b) Momentum Kick Model

Figure 9.12: (a) STAR triggered correlation in $\Delta\eta$ compared to recombination model with a thermal enhancement of $\Delta T \approx 15$ MeV taken from [152]. (b) Comparison of momentum kick model prediction [155] to the PHOBOS per-trigger correlated yield as a function of $\Delta\eta$ for 0-10% central Au+Au.

falling into a puddle, the penetration of the away-side jet into the medium results in a splash of oppositely directed particles (i.e. towards the near-side). This mechanism has the desirable feature that the ridge structure has the same $\Delta\eta$ extent as the away-side correlation. However, without further theoretical work it is unclear how seriously this picture should be taken.

Recombination of Energetic Thermal Partons

The development of recombination models was motivated by observations at intermediate p_T (e.g. baryon-to-meson ratios, differing p_T dependence of elliptic flow between baryons and mesons) that could be explained by the recombination of valence quarks at hadronization. Within the recombination framework, triggered correlations are described as follows: a hard parton is scattered near the surface losing energy along its trajectory through the medium. Upon exiting the medium, the parton fragments into shower particles (S) that recombine with enhanced thermal particles (T) to become both the trigger particle and the jet-like associated particles on near-side. Pairs of enhanced thermal particles (TT for mesons, TTT for baryons) recombine to form the associated particles of the ridge, which are noticeable after background subtraction due to their increased temperature. An enhancement of $\Delta T \approx 15$ MeV is found to reproduce the STAR data on the interval $|\Delta\eta| < 1.2$ (see Fig. 9.12(a) [152]).

Due to causality, correlations between particles separated by many units of rapidity must be imprinted in the very earliest moments of the collisions. It seems improbable that the energy deposited by the trigger jet can thermalize quickly enough to allow correlations at $\Delta\eta = 4$. Thus, the PHOBOS triggered correlations measurement appears to rule out this explanation of the ridge phenomenon.

Momentum Kick Model

The momentum kick model attempts to describe, as simply as possible, the essential elements of the experimentally observed correlation features: particles in the ridge share the properties of the bulk and receive their azimuthal properties from the trigger. In the model, jets are produced near the surface of the medium, suffering at most one collision before escaping. The jet-medium collision gives a momentum kick to the medium parton in the direction of the jet.

It is claimed that the jet-medium collisions sample the properties of the medium (i.e. rapidity width, p_T distribution, etc.) at the very earliest moments after the collision of the two nuclei. The magnitude of the average momentum kick and the rapidity width of the medium partons are extracted by fitting to STAR results at mid-rapidity [64] and forward rapidity [134]. Using these parameters, the model *predicted* the correlation in the PHOBOS acceptance quite accurately as shown in Fig. 9.12(b). It should be pointed out that the forward STAR results have quite a similar acceptance to the forward PHOBOS results, except for a slightly higher trigger p_T. (Recall that the ridge yield closer to mid-rapidity hardly depends on trigger p_T at all [64].) Therefore, it isn't obvious that this is so much a prediction as a verification that the STAR and PHOBOS results are consistent.

One particularly interesting feature of the momentum kick model is that it is quite sensitive to the properties of the early system. For example, it requires a very wide rapidity distribution for the initial partons – much wider than the distribution of final hadrons. If this model turns out to be a valid description of correlated particle production, it may be possible to use the structure of long-range correlations to extract the temperature and rapidity distribution at the very earliest moments after the collision.

An issue that certainly needs to be addressed is finding a plausible mechanism with associated cross-sections that can account for the magnitude and frequency of these momentum kicks. In a sense, the momentum kick model is not so different from the model proposed by Shuryak in [146]. In place of the momentum kick from a trigger parton, there is a boost from radial flow aligned with the surviving jet trigger. In place of the wide distribution of initial partons in the medium, there is a wide distribution of QCD bremsstrahlung.

9.4.4 Summary of Theoretical Models

1. The longitudinal flow picture [137] is inconsistent with the very broad extent of the ridge correlation due to causality considerations. Furthermore, it has difficulty reproducing the flatness of the observed ridge in $\Delta\eta$.

2. Other proposed mechanisms for medium modification of jet fragmentation [138–140] rely on very early pre-equilibrium processes. While the observed structure of the ridge correlation is not transparently attained, further quantitative calculations will be required to determine if these theoretical proposals are consistent with this measurement.

3. The wide rapidity distribution of QCD bremsstrahlung invoked in [146] and the

early time of the hard scattering are certainly consistent with our result. It remains to be seen whether quantitative theoretical calculations using realistic inputs can reproduce experimental results.

4. The glasma flux tube model [143, 147] has already shown an impressive agreement with the STAR autocorrelation results, though it is unclear how important the *glasma* part really is to the result. It appears likely that flux tubes will be consistent with this measurement, though the correlation has not yet been presented versus $\Delta\eta$.

5. Because of causality constraints, an explanation of the ridge based on recombination of thermal partons [151, 152], enhanced by the deposition of energy from a passing jet trigger, seems inconsistent with this measurement.

6. At present, the momentum kick model has made the only quantitative prediction of the near-side triggered correlation for the PHOBOS acceptance [155]. It remains to be seen whether the striking agreement can be understood in terms of a plausible mechanism for the 'kick'.

10 Summary

The dynamical interactions between high-p_T probes and the hot, dense medium produced in heavy ion collisions have been studied experimentally by the PHOBOS experiment. Details of the analysis of single-particle transverse momentum spectra and p_T-triggered, two-particle correlations are presented in this thesis.

Charged hadron transverse momentum distributions for Cu+Cu collisions at $\sqrt{s_{NN}} =$ 200 and 62.4 GeV have been measured and compared to the Au+Au spectra measured previously at both energies [57, 95]. It has been suggested that the large suppression of the particle yields in central Au+Au collisions, compared to binary scaling of p+p, is a consequence of energy loss via final-state scatterings in the dense, strongly interacting medium [55, 60, 61]. By varying the geometry and density of the produced system, the precise nature of the energy loss mechanism was tested.

At both energies, the nuclear modification factor, R_{AA}, was shown to depend only on the size of the produced system, measured either by N_{coll} or N_{part}. The scaling of the high-p_T suppression with system size supported the prediction of a simple geometric model, which related the survival probability of a jet to a quadratic dependence of energy loss on path length in an expanding medium. Interestingly, this observed scaling between the Au+Au and Cu+Cu yields persisted over the full p_T-range that was measured ($0.25 < p_T < 7.0$). It remains a challenge to theoretical models to explain how the numerous mechanisms of particle production can conspire to produce such similar spectra over a large range of p_T.

In addition, two-particle angular correlations with respect to high-p_T trigger particles have been measured in Au+Au collisions at $\sqrt{s_{NN}} = 200$ GeV over the broad longitudinal acceptance of the PHOBOS multiplicity array. The correlation structure in Au+Au was found to be strongly modified compared to p+p collisions. The magnitude of the near-side peak due to jet fragments was largely unchanged. In Au+Au, however, the jet correlation was accompanied by a novel 'ridge' structure of near-side, correlated partners that extended over the full measured pseudorapidity range ($-4 < \Delta\eta < 2$). As in previous measurements of the ridge near mid-rapidity [64], the magnitude of the correlation was seen to have a pronounced centrality dependence.

Many different theoretical mechanisms have been proposed that can qualitatively describe the presence of such an extended, near-side correlation near mid-rapidity. The large $\Delta\eta$ extent observed in this measurement places a powerful constraint on possible explanations of the ridge phenomenon. For a boost-invariant system, any effect that might have a causal influence on two particles separated by such a large rapidity gap is constrained to a region of space-time defined by the overlap of their backward-pointing light cones from freezeout. For a rapidity gap of $\Delta y = 4$, this requires that the correlation originated at least an order of magnitude earlier than freezeout. Based on these causality considerations, the $\Delta\eta$ extent of the ridge correlation is inconsistent with jet fragmentation in a longitudinally flowing medium. Similarly, recombination models that require thermalization of the deposited jet energy are strongly disfavored.

The PHOBOS correlation measurement seems to be consistent with a number of promising models based on a coupling of longitudinal correlations to radial flow. More theoretical work is needed, however, before these models can be compared quantitatively to the experimental results.

A Fundamental Particles

Generation	Particle	Symbol	Charge	Mass [157]
First	Up Quark	u	+2/3	1.5 – 4.5 MeV
	Down Quark	d	-1/3	5 – 8.5 MeV
Second	Strange Quark	s	-1/3	80 – 155 MeV
	Charm Quark	c	+2/3	1.0 – 1.4 GeV
Third	Bottom Quark	b	-1/3	4.0 – 4.5 GeV
	Top Quark	t	+2/3	174.3 ± 5.1 GeV

Table A.1: The properties of the six quarks. As discussed in Sect. 1.2, each quark can come in three colors (i.e. red, green blue) . In addition, each quark is accompanied by an antiquark with the opposite charge and color. The values of the quark masses are taken from the best estimates quoted in the Particle Data Book [157]

Generation	Particle	Symbol	Charge	Mass (MeV/c^2) [158]
First	Electron Neutrino	ν_e	0	$< 2 \times 10^{-6}$
	Electron	e^-	-1	0.511
Second	Muon Neutrino	ν_μ	0	< 0.19
	Muon	μ^-	-1	105.7
Third	Tau Neutrino	ν_τ	0	< 18.2
	Tau	τ^-	-1	1777

Table A.2: The properties of leptons. Again, there is an oppositely charged antiparticle for each particle listed here. The listed neutrino masses are effective masses, see [158].

	Gravitational	Electromagnetic	Weak	Strong
Field Boson	graviton	photon	$W^{\pm}$, Z	gluon
Spin-Parity	2^+	1^-	1^-, 1^+	1^-
Mass [GeV/c²]	0	0	80.2, 91.2	0
Range [m]	∞	∞	10^{-18}	$\leq 10^{-15}$
Source	mass	charge	'weak charge'	'color charge'
Coupling	$\frac{G_N M^2}{4\pi\hbar c}$	$\alpha = \frac{e^2}{4\pi\hbar c}$	$\frac{G(Mc^2)^2}{(\hbar c)^3}$	α_s
Constant	$= 5 \text{ x } 10^{-40}$	$= 1/137$	$= 1.17 \text{ x } 10^{-5}$	≤ 1
Typical Lifetime [s]		10^{-20}	10^{-10}	10^{-23}
Cross-section [m²]		10^{-33}	10^{-39}	10^{-30}

Table A.3: Some properties of the fundamental interactions taken from [159]. Note that the very small range of the weak force and its relative weakness at low energies is a consequence of the large mass of the $W^{\pm}$ and Z bosons. G_N is Newton's gravitational constant. For the calculation of coupling constnts, Mc^2 is taken to be 1 GeV – approximately the proton mass.

B Kinematic Variables

The rapidity variable, denoted by the symbol y, has the useful property that relativistic rapidities are additive (unlike velocities). It can be related to the velocity β (in units of the speed of light) by

$$\beta = \tanh y \tag{B.1}$$

Similarly, it is related to the Lorentz factor by

$$\gamma = \frac{1}{\sqrt{1-\beta^2}} = \cosh y \tag{B.2}$$

Another pair of useful identities is:

$$\begin{aligned} E &= m_T \cosh y \\ p_z &= m_T \sinh y \end{aligned} \tag{B.3}$$

where $m_T^2 = m_0^2 + p_T^2 = E^2 - p_z^2$.

From the above identities, rapidity can be expressed as in Eq. B.4. In many experimental situations, when the mass of a particle is not known, it is convenient to approximate rapidity with pseudorapidity which can be determined based only on the polar angle θ (see Eq. B.5). This approximation is very good for high energy particles.

$$\begin{aligned} y &= \frac{1}{2}\ln\left(\frac{E+p_z}{E-p_z}\right) \\ &\approx \frac{1}{2}\ln\left(\frac{p+p_z}{p-p_z}\right) \qquad \text{for } m^2 \ll E^2 \\ &= \frac{1}{2}\ln\left(\frac{p+p\cos(\theta)}{p-p\cos(\theta)}\right) \\ &= \frac{1}{2}\ln\left(\frac{1+\cos(\theta)}{\sin(\theta)}\,\frac{\sin(\theta)}{1-\cos(\theta)}\right) \\ &= \frac{1}{2}\ln\left(\frac{1}{\tan(\theta/2)}\,\frac{1}{\tan(\theta/2)}\right) \end{aligned} \tag{B.4}$$

$$y \approx -\ln(\tan(\theta/2)) \equiv \eta \tag{B.5}$$

C Centrality Tables

Bin	Fraction	EOct Cuts	N_{part}	N_{coll}
17	0% to 3%	723.0 to 99999.0	108 ± 3.1	208 ± 14.9
16	3% to 6%	644.6 to 723.0	99.9 ± 2.9	186 ± 13.4
15	6% to 10%	558.7 to 644.6	91.1 ± 2.7	163 ± 11.8
14	10% to 15%	468.8 to 558.7	79 ± 2.6	132 ± 9.9
13	15% to 20%	392.2 to 468.8	67.5 ± 2.7	106 ± 8.6
12	20% to 25%	326.9 to 392.2	56.9 ± 2.9	83.1 ± 7.7
11	25% to 30%	270.1 to 326.9	47.4 ± 3.1	64.3 ± 7.0
10	30% to 35%	222.1 to 270.1	39.7 ± 3.2	50.4 ± 6.4
9	35% to 40%	181.3 to 222.1	32.7 ± 3.3	38.6 ± 5.7
8	40% to 45%	146.4 to 181.3	26.5 ± 3.2	29.2 ± 5.0
7	45% to 50%	116.8 to 146.4	21.3 ± 2.9	21.9 ± 4.2

Table C.1: Properties of the centrality selection used in Cu+Cu collisions at $\sqrt{s_{\text{NN}}} = 200$ GeV. The EOct cuts were `TrgCuts_PR05_200CuCu_B[M,P]_DCMEOct`.

Bin	Fraction	EOct Cuts	N_{part}	N_{coll}
17	0% to 3%	478.3 to 99999.0	105 ± 3.0	181 ± 13.5
16	3% to 6%	425.6 to 478.3	96.6 ± 2.8	161 ± 12.0
15	6% to 10%	368.8 to 425.6	87.5 ± 2.7	140 ± 10.6
14	10% to 15%	308.8 to 368.8	75.7 ± 2.6	114 ± 9.0
13	15% to 20%	256.9 to 308.8	63.7 ± 2.7	89.9 ± 7.9
12	20% to 25%	214.4 to 256.9	53.6 ± 3.0	71 ± 7.2
11	25% to 30%	177.1 to 214.4	44.8 ± 3.2	55.7 ± 6.7
10	30% to 35%	146.1 to 177.1	37 ± 3.3	43 ± 6.1
9	35% to 40%	118.8 to 146.1	30.6 ± 3.3	33.5 ± 5.4

Table C.2: Properties of the centrality selection used in Cu+Cu collisions at $\sqrt{s_{\text{NN}}} = 62.4$ GeV. The EOct cuts were `TrgCuts_PR05_62CuCu_B[M,P]_DCMEOct_0pt750`.

Bin	Fraction	PdlMean Cuts	N_{part}	N_{coll}
17	0% to 3%	1889.7 to 99999.0	359 ± 10.6	1105 ± 79.2
16	3% to 6%	1722.3 to 1889.7	330 ± 10.7	984 ± 73.0
15	6% to 10%	1519.0 to 1722.3	297 ± 9.8	847 ± 63.2
14	10% to 15%	1290.3 to 1519.0	256 ± 8.2	685 ± 50.5
13	15% to 20%	1085.3 to 1290.3	215 ± 6.8	537 ± 39.5
12	20% to 25%	902.8 to 1085.3	181 ± 6.3	421 ± 32.0
11	25% to 30%	743.4 to 902.8	149 ± 6.2	321 ± 26.4
10	30% to 35%	603.0 to 743.4	123 ± 6.3	245 ± 22.6
9	35% to 40%	483.4 to 603.0	101 ± 6.3	186 ± 19.5
8	40% to 45%	377.8 to 483.4	82.1 ± 6.2	138 ± 16.7
7	45% to 50%	288.5 to 377.8	64.9 ± 5.8	99.1 ± 13.7

Table C.3: Properties of the centrality selection used in Au+Au collisions at $\sqrt{s_{\mathrm{NN}}} = 200$ GeV. The PdlMean cuts were `TrgCuts_PR04_200_BM` and `TrgCuts_PR04_200_BP`. The N_{coll} numbers are those quoted in [63]. Earlier papers [57, 95] used the values directly from HIJING (see Sect. 4.3.3).

Bin	Fraction	PdlMean Cuts	N_{part}	N_{coll}
17	0% to 3%	709.3 to 99999.0	350 ± 11.2	935 ± 68.4
16	3% to 6%	653.1 to 709.3	323 ± 10.2	838 ± 60.8
15	6% to 10%	585.8 to 653.1	290 ± 8.9	723 ± 51.9
14	10% to 15%	506.9 to 585.8	246 ± 7.5	575 ± 41.3
13	15% to 20%	433.3 to 506.9	207 ± 6.9	455 ± 33.7
12	20% to 25%	366.8 to 433.3	173 ± 6.8	354 ± 28.1
11	25% to 30%	306.1 to 366.8	142 ± 6.8	272 ± 23.9
10	30% to 35%	250.8 to 306.1	116 ± 6.8	206 ± 20.4
9	35% to 40%	201.4 to 250.8	95.8 ± 6.6	158 ± 17.6
8	40% to 45%	159.9 to 201.4	77.7 ± 6.3	118 ± 14.8
7	45% to 50%	122.1 to 159.9	62.6 ± 5.7	88 ± 12.2

Table C.4: Properties of the centrality selection used in Au+Au collisions at $\sqrt{s_{\mathrm{NN}}} = 62.4$ GeV. The PdlMean cuts were `TrgCuts_PR04_63_BM` and `TrgCuts_PR04_63_BP`. The N_{coll} numbers are those quoted in [63]. Earlier papers [57, 95] used the values directly from HIJING (see Sect. 4.3.3).

D Elliptic Flow Fit Coefficients

	VALUE	ERROR
p0	5.84295e-02	1.11148e-02
p1	1.65293e-04	1.92265e-04
p2	-1.29538e-06	1.02164e-06
p3	1.40226e-09	1.68949e-09

Table D.1: Table of coefficients from the third-order polynomial fit to published hit- and track-based $v_2(N_{part})$ results.

	VALUE	ERROR
p0	0	0
p1	9.13463e-02	2.63615e-03
p2	-2.88054e-03	5.19738e-03
p3	-6.47523e-03	3.04650e-03
p4	9.66730e-04	5.36281e-04

Table D.2: Table of coefficients from the fourth-order polynomial fit to preliminary $v_2(p_T)$ scaled by the $v_2(N_{part} = 236)/v_2(N_{part})$.

	VALUE	ERROR
p0	5.16512e-02	8.20073e-04
p2	-2.34520e-03	4.63317e-04
p4	4.49349e-05	2.63290e-05

Table D.3: Table of coefficients from the even, fourth-order polynomial fit to published $v_2(\eta)$ scaled by the $v_2(N_{part} = 200)/v_2(N_{part})$.

E List of Acronyms

Facilities:

AGS	Alternating Gradient Synchrotron (http://www.bnl.gov/bnlweb/facilities/AGS.asp)
BNL	Brookhaven National Lab (http://www.bnl.gov/)
CERN	European Organization for Nuclear Research – *Conseil Européen pour la Recherche Nucléaire* (http://public.web.cern.ch/public/)
FAIR	Facility for Antiproton and Ion Research (http://www.gsi.de/fair/index_e.html)
ISR	Intersecting Storage Rings
LHC	Large Hadron Collider (http://lhc.web.cern.ch/lhc/)
RHIC	Relativistic Heavy Ion Collider (http://www.bnl.gov/RHIC/)
SPS	Super Proton Synchrotron (http://ab-dep-op-sps.web.cern.ch/ab-dep-op-sps/)

Physics Terminology:

BDMPS	Baier Dokshitzer Mueller Peigné Schiff
CFL	Color-Flavor Locked
CGC	Color Glass Condensate
DIS	Deep-Inelastic Scattering
EMC	European Muon Collaboration
GLV	Gyulassy Lévai Vitev
HBT	Hanbury-Brown and Twiss Effect
LPM	Landau Pomeranchuk Migdal
NLO	Next-to-leading Order

NNLO	Next-to-next-to-leading Order
pQCD	perturbative QCD
PQM	Parton Quenching Model
QCD	Quantum Chromodynamics
QED	Quantum Electrodynamics
QGP	Quark Gluon Plasma

PHOBOS and RHIC Hardware:

ADC	Analog-to-Digital Converter
DAC	Digital-to-Analog Converter
DAQ	Data Acquisition
DMU	Data Multiplexing Unit
FEC	Front-End Controller
FTPC	Forward Time Projection Chamber (STAR) [135]
HPSS	High Performance Storage System (http://www.hpss-collaboration.org/hpss/index.jsp)
ONO	Oxide-Nitrous-Oxide
PCAL	Proton Calorimeter
PMMA	Poly-methyl-methacrylate
PMT	Photomultiplier Tube
RF	Radio Frequency
SpecCAL	Spectrometer Calorimeter
SpecTrig	Spectrometer Trigger
TAC	Time-to-Analog Converter
TDC	Time-to-Digital Converter
TOF	Time-of-Flight
TPC	Time Projection Chamber (STAR) [136]

T0	Time-Zero Counter
VME	VERSAmodule Eurocard
ZDC	Zero-Degree Calorimeter

Experimental Terminology:

CMN	Common-Mode Noise
DCA	Distance of Closest Approach
HIJING	Heavy Ion Jet Interaction Generator (http://www-nsdth.lbl.gov/ xnwang/hijing/)
IsCol	Is Collision
MC	Monte Carlo
MinBias	Minimum Bias
MIP	Minimum Ionizing Particle
OctProbMult	Octagon Probability Multiplicity
PdlMean	Paddle Mean
PdlTDiff	Paddle Time Difference
PID	Particle Identification
RMS	Root Mean Square
RMSSel	RMS-Selected
ZYAM	Zero Yield at Minimum
ZYA1	Zero Yield at One

Bibliography

[1] R. Machleidt and I. Slaus. The nucleon-nucleon interaction. *J. Phys.*, G27:R69–R108, 2001. [arXiv:nucl-th/0101056].

[2] I. E. Dzyaloshinskii, E. M. Lifshitz, and Lev P. Pitaevskii. General theory of van der Waals' forces. *Soviet Physics Uspekhi*, 4(2):153–176, 1961. URL `http://stacks.iop.org/0038-5670/4/153`.

[3] L.M. Brown, M. Dresden, and L. Hoddeson, editors. *Pions to Quarks: Particle Physics in the 1950s*, Cambridge, U.K.; New York, U.S.A., 1989. Cambridge University Press.

[4] M. Gell-Mann. The eightfold way: A theory of strong interaction symmetry. California Institute of Technology Synchrotron Laboratory Report CTSL-20, 1961.

[5] Y. Ne'eman. Derivations of strong interactions from a gauge invariance. *Nucl. Phys.*, 26:222–229, 1961.

[6] Murray Gell-Mann. A Schematic Model of Baryons and Mesons. *Phys. Lett.*, 8: 214–215, 1964. doi: 10.1016/S0031-9163(64)92001-3.

[7] G. Zweig. An SU(3) model for strong interaction symmetry and its breaking. 2. CERN-TH-412, 1964.

[8] V. E. Barnes et al. Observation of a hyperon with strangeness -3. *Phys. Rev. Lett.*, 12:204–206, 1964. doi: 10.1103/PhysRevLett.12.204.

[9] Public domain image, 2008. URL `http://en.wikipedia.org/wiki/Image:Noneto_mesônico_de_spin_0.svg`.

[10] Public domain image, 2005. URL `http://en.wikipedia.org/wiki/Image:Octeto_bariônico.svg`.

[11] Public domain image, 2008. URL `http://en.wikipedia.org/wiki/Image:Baryon_decuplet.svg`.

[12] Jerome I. Friedman and Henry W. Kendall. Deep inelastic electron scattering. *Ann. Rev. Nucl. Part. Sci.*, 22:203–254, 1972. doi: 10.1146/annurev.ns.22.120172.001223.

[13] J. D. Bjorken. Asymptotic Sum Rules at Infinite Momentum. *Phys. Rev.*, 179:1547–1553, 1969. doi: 10.1103/PhysRev.179.1547.

[14] O. W. Greenberg. Spin and Unitary Spin Independence in a Paraquark Model of Baryons and Mesons. *Phys. Rev. Lett.*, 13:598–602, 1964. doi: 10.1103/PhysRevLett.13.598.

[15] Particle Data Group. Plots of cross sections and related quantities, 2007. URL `http://pdg.lbl.gov/2007/hadronic-xsections/hadronicrpp_page6.pdf`. Fig. 6.

[16] C. Reed. *Studies of Nucleon-Gold Collisions at 200 GeV per Nucleon Pair Using Tagged d+Au Interactions.* PhD thesis, Massachusetts Institute of Technology, 2006.

[17] R. Brandelik et al. Evidence for Planar Events in e+ e- Annihilation at High- Energies. *Phys. Lett.*, B86:243, 1979. doi: 10.1016/0370-2693(79)90830-X.

[18] N. K. Nielsen. Asymptotic freedom as a spin effect. *Am. J. Phys.*, 49:1171, 1981. doi: 10.1119/1.12565.

[19] M. E. Peskin and D. V. Schroeder. *An Introduction to Quantum Field Theory.* Addison-Wesley Pub. Co., Reading, Massachusetts, USA, 1995. ISBN 0-201-50397-2.

[20] D. J. Gross and Frank Wilczek. Ultraviolet behavior of non-Abelian gauge theories. *Phys. Rev. Lett.*, 30:1343–1346, 1973. doi: 10.1103/PhysRevLett.30.1343.

[21] H. David Politzer. Reliable perturbative results for strong interactions? *Phys. Rev. Lett.*, 30:1346–1349, 1973. doi: 10.1103/PhysRevLett.30.1346.

[22] Siegfried Bethke. Experimental tests of asymptotic freedom. *Prog. Part. Nucl. Phys.*, 58:351–386, 2007. doi: 10.1016/j.ppnp.2006.06.001. Shown in Fig. 17. [arXiv:hep-ex/0606035].

[23] Rajan Gupta. Introduction to lattice QCD. 1997. [arXiv:hep-lat/9807028].

[24] Kenneth G. Wilson. Confinement of quarks. *Phys. Rev.*, D10:2445–2459, 1974. doi: 10.1103/PhysRevD.10.2445.

[25] S Chakrabarty. On the possibility of nuclear liquid-gas phase transition. *Journal of Physics G: Nuclear and Particle Physics*, 20(3):469–475, 1994. URL `http://stacks.iop.org/0954-3899/20/469`.

[26] Mark G. Alford, Krishna Rajagopal, and Frank Wilczek. QCD at finite baryon density: Nucleon droplets and color superconductivity. *Phys. Lett.*, B422:247–256, 1998. doi: 10.1016/S0370-2693(98)00051-3.

[27] R. Rapp, Thomas Schafer, Edward V. Shuryak, and M. Velkovsky. Diquark Bose condensates in high density matter and instantons. *Phys. Rev. Lett.*, 81:53–56, 1998. doi: 10.1103/PhysRevLett.81.53.

[28] Mark G. Alford, Krishna Rajagopal, and Frank Wilczek. Color-flavor locking and chiral symmetry breaking in high density QCD. *Nucl. Phys.*, B537:443–458, 1999. doi: 10.1016/S0550-3213(98)00668-3.

[29] Mark G. Alford, Andreas Schmitt, Krishna Rajagopal, and Thomas Schafer. Color superconductivity in dense quark matter. 2007. [arXiv:0709.4635].

[30] Dany Page and Sanjay Reddy. Dense Matter in Compact Stars: Theoretical Developments and Observational Constraints. *Ann. Rev. Nucl. Part. Sci.*, 56:327–374, 2006. doi: 10.1146/annurev.nucl.56.080805.140600. [arXiv:astro-ph/0608360].

[31] J. C. Collins and M. J. Perry. Superdense matter: Neutrons or asymptotically free quarks? *Phys. Rev. Lett.*, 34(21):1353–1356, May 1975. doi: 10.1103/PhysRevLett.34.1353.

[32] Edward Shuryak. Quantum chromodynamics and the theory of superdense matter. *Physics Reports*, 61(2):71–158, 1980.

[33] Z. Fodor and S. D. Katz. Critical point of QCD at finite T and mu, lattice results for physical quark masses. *JHEP*, 04:050, 2004. [arXiv:hep-lat/0402006].

[34] Frithjof Karsch. Lattice QCD at high temperature and density. *Lect. Notes Phys.*, 583:209–249, 2002. [arXiv:hep-lat/0106019].

[35] B. B. Back et al. The PHOBOS perspective on discoveries at RHIC. *Nucl. Phys.*, A757:28–101, 2005. doi: 10.1016/j.nuclphysa.2005.03.084. [arXiv:nucl-ex/0410022].

[36] John Adams et al. Experimental and theoretical challenges in the search for the quark gluon plasma: The STAR collaboration's critical assessment of the evidence from RHIC collisions. *Nucl. Phys.*, A757:102–183, 2005. doi: 10.1016/j.nuclphysa.2005.03.085. [arXiv:nucl-ex/0501009].

[37] K. Adcox et al. Formation of dense partonic matter in relativistic nucleus nucleus collisions at RHIC: Experimental evaluation by the PHENIX collaboration. *Nucl. Phys.*, A757:184–283, 2005. doi: 10.1016/j.nuclphysa.2005.03.086. [arXiv:nucl-ex/0410003].

[38] I. Arsene et al. Quark gluon plasma and color glass condensate at RHIC? The perspective from the BRAHMS experiment. *Nucl. Phys.*, A757:1–27, 2005. doi: 10.1016/j.nuclphysa.2005.02.130. [arXiv:nucl-ex/0410020].

[39] K. Splittorff. The sign problem in the epsilon-regime of QCD. *PoS*, LAT2006:023, 2006. [arXiv:hep-lat/0610072].

[40] Philippe de Forcrand and Owe Philipsen. The chiral critical line of N(f) = 2+1 QCD at zero and non-zero baryon density. *JHEP*, 01:077, 2007. [arXiv:hep-lat/0607017].

[41] Christof Roland. Particle ratio fluctuations in NA49. *PoS*, CFRNC2006:012, 2006.

[42] (ed.) Ma, Yu-Gang et al. Ultra-relativistic nucleus-nucleus collisions. Proceedings, 19th International Conference, Quark Matter 2006, Shanghai, P.R. China, November 14-20, 2006. Prepared for 19th International Conference on Ultra-Relativistic Nucleus-Nucleus Collisions: Quark Matter 2006 (QM2006), Shanghai, China, 14-20 Nov 2006.

[43] (ed.) Csörgő, T., (ed.) Lévai, P., (ed.) David, G., and (ed.) Papp, G. Quark matter. Proceedings, 18th International Conference on Ultra-Relativistic Nucleus-Nucleus Collisions, QM'05, Budapest, Hungary, August 4-9, 2005. Prepared for 18th International Conference on Ultrarelativistic Nucleus-Nucleus Collisions: Quark Matter 2005 (QM 2005), Budapest, Hungary, 4-9 Aug 2005.

[44] (ed.) Ritter, H. G. and (ed.) Wang, X. N. Ultra-relativistic nucleus-nucleus collisions. Proceedings, 17th International Conference, Quark Matter 2004, Oakland, USA, January 11-17, 2004. Prepared for 17th International Conference on Ultra Relativistic Nucleus-Nucleus Collisions (Quark Matter 2004), Oakland, California, 11-17 Jan 2004.

[45] J. D. Bjorken. Highly Relativistic Nucleus-Nucleus Collisions: The Central Rapidity Region. *Phys. Rev.*, D27:140–151, 1983. doi: 10.1103/PhysRevD.27.140.

[46] P. Huovinen, P. F. Kolb, Ulrich W. Heinz, P. V. Ruuskanen, and S. A. Voloshin. Radial and elliptic flow at RHIC: Further predictions. *Phys. Lett.*, B503:58–64, 2001. doi: 10.1016/S0370-2693(01)00219-2. [arXiv:hep-ph/0101136].

[47] B. B. Back et al. Identified hadron transverse momentum spectra in Au + Au collisions at s(NN)**(1/2) = 62.4-GeV. *Phys. Rev.*, C75:024910, 2007. doi: 10.1103/PhysRevC.75.024910. [arXiv:nucl-ex/0610001].

[48] B. B. Back et al. Centrality dependence of the charged particle multiplicity near mid-rapidity in Au + Au collisions at s(NN)**(1/2) = 130-GeV and 200-GeV. *Phys. Rev.*, C65:061901, 2002. doi: 10.1103/PhysRevC.65.061901. [arXiv:nucl-ex/0201005].

[49] B. Alver et al. Importance of Correlations and Fluctuations on the Initial Source Eccentricity in High-Energy Nucleus-Nucleus Collisions. *Phys. Rev.*, C77:014906, 2008. doi: 10.1103/PhysRevC.77.014906. [arXiv:0711.3724].

[50] B. B. Back et al. Centrality and pseudorapidity dependence of elliptic flow for charged hadrons in Au + Au collisions at s(NN)**(1/2) = 200-GeV. *Phys. Rev.*, C72: 051901, 2005. doi: 10.1103/PhysRevC.72.051901. [arXiv:nucl-ex/0407012].

[51] P. F. Kolb, P. Huovinen, Ulrich W. Heinz, and H. Heiselberg. Elliptic flow at SPS and RHIC: From kinetic transport to hydrodynamics. *Phys. Lett.*, B500:232–240, 2001. doi: 10.1016/S0370-2693(01)00079-X. [arXiv:hep-ph/0012137].

[52] John Adams et al. Particle dependence of azimuthal anisotropy and nuclear modification of particle production at moderate p(T) in Au + Au collisions at s(NN)**(1/2) = 200-GeV. *Phys. Rev. Lett.*, 92:052302, 2004. doi: 10.1103/PhysRevLett.92.052302. [arXiv:nucl-ex/0306007].

[53] John Adams et al. Multi-strange baryon elliptic flow in Au + Au collisions at s(NN)**(1/2) = 200-GeV. *Phys. Rev. Lett.*, 95:122301, 2005. doi: 10.1103/PhysRevLett.95.122301. [arXiv:nucl-ex/0504022].

[54] Klaus Reygers. High-p(T) direct-photon results from PHENIX. *Acta Phys. Polon.*, B37:727–732, 2006. [arXiv:hep-ex/0512015].

[55] B. B. Back et al. Centrality dependence of charged hadron transverse momentum spectra in d + Au collisions at s(NN)**(1/2) = 200-GeV. *Phys. Rev. Lett.*, 91:072302, 2003. doi: 10.1103/PhysRevLett.91.072302. [arXiv:nucl-ex/0306025].

[56] Stephen Scott Adler et al. Centrality dependence of direct photon production in s(NN)**(1/2) = 200-GeV Au + Au collisions. *Phys. Rev. Lett.*, 94:232301, 2005. doi: 10.1103/PhysRevLett.94.232301. [arXiv:nucl-ex/0503003].

[57] B. B. Back et al. Charged hadron transverse momentum distributions in Au + Au collisions at s(NN)**(1/2) = 200-GeV. *Phys. Lett.*, B578:297–303, 2004. doi: 10.1016/j.physletb.2003.10.101. [arXiv:nucl-ex/0302015].

[58] Stephen Scott Adler et al. High-p(T) charged hadron suppression in Au + Au collisions at s(NN)**(1/2) = 200-GeV. *Phys. Rev.*, C69:034910, 2004. doi: 10.1103/PhysRevC.69.034910. [arXiv:nucl-ex/0308006].

[59] John Adams et al. Transverse momentum and collision energy dependence of high p(T) hadron suppression in Au + Au collisions at ultrarelativistic energies. *Phys. Rev. Lett.*, 91:172302, 2003. doi: 10.1103/PhysRevLett.91.172302. [arXiv:nucl-ex/0305015].

[60] John Adams et al. Evidence from d + Au measurements for final-state suppression of high p(T) hadrons in Au + Au collisions at RHIC. *Phys. Rev. Lett.*, 91:072304, 2003. doi: 10.1103/PhysRevLett.91.072304. [arXiv:nucl-ex/0306024].

[61] Stephen Scott Adler et al. Absence of suppression in particle production at large transverse momentum in s(NN)**(1/2) = 200-GeV d + Au collisions. *Phys. Rev. Lett.*, 91:072303, 2003. doi: 10.1103/PhysRevLett.91.072303. [arXiv:nucl-ex/0306021].

[62] Stephen Scott Adler et al. A detailed study of high-p(T) neutral pion suppression and azimuthal anisotropy in Au + Au collisions at s(NN)**(1/2) = 200-GeV. *Phys. Rev.*, C76:034904, 2007. doi: 10.1103/PhysRevC.76.034904. [arXiv:nucl-ex/0611007].

[63] B. Alver et al. System size and centrality dependence of charged hadron transverse momentum spectra in Au + Au and Cu + Cu collisions at s**(1/2) = 62.4-GeV and 200-GeV. *Phys. Rev. Lett.*, 96:212301, 2006. doi: 10.1103/PhysRevLett.96.212301. [arXiv:nucl-ex/0512016].

[64] Jörn Putschke. Intra-jet correlations of high-p_t hadrons from STAR. *J. Phys.*, G34: S679–684, 2007. doi: 10.1088/0954-3899/34/8/S72. [arXiv:nucl-ex/0701074].

[65] C. Adler et al. Disappearance of back-to-back high p(T) hadron correlations in central Au + Au collisions at s(NN)**(1/2) = 200-GeV. *Phys. Rev. Lett.*, 90:082302, 2003. doi: 10.1103/PhysRevLett.90.082302. [arXiv:nucl-ex/0210033].

[66] A. Adare et al. Transverse momentum and centrality dependence of dihadron correlations in Au+Au collisions at sqrt(s_NN)=200 GeV: Jet-quenching and the response of partonic matter. *Phys. Rev.*, C77:011901, 2008. doi: 10.1103/PhysRevC.77.011901. [arXiv:0705.3238].

[67] John Adams et al. Distributions of charged hadrons associated with high transverse momentum particles in p p and Au + Au collisions at s(NN)**(1/2) = 200-GeV. *Phys. Rev. Lett.*, 95:152301, 2005. doi: 10.1103/PhysRevLett.95.152301. [arXiv:nucl-ex/0501016].

[68] B. B. Back et al. Charged particle multiplicity near mid-rapidity in central Au + Au collisions at s**(1/2) = 56-A/GeV and 130-A/GeV. *Phys. Rev. Lett.*, 85:3100–3104, 2000. doi: 10.1103/PhysRevLett.85.3100. [arXiv:hep-ex/0007036].

[69] M. Harrison, T. Ludlam, and S. Ozaki. RHIC project overview. *Nucl. Instrum. Meth.*, A499:235–244, 2003. doi: 10.1016/S0168-9002(02)01937-X.

[70] M. Harrison, Stephen G. Peggs, and T. Roser. The RHIC accelerator. *Ann. Rev. Nucl. Part. Sci.*, 52:425–469, 2002. doi: 10.1146/annurev.nucl.52.050102.090650.

[71] J. Wei and M. Harrison. The RHIC project: Design, status, challenges, and perspectives. **Osaka 1997, Multi-GeV high-performance accelerators and related technology**, pages 198–206, 1997. Prepared for 16th RCNP Osaka International Symposium on Multi GeV High Performance Accelerators, Osaka, Japan, 12- 14 Mar 1997.

[72] B. B. Back et al. The PHOBOS detector at RHIC. *Nucl. Instrum. Meth.*, A499:603–623, 2003. doi: 10.1016/S0168-9002(02)01959-9.

[73] W. Busza et al. To study very low p(t) phenomena at RHIC: Letter of intent. BNL-RLOI-14.

[74] K. Gulbrandsen. *Relative Yields of Antiparticles to Particles in Au+Au Collisions at 130 and 200 GeV per Nucleon Pair.* PhD thesis, Massachusetts Institute of Technology, 2004.

[75] A. Bickley. *Charged Antiparticle to Particle Ratios Near Midrapidity in d+Au and p+p Collisions at sqrt(sNN) = 200 GeV.* PhD thesis, University of Maryland, 2004. UMI-31-52308.

[76] C. Henderson. *Identified Particle Transverse Momentum Distributions from Au+Au Collisions at 62.4 GeV per Nucleon Pair.* PhD thesis, Massachusetts Institute of Technology, 2005.

[77] Clemens Adler et al. The RHIC zero degree calorimeters. *Nucl. Instrum. Meth.*, A470:488–499, 2001. doi: 10.1016/S0168-9002(01)00627-1. [arXiv:nucl-ex/0008005].

[78] R. Bindel, R. Baum, E. García, A. C. Mignerey, and L. P. Remsberg. Array of Cherenkov radiators for PHOBOS at RHIC. *Nucl. Instrum. Meth.*, A488:94–99, 2002. doi: 10.1016/S0168-9002(02)00473-4.

[79] R. Bindel, E. García, A. C. Mignerey, and L. P. Remsberg. Array of scintillator counters for PHOBOS at RHIC. *Nucl. Instrum. Meth.*, A474:38–45, 2001. doi: 10.1016/S0168-9002(01)00866-X.

[80] A. Sukhanov, P. Kulinich, and P. Sarin. A gigabit/s data acquisition system. *rtc*, 0: 123, 2005. doi: http://doi.ieeecomputersociety.org/10.1109/RTC.2005.1547512.

[81] P. Kulinich, P. Sarin, and A. Sukhanov. The DAQ system with a RACEway switch for the PHOBOS experiment at RHIC. *IEEE Trans. Nucl. Sci.*, 49:2455–2458, 2002. doi: 10.1109/TNS.2002.804729.

[82] D. A. Huffman. A method for the construction of minimum redundancy codes. *Proc. IRE*, 40:1098–1101, 1952.

[83] R. Nouicer et al. Silicon pad detectors for the PHOBOS experiment at RHIC. *Nucl. Instrum. Meth.*, A461:143–149, 2001. doi: 10.1016/S0168-9002(00)01191-8. [arXiv:nucl-ex/0208006].

[84] P. Sarin. *Measurement of Charged Particle Multiplicity Distributions in Au+Au Collisions up to 200 GeV.* PhD thesis, Massachusetts Institute of Technology, 2003.

[85] M. Plesko, J. Fitch, D. Ross, C. Gomes, P. Kulinich, H. Pernegger, P. Sarin, and B. Wadsowrth. Front-end electronics for the silicon partition of the phobos detector at rhic. *Nuclear Science Symposium Conference Record, 2001 IEEE*, 1:76–80 vol.1, Nov. 2001. ISSN 1082-3654.

[86] W. Fischer et al. Electron cloud observations and cures in the Relativistic Heavy Ion Collider. *Phys. Rev. ST Accel. Beams*, 11:041002, 2008. doi: 10.1103/PhysRevSTAB.11.041002.

[87] R. Hollis. *Centrality Evolution of Charged Particles Produced in Ultra-relativistic Au+Au and d+Au Collisions.* PhD thesis, University of Illinois at Chicago, 2005.

[88] P. Decowski. *Energy and Centrality Dependence of Mid-Rapidity Charged Particle Multiplicity in Relativistic Heavy-Ion Collisions.* PhD thesis, Massachusetts Institute of Technology, 2002.

[89] G. Roland et al. New results from the PHOBOS experiment. *Nucl. Phys.*, A774: 113–128, 2006. doi: 10.1016/j.nuclphysa.2006.06.034. [arXiv:nucl-ex/0510042].

[90] J. Hamblen. *Pseudorapidity Dependence of Directed and Elliptic Flow in Au+Au Collisions at 19.6, 62.4, 130, and 200 GeV per Nucleon Pair.* PhD thesis, University of Rochester, 2006.

[91] B. B. Back et al. Forward-backward multiplicity correlations in s(NN)**(1/2) = 200-GeV Au + Au collisions. *Phys. Rev.*, C74:011901, 2006. doi: 10.1103/PhysRevC.74.011901. [arXiv:nucl-ex/0603026].

[92] Richard O. Duda and Peter E. Hart. Use of the hough transformation to detect lines and curves in pictures. *Commun. ACM*, 15(1):11–15, 1972. ISSN 0001-0782. doi: http://doi.acm.org/10.1145/361237.361242.

[93] J. L. Kane. *Charged Hadron Transverse Momentum Spectra in Au+Au and d+Au Collisions at 200 GeV per Nucleon Pair.* PhD thesis, Massachusetts Institute of Technology, 2005.

[94] K. Adcox et al. Suppression of hadrons with large transverse momentum in central Au + Au collisions at s**(1/2)(N N) = 130-GeV. *Phys. Rev. Lett.*, 88:022301, 2002. doi: 10.1103/PhysRevLett.88.022301. [arXiv:nucl-ex/0109003].

[95] B. B. Back et al. Centrality dependence of charged hadron transverse momentum spectra in Au + Au collisions from s(NN)**(1/2) = 62.4-GeV to 200-GeV. *Phys. Rev. Lett.*, 94:082304, 2005. doi: 10.1103/PhysRevLett.94.082304. [arXiv:nucl-ex/0405003].

[96] C. Albajar et al. A Study of the General Characteristics of Proton - anti- Proton Collisions at s**(1/2) = 0.2-TeV to 0.9-TeV. *Nucl. Phys.*, B335:261, 1990. doi: 10.1016/0550-3213(90)90493-W.

[97] Torbjörn Sjöstrand et al. High-energy-physics event generation with PYTHIA 6.1. *Comput. Phys. Commun.*, 135:238–259, 2001. doi: 10.1016/S0010-4655(00)00236-8. [arXiv:hep-ph/0010017].

[98] A. Breakstone et al. Inclusive charged particle cross-sections in full phase space from proton proton interactions at ISR energies. *Z. Phys.*, C69:55–66, 1995. doi: 10.1007/s002880050005.

[99] D. Drijard et al. A MEASUREMENT OF THE INCLUSIVE CROSS-SECTION OF CHARGED PIONS AT VERY HIGH TRANSVERSE MOMENTA. *Nucl. Phys.*, B208:1, 1982. doi: 10.1016/0550-3213(82)90185-7.

[100] Peter Jacobs and Xin-Nian Wang. Matter in extremis: ultrarelativistic nuclear collisions at rhic. *Progress in Particle and Nuclear Physics*, 54: 443, 2005. URL `http://www.citebase.org/abstract?id=oai:arXiv.org:hep-ph/0405125`.

[101] Michele Arneodo. Nuclear effects in structure functions. *Phys. Rept.*, 240:301–393, 1994. doi: 10.1016/0370-1573(94)90048-5.

[102] P. Amaudruz et al. Precision measurement of the structure function ratios F2 (He) / F2 (D), F2 (C) / F2 (D) and F2 (Ca) / F2 (D). *Z. Phys.*, C51:387–394, 1991. doi: 10.1007/BF01548560.

[103] J. W. Cronin et al. Production of Hadrons with Large Transverse Momentum at 200-GeV, 300-GeV, and 400-GeV. *Phys. Rev.*, D11:3105, 1975. doi: 10.1103/PhysRevD.11.3105.

[104] Alberto Accardi. 'Naked' Cronin effect in A + A collisions from SPS to RHIC. *Eur. Phys. J.*, C43:121–125, 2005. [arXiv:nucl-th/0502033].

[105] Xin-Nian Wang. Systematic study of high p(T) hadron spectra in p p, p A and A A collisions from SPS to RHIC energies. *Phys. Rev.*, C61:064910, 2000. doi: 10.1103/PhysRevC.61.064910. [arXiv:nucl-th/9812021].

[106] Stephen Scott Adler et al. Production of Phi mesons at mid-rapidity in s**(1/2)(NN) = 200-GeV Au + Au collisions at RHIC. *Phys. Rev.*, C72:014903, 2005. doi: 10.1103/PhysRevC.72.014903. [arXiv:nucl-ex/0410012].

[107] Rudolph C. Hwa. Parton recombination at all p(T). *Eur. Phys. J.*, C43:233–237, 2005. [arXiv:nucl-th/0501054].

[108] L. D. Landau and I. Pomeranchuk. Electron cascade process at very high-energies. *Dokl. Akad. Nauk Ser. Fiz.*, 92:735–738, 1953.

[109] Arkady B. Migdal. Bremsstrahlung and pair production in condensed media at high-energies. *Phys. Rev.*, 103:1811–1820, 1956. doi: 10.1103/PhysRev.103.1811.

[110] R. Baier, D. Schiff, and B. G. Zakharov. Energy loss in perturbative QCD. *Ann. Rev. Nucl. Part. Sci.*, 50:37–69, 2000. doi: 10.1146/annurev.nucl.50.1.37. [arXiv:hep-ph/0002198].

[111] R. Baier, Yuri L. Dokshitzer, Alfred H. Mueller, S. Peigne, and D. Schiff. Radiative energy loss of high energy quarks and gluons in a finite-volume quark-gluon plasma. *Nucl. Phys.*, B483:291–320, 1997. doi: 10.1016/S0550-3213(96)00553-6. [arXiv:hep-ph/9607355].

[112] Carlos A. Salgado and Urs Achim Wiedemann. Calculating quenching weights. *Phys. Rev.*, D68:014008, 2003. doi: 10.1103/PhysRevD.68.014008. [arXiv:hep-ph/0302184].

[113] Urs Achim Wiedemann. Gluon radiation off hard quarks in a nuclear environment: Opacity expansion. *Nucl. Phys.*, B588:303–344, 2000. doi: 10.1016/S0550-3213(00)00457-0.

[114] Miklos Gyulassy, Peter Levai, and Ivan Vitev. Jet quenching in thin quark-gluon plasmas. I: Formalism. *Nucl. Phys.*, B571:197–233, 2000. doi: 10.1016/S0550-3213(99)00713-0. [arXiv:hep-ph/9907461].

[115] Thomas Henry. Full jet reconstruction in d + Au and p + p collisions at RHIC. *J. Phys.*, G30:S1287–S1290, 2004. doi: 10.1088/0954-3899/30/8/110. [arXiv:nucl-ex/0403031].

[116] A. Dainese, C. Loizides, and G. Paic. Leading-particle suppression in high energy nucleus nucleus collisions. *Eur. Phys. J.*, C38:461–474, 2005. doi: 10.1140/epjc/s2004-02077-x. [arXiv:hep-ph/0406201].

[117] Christian Klein-Boesing. Systematic study of particle production at high p(T) with the PHENIX experiment. 2006. [arXiv:nucl-ex/0606013].

[118] Axel Drees, Haidong Feng, and Jiangyong Jia. Medium induced jet absorption at RHIC. *Phys. Rev.*, C71:034909, 2005. doi: 10.1103/PhysRevC.71.034909. [arXiv:nucl-th/0310044].

[119] I. Vitev. Testing the mechanism of QGP-induced energy loss. *Acta Phys. Hung.*, A27:281–286, 2006. doi: 10.1556/APH.27.2006.2-3.23. [arXiv:hep-ph/0511237].

[120] V. S. Pantuev. Jet absorption and corona effect at RHIC. Extracting collision geometry from experimental data. *JETP Lett.*, 85:104–108, 2007. doi: 10.1134/S0021364007020026. [arXiv:hep-ph/0506095].

[121] B. Alver et al. Elliptic flow fluctuations in s(NN)**(1/2) = 200-GeV Au + Au collisions at RHIC. *J. Phys.*, G34:S907–S910, 2007. doi: 10.1088/0954-3899/34/8/S123. [arXiv:nucl-ex/0701049].

[122] C. Vale. *Elliptic Flow in Au+Au Collisions at 200 GeV per Nucleon Pair.* PhD thesis, Massachusetts Institute of Technology, 2004.

[123] H. Masui. Anisotropic flow in s(NN)**(1/2) = 200-GeV Cu + Cu and Au + Au collisions at PHENIX. *Nucl. Phys.*, A774:511–514, 2006. doi: 10.1016/j.nuclphysa.2006.06.077. [arXiv:nucl-ex/0510018].

[124] N. N. Ajitanand et al. Decomposition of harmonic and jet contributions to particle-pair correlations at ultra-relativistic energies. *Phys. Rev.*, C72:011902, 2005. doi: 10.1103/PhysRevC.72.011902. [arXiv:nucl-ex/0501025].

[125] B. Alver et al. Two-particle angular correlations in p + p and Cu + Cu collisions at PHOBOS. *J. Phys.*, G34:S1005–1010, 2007. doi: 10.1088/0954-3899/34/8/S144. [arXiv:nucl-ex/0701055].

[126] B. B. Back et al. The significance of the fragmentation region in ultrarelativistic heavy ion collisions. *Phys. Rev. Lett.*, 91:052303, 2003. doi: 10.1103/PhysRevLett.91.052303. [arXiv:nucl-ex/0210015].

[127] Edward Wenger et al. High p_T Triggered $\Delta\eta$,$\Delta\phi$ Correlations over a Broad Range in $\Delta\eta$. 2008. [arXiv:0804.3038].

[128] John Adams et al. Minijet deformation and charge-independent angular correlations on momentum subspace (eta, phi) in Au-Au collisions at s(NN)**(1/2) = 130-GeV. *Phys. Rev.*, C73:064907, 2006. doi: 10.1103/PhysRevC.73.064907. [arXiv:nucl-ex/0411003].

[129] Wei Li. System size dependence of two-particle angular correlations in p+p, Cu+Cu and Au+Au collisions. 2008. [arXiv:0804.2471].

[130] Michael Daugherity. Anomalous centrality variation of minijet angular correlations in Au-Au collisions at 62 and 200 GeV from STAR. 2008. [arXiv:0806.2121].

[131] Jana Bielcikova. Two-particle correlations with strange baryons and mesons at RHIC. 2007. [arXiv:0707.3100].

[132] Jana Bielcikova. Azimuthal and pseudo-rapidity correlations with strange particles at intermediate-p(T) at RHIC. *J. Phys.*, G34:S929–930, 2007. doi: 10.1088/0954-3899/34/8/S128. [arXiv:nucl-ex/0701047].

[133] Aoqi Feng. Away-side modification and near-side ridge relative to reaction plane at 200 gev au+au collisions, 2008. Presented at the 2008 Quark Matter Conference in Jaipur, India.

[134] Levente Molnar. Jet-like correlations between forward- and mid- rapidity in p + p, d + Au and Au + Au collisions from STAR at 200- GeV. *J. Phys.*, G34:S593–598, 2007. doi: 10.1088/0954-3899/34/8/S51. [arXiv:nucl-ex/0701061].

[135] K. H. Ackermann et al. The forward time projection chamber (FTPC) in STAR. *Nucl. Instrum. Meth.*, A499:713–719, 2003. doi: 10.1016/S0168-9002(02)01968-X.

[136] M. Anderson et al. The STAR time projection chamber: A unique tool for studying high multiplicity events at RHIC. *Nucl. Instrum. Meth.*, A499:659–678, 2003. doi: 10.1016/S0168-9002(02)01964-2.

[137] Nestor Armesto, Carlos A. Salgado, and Urs Achim Wiedemann. Measuring the collective flow with jets. *Phys. Rev. Lett.*, 93:242301, 2004. doi: 10.1103/PhysRevLett.93.242301. [arXiv:hep-ph/0405301].

[138] A. Majumder, Berndt Muller, and Steffen A. Bass. Longitudinal Broadening of Quenched Jets in Turbulent Color Fields. *Phys. Rev. Lett.*, 99:042301, 2007. doi: 10.1103/PhysRevLett.99.042301. [arXiv:hep-ph/0611135].

[139] Paul Romatschke. Momentum broadening in an anisotropic plasma. *Phys. Rev.*, C75:014901, 2007. doi: 10.1103/PhysRevC.75.014901. [arXiv:hep-ph/0607327].

[140] R. Mizukawa, T. Hirano, M. Isse, Y. Nara, and A. Ohnishi. Search for a Ridge Structure Origin with Shower Broadening and Jet Quenching. 2008. [arXiv:0805.2795].

[141] Fuqiang Wang. Measurement of jet modification at RHIC. *J. Phys.*, G30:S1299–S1304, 2004. doi: 10.1088/0954-3899/30/8/113. [arXiv:nucl-ex/0404010].

[142] T. Lappi and L. McLerran. Some features of the glasma. *Nucl. Phys.*, A772:200–212, 2006. doi: 10.1016/j.nuclphysa.2006.04.001. [arXiv:hep-ph/0602189].

[143] Adrian Dumitru, Francois Gelis, Larry McLerran, and Raju Venugopalan. Glasma flux tubes and the near side ridge phenomenon at RHIC. 2008. [arXiv:0804.3858].

[144] Djamel Ouerdane. Rapidity dependence of charged particle yields for Au + Au at s(NN)**(1/2) = 200-GeV. *Nucl. Phys.*, A715:478–481, 2003. doi: 10.1016/S0375-9474(02)01454-9. [arXiv:nucl-ex/0212001].

[145] Sergei A. Voloshin. Transverse radial expansion in nuclear collisions and two particle correlations. *Phys. Lett.*, B632:490–494, 2006. doi: 10.1016/j.physletb.2005.11.024. [arXiv:nucl-th/0312065].

[146] E. V. Shuryak. On the Origin of the 'Ridge' phenomenon induced by Jets in Heavy Ion Collisions. *Phys. Rev.*, C76:047901, 2007. doi: 10.1103/PhysRevC.76.047901. [arXiv:0706.3531].

[147] Sean Gavin, Larry McLerran, and George Moschelli. Long Range Correlations and the Soft Ridge in Relativistic Nuclear Collisions. 2008. [arXiv:0806.4718].

[148] S. Uhlig, I. Derado, R. Meinke, and H. Preissner. Observation of Charged Particle Correlations Between the Forward and Backward Hemispheres in p p Collisions at ISR Energies. *Nucl. Phys.*, B132:15, 1978. doi: 10.1016/0550-3213(78)90254-7.

[149] R. E. Ansorge et al. CHARGED PARTICLE CORRELATIONS IN ANTI-P P COLLISIONS AT C.M. ENERGIES OF 200-GEV, 546-GEV AND 900-GEV. *Z. Phys.*, C37:191–213, 1988. doi: 10.1007/BF01579906.

[150] B. Alver et al. Cluster properties from two-particle angular correlations in p + p collisions at s**(1/2) = 200-GeV and 410-GeV. *Phys. Rev.*, C75:054913, 2007. doi: 10.1103/PhysRevC.75.054913. [arXiv:0704.0966].

[151] Charles B. Chiu and Rudolph C. Hwa. Pedestal and peak structure in jet correlation. *Phys. Rev.*, C72:034903, 2005. doi: 10.1103/PhysRevC.72.034903. [arXiv:nucl-th/0505014].

[152] Rudolph C. Hwa. High p(T) hadron correlation and no correlation. *Nucl. Phys.*, A783:57–64, 2007. doi: 10.1016/j.nuclphysa.2006.11.004. [arXiv:nucl-th/0609017].

[153] Cheuk-Yin Wong. Ridge Structure associated with the Near-Side Jet in the (Delta phi)-(Delta eta) Correlation. *Phys. Rev.*, C76:054908, 2007. doi: 10.1103/PhysRevC.76.054908. [arXiv:0707.2385].

[154] Cheuk-Yin Wong. Exploring Early Parton Momentum Distribution with the Ridge from the Near-Side Jet. 2008. [arXiv:0804.4017].

[155] Cheuk-Yin Wong. The Momentum Kick Model Description of the Near-Side Ridge and Jet Quenching. 2008. [arXiv:0806.2154].

[156] V. S. Pantuev. 'Jet-Ridge' effect in heavy ion collisions as a back splash from stopped parton. 2007. [arXiv:0710.1882].

[157] K. Hagiwara et al. Review of Particle Physics. *Physical Review D*, 66:010001+, 2002. URL `http://pdg.lbl.gov`.

[158] W. M. Yao *et al.* Review of particle physics. *J. Phys.*, G33:1–1232, 2006.

[159] D. H. Perkins. *Introduction to High Energy Physics.* Addison-Wesley Pub. Co., Reading, Massachusetts, USA, 1987. ISBN 0-201-12105-0.

Acknowledgments

This work would not have been possible without the invaluable support and assistance of many people.

First and foremost, I would like to thank my advisor, Gunther Roland, who has guided me through all the challenges I have faced in my graduate studies. He has played an instrumental role in ensuring not only the success of my analyses, but the continued success of the PHOBOS experiment.

Let me express my gratitude to the other members of my thesis committee, Wit Busza and Krishna Rajagopal, for their many helpful suggestions. I would especially like to thank Wit Busza for encouraging me to take some time every week to think about the physics implications of these measurements.

It has been a pleasure working with the MIT heavy ion group. Bolek Wysłouch, Christof Roland, and Maarten Ballintijn have always been happy to lend their expertise. Gábor Veres and Constantin Loizides have been excellent role models; their own tireless work inspired everyone who had the privilege of collaborating with them. The students who came before me – Kris Gulbrandsen, Jay Kane, Conor Henderson, and Corey Reed – are responsible for teaching me most of what I know about heavy ion physics. I have truly enjoyed the relaxed, entertaining, multi-cultural environment that my fellow students – Burak Alver, Wei Li, and Siarhei Vaurynovich – bring to the office.

One nice thing about working on a small collaboration like PHOBOS is that each of my colleagues has contributed in some way to this thesis. Nonetheless, I am compelled to single out a few. I owe many thanks to Peter Steinberg, George Stephans, and Don Barton for the time and effort spent reviewing my analyses. Their attention to detail has vastly improved the quality of these results. Gerrit van Nieuwenhuizen and Rachid Nouicer built a beautiful set of silicon detectors and introduced me to the joys of making a dead channel map. Without the stellar work of Andrei Sukhanov on data acquisition and Marguerite Tonjes on data production, there would be no data to analyze! Andrzej Olszewski and Krzysztof Woźniak generated the Monte Carlo events and detector simulations that were crucial to understanding our detector response. Besides providing the centrality cuts and elliptic flow measurements that were essential to my analyses, Dave Hofman, Richard Hollis, Aneta Iordanova, Vasu Chetluru, Josh Hamblen, and Richard Bindel always ensured that meetings and conferences were a fun time.

I would like to thank Tim, Matt, Pete, Kekane, Bub, and Bradford for being great friends and making Boston such an enjoyable place to have lived over the past five years.

Finally, I owe everything to my family. Without their support and understanding (not to mention babysitting services), none of this would have been possible.